DOI: 10.1002/aenm.201702582

Review

Beyond Insertion for Na-ion Batteries: Nanostructured Alloying and Conversion Anode Materials

Huang Zhang, Ivana Hasa, and Stefano Passerini**

H. Zhang, Prof. S. Passerini

Helmholtz Institute Ulm (HIU)

Helmholtzstraße 11, Ulm 89081, Germany

E-mail: stefano.passerini@kit.edu

H. Zhang, Prof. S. Passerini

Karlsruhe Institute of Technology (KIT)

PO Box 3640, Karlsruhe 76021, Germany

Dr. I. Hasa
Energy Storage and Distributed Resources Division

Lawrence Berkeley National Laboratory

1 Cyclotron Road, Berkeley, CA 94720, USA

E-mail: ivana.hasa@lbl.gov

Keywords: alloying, anodes, conversion, nanostructure design, sodium-ion batteries,

Abstract: Sodium-ion technology has the potential to become the next generation of low cost and environmentally friendly electrochemical energy storage system for grid-level applications. The low cost and abundant raw materials employed in sodium cells have driven the recent increasing interest in sodium-ion batteries (SIBs), which appear especially appealing, since manufacturers can use the already existing production technology of lithium-ion batteries (LIBs). However, SIBs are still an early stage technology, which requires that several issues affecting cell performance be addressed. Despite the accelerated development of cathode materials, anode materials still require further investigation and optimization to reach high energy density performance. In the pursuit of high capacity anode materials, several alloying, conversion and combined conversion-alloying based electrodes have been investigated. This review offers a comprehensive overview on the recent progresses toward the realization of "beyond-insertion" anode materials. The role of nanostructuration with the associated advantages and disadvantages is presented for each class of compounds, combined with the main strategies adopted to improve the electrochemical behavior. Finally, an overview of the challenges and perspectives associated to the development of the next generation anode materials is presented with a particular focus on the role of the electrolyte solutions and solid/electrolyte interphase.

1. Introduction

One of the greatest challenges in 21st century is the rapidly increasing energy demand associated with the industrial development and population growth. Global concerns over climate changes and constraints of fossil fuels as primary power supply sources result in the exploration of green and sustainable resources, which have realized the utilization of renewable energy alternatives such as solar, wind, geothermal and tidal power. [1] The operational mode of these technologies requires the integration of efficient energy storage systems. Rechargeable batteries with cost-effective and environmentally friendly features represent the most promising strategy to efficiently store energy. [2] Secondary batteries are composed of two electrodes with different chemical potentials connected by an ionically conductive electrolyte. The amount of electrical energy per mass or volume that a battery can deliver is a function of the cell voltage and capacity, which strongly dependent on the chemistry of the electrode materials. [3]

Lithium-ion batteries (LIBs) are one of the greatest successes for energy storage applications of the last century. LIBs are light, compact and offer outstanding energy and power density dominating the market for portable electronics, hybrid and electric vehicles (EV). [4, 5] In view of the increasingly growing electrified automotive field, an increasing demand of lithium and cobalt has been observed with consequent price increase and related concerns about the future and long-term materials availability. Indeed, the global lithium supply is concentrated in a few areas with the major lithium resources located in South America brine deposits and in the Greenbushes mine in Australia.

Moreover, the market managing lithium sources is dominated by few companies such as Albemarle (ALB US), owing Rockwood Lithium, SQM (SQM US), FMC (FMC US) and Chengdu Tianqi (China), altogether controlling around 50% of the lithium supply. [6, 7] In this scenario, studies to reveal and estimate the future lithium demand are necessary and of crucial importance. In 2007 it has been calculated that if the 60 million car produced annually over the world would be totally replaced by plug-in hybrids vehicles, each of them requiring about 1.4 kg of lithium carbonate, the total annual demand for lithium would be around 420 K tons, which is about 5 times the current lithium carbonate production. This would place an unsustainable demand on lithium resources because of geochemical constraints in extracting the product from known deposits. [7, 8] At Argonne National Laboratory, Gaines and Nelson, assuming a penetration of electric vehicles in the automobile market of about 50% within 2030 and a very optimistic 90% in 2015, calculated that the annual demand of lithium in the United States will increase up to 22,000 t (117,000 tons of lithium carbonate) by 2030 and 54,000 t (287,000 tons of lithium carbonate) by 2050. [9] Considering the associated possible future risk of lithium dependency after years of dependency from oil and fossil fuels, the search of alternative chemistries to lithium for use in rechargeable batteries is not anymore necessary but mandatory.

Sodium represents the most appealing alternative to lithium. Firstly studied during the 80s alongside with LIBs, [10, 11] it was sidelined due to the more promising features of LIBs mostly in terms of energy density. The recent renewed interest in sodium-ion batteries (SIBs) has been mainly driven by the abundance and low cost of foreseen raw materials (e.g., sodium is the 4th most abundant element in the Earth's crust) and their uniform distribution, leading to lower economic and geopolitical impact. [12-14] In addition, the Na-ion chemistry is based on the rocking chair principle as LIBs, thus, it could

benefit from the great advances done in the LIBs field in the last 30 years, resulting in the accelerated knowledge-development and easy transition to manufacturing. Moreover, the use of sodium-based electrolyte solution and the implementation of aluminum as current collector at the anode side (instead of the more expensive copper) represent further cost cuts versus LIBs. [15] It should be mentioned, however, that the larger ionic radii and atomic mass of sodium result in SIBs intrinsically offering lower volumetric and gravimetric energies. [16] However, the English company Faradion has already demonstrated that optimization and proper design of the cell components may lead, in full sodium-ion configuration, to the achievement of energy density values comparable to the current lithium-ion technology. [17]

To improve the energy density of SIBs, a rational design of the electrode material is crucial, enabling the achievement of high specific capacities and appropriate redox potentials. So far, great efforts have been done in materials development reaching successful results mostly at the cathode side, mainly related to the use of layered transition metal oxides and polyanionic compounds. [18-22] The anode of choice so far reported for SIBs is hard carbon, exhibiting average specific capacities between 300-400 mAh g^{-1}. [23-26] Further breakthroughs on the energy density of SIBs strongly rely on the development of high performance anode materials. Therefore, search for anode materials with low operating potential, high reversible capacity, and structural stability, represent the next challenge for SIBs. In this context, materials with new atomic composition or unique microstructure could offer significantly enhanced properties to enable an efficient and durable energy storage ability of SIBs. Carbon-based anodes and insertion-type electrodes offer satisfactory performance, however, they are intrinsically characterized by low energy density. Promising candidates offering high electrochemical performance in terms of delivered capacity belong to the class of materials

employing a beyond-insertion storage mechanism, such as alloying, conversion and their combination (conversion-alloying). Over the years, nanotechnology has led to great advances in the nanostructuration for this class of compounds, offering a real strategy to design and architecture advanced anode materials with enhanced properties.

In this Review, we firstly clarify important parameters characterizing the anode performance in sodium cells. Additionally, we briefly summarize the advantages and disadvantages of nanostructuration for electrode materials used in rechargeable batteries to finally get to the state-of-the-art of beyond-insertion type anodes for SIBs. Alloying, conversion and the combined conversion-alloying mechanism (CAM) are considered for nanostructured anode materials. In addition, heterostructured materials are also discussed as a novel opportunity to design electrodes leading to superior electrochemical performance. Synthesis, properties and performances related to the nanostructuration are discussed to highlight the advantages and remaining challenges with respect to their governing chemistries and implementation of nanotechnology. Finally, a summary and outlook of recent achievements in the field of nanostructured anodes for SIBs are given.

2. Anode Parameters and Electrochemistry

The energy density and power density of a battery are two essential parameters for the evaluation of its practical performance. Both of them strongly depend on the cell characteristics such as the operating voltage and the delivered specific capacity. While supercapacitors dominate the field for high power application, secondary batteries such as LIBs and SIBs are expected to govern the high-energy density applications. The energy density of a cell is generally limited by its operating voltage and storage ability in terms of specific capacity. In this section, a brief overview of the most

important parameters characterizing anode systems is given together with the criteria for the selection of the next generation anode materials.

2.1. Working Potential

The cell voltage is strongly dependent by the affinity of Na^+ ions for the two electrodes and the electrochemical stability window of the electrolyte. Both electrodes should be selected taking into account that negative electrodes having a Fermi level higher than the lowest unoccupied molecular orbital (LUMO) of the electrolyte will represents the driving force for electrolyte reduction, while positive electrodes with a Fermi level lower in energy than the highest occupied molecular orbital (HOMO) will lead to electrolyte oxidation. [5, 27-29]. Typically, (see **Figure 1**) the Fermi level of the Na metal anode lies above the LUMO of the electrolyte leading to reduction of the electrolyte. This phenomenon leads to the formation of the electronically insulating, but ionically conductive, solid/electrolyte interphase (SEI) allowing the battery operation. [30] Therefore, ideal anode material candidates should exhibit electrochemical activity at low voltage (but not too close to the sodium plating potential) thus maximizing the cell voltage (i.e., the voltage difference between the cathode and the anode), conferring high energy density. Hard carbons generally exhibit redox activity at very low voltage values, thus largely contributing to an increase of the overall cell voltage in full-cell configuration but resulting in pronounced electrolyte reductive decomposition and consequent instability of the SEI in addition to the safety issues related to metal plating and dendrite growth. [31] These issues may be mitigated employing Ti-based compounds operating through insertion mechanism, which generally present a higher operating voltage and a higher safety content due to metal plating inhibition, however with a decreased energy density. A good compromise is represented by beyond-insertion anode materials. **Figure 2 a-c** shows the typical voltage profile

associated to alloying, conversion and conversion-alloying based electrodes with related schematic representation of the reaction mechansim (**Figure 2 d**). Alloying anode materials (see **Figure 2 a**), which exhibiting slightly higher working potentials than hard carbons and good capacity, promising high achievable cell energy density values. Conversion-type electrodes generally show even higher capacity and operating voltage (see **Figure 2 b**), but large voltage hysteresis between sodiation and desodiation arising from the poor reversibility of the conversion reactions. However, the combination of the alloying and conversion mechanisms in anode materials may represent a strategic way to obtain lower voltage values and reduced hysteresis (**Figure 2 c**). [32]

2.2. Irreversible Capacity

The irreversible capacity generally observed during the first sodiation process is mainly attribute to the formation of the SEI and other parasitic secondary reactions occurring between the electrolyte solution and the anode material. The formation of a stable SEI is strongly desirable to obtain high Coulombic efficiency values upon cycling. However, it has been reported that the SEI formed in sodium systems is very unstable due to the high solubility of the SEI components, thus strongly affecting the electrochemical performance due to a continuous electrolyte decomposition taking place at every cycle. [30] The first cycle irreversible capacity is even exhacerbated when getting to nanostructured electrodes, in which the higher surface area leads to increased amount of electrolyte decomposition. In addition, respect to insertion-type electrodes, alloying and conversion systems may lead to increased irreversible capacity due to irreversible structural reorganization occurring upon the first sodiation process. These phenomena represent a challenging issue for the application of the anode material in full sodium-ion cells requiring a very unfavorable electrode balancing with respect to the reversible cell capacity. The first irreversible capacity is generally mitigated through a

"pre-activation" step. This process is constituted by a pre-sodiation, which may be achieved through the contact of the electrodes with sodium metal or via electrochemical activation. [36-38] A smarter strategy proposed involves the use of sacrificial salts. [39] This strategy requires the conversion of the anion of the employed salt into gas, e.g., N_2, CO, or CO_2, upon the first charge and the generation of extra sodium ions able to compensate the irreversible capacity. [40] Additionally, the use of additives in the electrolyte solution, already demonstrated in LIBs systems, is expected to improve the overall coulombic efficiency and SEI stability upon cycling. [15, 41]

2.3. Specific Capacity

The specific capacity of anode materials is a critical parameter for their electrochemical performance. The theoretical capacity of a material is directly related to its ability to store sodium ions. Generally, the determining factors are represented by the available space to accommodate ions, the ability to change valence state and the degree of reversibility of the reactions. A significant breakthrough in the energy density of sodium-ion cells may be achieved by employing beyond-insertion anode materials. Indeed, alloying and conversion-type materials allow the achievement of higher specific capacity values implying multiple electron exchange per metal atom involved in the electrochemical process. However, these classes of compounds require nanostructuring to operate effectively making worth mentioning that the generally low density and high porosity of nanomaterials strongly affect the energy density of the final system, especially the volumetric one, despite the high theoretical and experimental (sometimes) capacity values.

2.4. Cost and Sustainability

Beside the lower cost and larger availability of the raw materials employed in SIBs with respect to LIBs, such as Na_2CO_3 (25-30 times cheaper than Li_2CO_3), other big advantages are achieved via the use of aluminum as current collector at the anode side, since sodium does not alloy with it. This represents a predictable cost cut and a further advantage in terms of weight of the total cell. It has been recently reported that even considering the lower cost of Na-precursors, still the cost cut is not sufficient to compensate for the lower energy density of SIBs when compared with LIBs. [42, 43] In this regard, the use of low cost and abundant raw materials is a mandatory selection criterion for the identification of the electrode materials. The synthesis procedure adopted to obtain such electrode materials should also be considered as one of the main factors affecting the overall cost. Obviously, improving the specific energy of the materials along with their cycle life is also necessary for the achievement of a tangible cost reduction. In this context, advanced anode materials play a crucial role and their screening should take into account key performance metrics such as working potential, specific capacity, reversibility and cost-effectiveness.

2.5. Beyond-insertion Anode Materials: Electrode Nanostructuration

In a continuous effort of the research community to achieve high performance rechargeable batteries, electrode materials exhibiting new reaction pathways have been investigated granting a breakthrough with respect to the standard, insertion-type materials. [32] Electrochemical processes involving alloying, conversion and the combined conversion-alloying mechanism enable the achievement of much higher specific capacity values thus representing an intriguing class of compounds for the next generation anode materials for SIBs. However, these materials require nanostructuration to effectively take advantages of the main features in the practical use for batteries. Accordingly, in the next session a brief overview on the advantages and disadvantages of

nanostructuration is given followed by a detailed overview of the literature available on alloying, conversion and conversion-alloying anode materials.

3. Nanomaterials in Rechargeable Batteries

Nanomaterials presenting one or more characteristic dimensions within the 1-100 nm range offer unique mechanical, electrical and optical properties respect to the same materials prepared in a bulk state. The ability of preparing, controlling, and manipulating materials at the nano-scale has strongly influenced several research fields including electrochemical energy storage. In lithium-ion batteries and supercapacitors, the effect of nanostructuration has been largely investigated. [44]

A brilliant example of the beneficial effect of nanostructuration is represented by the case of $LiFePO_4$, which could be used in commercial batteries only after the implementation of a thin conductive carbon coating and a proper particle size reduction. [45-48]

Nanostructuring has also demonstrated in the past the potential to enable new reaction mechanism in LIBs, such as the conversion reaction investigated by Poizot et al. [49] The particle size effect on this class of materials has been further investigated demonstrating the great improvement in the electrochemical process of Li storage by using nanometric rather than micrometric hematite (α-Fe_2O_3) particles (see **Figure 3**). [50] A more recent study underlined the importance of the particle size of monodisperse Sb nanocrystals for application in both LIBs and SIBs. The specific capacity, rate capability, and cycling stability in both Li and Na cells were strongly influenced by the particle size. [51]

Being characterized by a similar working principle of LIBs, the nanostructuration of SIBs' materials is expected to present similar aspects. Nano-size and tailored morphology of electrode materials enable a better accommodation of the strain associated to the (de-)sodiation process, especially in

those materials presenting high volumetric deformation upon cycling. In addition, the high surface to volume ratio typical of nanomaterials leads to the substantial decrease of the solid-phase diffusion paths for the Na^+ ions. Indeed, the diffusion time for ions (and electrons) is strongly decreased respect to bulk materials since it is proportionally related to the square of the diffusion length, thus enabling improved rate capability and power performance. [52] The high surface area of nanoparticles also offers improved contact between the electrode and electrolyte facilitating the charge transfer processes and, thus, enhancing rate capability. [44, 53] However, nanostructured materials carry several issues related to their use. Indeed, their implementation results in decreased electrode densities leading to low volumetric energy, while the high surface area exposed to the electrolyte may accelerate undesired side reactions producing unstable and thick SEI. Moreover, the potentially more complex synthesis of nanomaterials and the potential hazards associate with their handling should be considered as important factors affecting the final cost.

Figure 3 reports a schematic summary of the properties with related advantages and disadvantages of nanomaterials employed in rechargeable batteries.

The implementation of nanostructured electrode materials in rechargeable batteries constitutes a real challenge. However, effective strategies aimed at exploiting the advantages of nanostructures and mitigating its disadvantages, may represent a real step forward the achievement of high performance and long lasting SIBs. The careful and rational design and fabrication of nanostructured electrode materials are crucial and represent the key turning points for the development of enhanced batteries. Nonetheless, the beneficial effects of nanotechnology find a perfect application field in the advancement of anode electrodes, especially those employing alloying or conversion reaction mechanism. In fact, the large volumetric expansion occurring in these materials results in

the mechanical instability of the SEI and the electrode upon cycling leading to exacerbate capacity fading with respect to insertion-based electrodes.

4. Nanostructured Alloying Anodes

Materials exhibiting reversible ability to alloy with sodium have attracted much attention in the search of high energy density anodes for SIBs. Indeed, a quite large number of metals and nonmetals such as tin, antimony, bismuth, lead, germanium, and phosphorus offer high theoretical capacity values as a result of the multiple electron exchange associated with the alloying process. However, it is well known that they suffer from severe structural changes upon cycling associated with large volume expansion and consequent electrode disintegration and capacity fading. For instance, tin (Sn) alloys with sodium at relatively low potentials (0.21 V *vs* Na/Na^+) to form $Na_{15}Sn_4$ with a correspondingly high theoretical specific capacity (847 mAh g^{-1}). However, the electrochemical sodiation leads to a huge volume expansion of about 420%. [54, 55] The freshly exposed electrode material upon every alloying cycle implies a continuous electrolyte reduction strongly affecting the overall coulombic efficiency and cycle life. In addition, slow reaction kinetics lead to inferior rate capability and power performance with respect to insertion-based materials. To address these issues, enormous research and technological efforts in terms of nanostructuration have been devoted. The performance of the most promising systems (Sn, Sb and P) is summarized in **Table 1**. Owing to the nanostructured nature, the alloying mechanism reversibility and the cycle life have been improved through rationalized structure and morphology design in combination with optimized electrode and electrolyte formulation.

4.1. Tin

Metallic Sn is one of the most intensively investigated anode material for room-temperature SIBs, due to its ability to alloy up to 3.75 Na per Sn, corresponding to the high theoretical capacity of 847 mAh g^{-1}. The electrochemical storage mechanism of Na into Sn was firstly reported by Ellis *et al*. [56] They proposed a sodiation process divided into four steps leading to $NaSn_3$, NaSn, Na_9Sn_4 and $Na_{15}Sn_4$, respectively. Further investigation on microstructural changes and phase transformations on sodiated Sn nanoparticles using *in situ* transmission electron microscopy proposed a two-step sodiation mechanism, in which the amorphous Na-poor phase Na_xSn (x ~ 0.5) was initially formed (first step) consuming the pristine Sn. [57] Upon further sodiation, several Na-rich amorphous phases (Na_3Sn, Na_9Sn) up to the final crystalline $Na_{15}Sn_4$ phase (second step) formed. The use of Sn nanoparticles enabled the direct observation of the amorphous phase formed during the first step, which revealed a lower volumetric expansion respect to the final crystalline phase, highlighting the beneficial effects of nanostructures in combination with amorphization of the material leading to a better accommodation of the stress induced by the volume change. Commercial Sn nanoparticles were primarily tested in aprotic Na cells delivering ca. 500 mAh g^{-1} for more than 20 cycles with a 1st cycle coulombic efficiency of 86%. These results underline as the use of nanoparticles by itself may not represent the ultimate solution, but, when combined with proper electrode and electrolyte optimizations, may lead to superior performance as for the use of poly(acrylic acid) (PAA) as binder and fluoroethylene carbonate (FEC) as electrolyte additive. [58] Beyond the use of optimized battery components and the importance of amorphous phases, other strategies aimed at the improvement of electrode performance have been proposed. Among them, the use of inactive elements in the alloying matrix, able to accommodate volume expansion upon cycling and limit electrolyte decomposition, represents an attractive route. It has been successfully reported that the

substitution of Sn with Cu, in η-Cu_6Sn_5 leads to an improved passivating behavior of the electrode surface, limiting the catalytic activity of tin toward carbonate-based electrolyte, [59] however, with limited specific capacity due to the restricted Na diffusion into the nanoparticles. [60]

Using other electrochemically active elements in combination with Sn, is a potential method for improving the electrode stability without sacrificing capacity. Several binary and ternary Sn-based alloys, *i.e.* Sn-Ge, [61] Sn-Ge-Sb, [62] Sn-Bi-Sb, [63] have shown considerable improvements in terms of reversible capacity and cycling stability. Such materials can be synthesized via chemical vapor deposition, [64] physical vapor deposition, [62] high-energy mechanical ball-milling, [65] and rapid solidification. [66] Among them, SnSb binary alloys attract particular interest because of their high capacity, low working potential, and improved structural stability upon cycling. [67-70] Minimization of capacity decay and improvement of the alloying process reversibility can be achieved by particle size reduction and implementation of conductive carbon additives improving both the electron transport properties and acting as buffering matrixes for the volumetric deformation. For instance, Ji *et al.* synthesized porous carbon nanofiber-supported SnSb nanocomposites through electrospinning technique followed by a thermal treatment process, showing a high reversible capacity of 350 mAh g^{-1} at 0.2 C (coulombic efficiency ≥96%) and excellent capacity retention of about 99.4% for more than 200 cycles. [71] The improved performance of these nanocomposites undoubtedly benefits from nanostructuration and incorporation of conductive carbon. Nonetheless, the use of electrolyte additives such as FEC plays a crucial role in the formation of a stable SEI preventing further electrolyte decomposition upon cycling and thus greatly enhancing the coulombic efficiency (**Table 1** shows all the electrolytic media employed in the reported studies).

Introducing carbon-based conductive additives not only mitigate the mechanical strain and provide conduction pathway, but present another great beneficial effect toward the limitation of Sn agglomeration upon cycling. Xu *et al.* firstly reported the *in situ* synthesis of Sn nanoparticles (~100 nm) embedded in mesoporous carbon matrix via carbonization. [54] Unfortunately, the porous C/Sn anodes exhibited large irreversible capacity and poor rate capability, resulting from the development of a thick SEI layer and high charge-transfer resistance. Although *in situ* growth of nanosized Sn in mesoporous carbon can efficiently enhance the reversibility and coulombic efficiency, the rate capability and capability retention still require further improvement for practical application. The limited performance may be attributable to the structure and morphology of the carbon additive employed, which may act as inert layer and slow transport kinetics associated with the large size of Na ions. In this regard, graphene, owing to its open conductive template with high conductivity and surface area, represents a promising carbon host for Sn nanoparticles. Jeon *et al*. electrodeposited Sn nanoparticles with dimension ranging from 15 nm to 40 nm on reduced graphene oxide-graphene scaffold. [72] The material delivered an initial capacity of 615 mA h g^{-1} with an initial coulombic efficiency of 62%, and maintained 84% of the initial capacity after 50 cycles. However, the presence of functional groups in reduced graphene oxide (rGO) generally leads to rather low coulombic efficiency and affects the cycling stability due to undesired side reactions with the electrolyte. Interestingly, Luo and coworkers fabricated a nanostructured composite of backboned graphene matrix with Sn nanoparticles *via* high temperature, carbothermal method. [73] The material exhibited a reversible Na-ion storage capacity of 413 mAh g^{-1} at 100 mA g^{-1} with negligible fading after 100 cycles. Moreover, the nanoparticle size and morphology control offers new opportunities to improve the overall Sn anode performance. It has been reported that the design of a Sn nanorods forest with

engineered core–shell structure on viral scaffolds vertically aligned on a metal substrate could considerably accommodate the volume expansion and suppress Sn aggregation during extended electrochemical cycling, thus improving the overall performance including reversibility. [74] In the same pursuit, Sn-CNT nano pillar arrays, [75] Sn/C nanofibers, [76] and yolk-shell Sn/C nanocomposites [77] have demonstrated that a rational and engineered design of nanostructured electrodes lead to considerably improved sodium storage. As expected, the nanoparticle's size plays a crucial role on the final electrochemical performance in terms of both rate capability and cycling stability. Chen *et al.* designed ultrasmall Sn nanoparticles (~8 nm) homogeneously embedded in a spherical carbon hosting network achieving an initial reversible capacity of ca. 493 mAh g^{-1} at a current density of 200 mA g^{-1}. The material also exhibited high-rate capacity (349 mAh g^{-1}) when cycled at 4000 mA g^{-1} and stable capacity (415 mAh g^{-1}) after 500 cycles at 1000 mA g^{-1}. [78] The remarkably improved electrochemical performance is not only due to the well-suppressed volume expansion and particle aggregation during prolonged cycling, but also benefits from the much reduced charge-transfer resistance, indicating that the ultrasmall Sn nanograins homogeneously distributed in conductive carbon could facilitate sodium-ion diffusion.

The use of natural wood fiber as soft buffer in "binder free" or conductive binder (PFE) electrodes were engineered to ensure the reported high-performance of Sn anodes. [79, 80] Despite the great results achieved so far, it is important to consider that nanosizing and incorporation of carbon matrixes may significantly affect the volumetric energy density, thus pointing out the importance of optimized strategies to ensure the effect of particle size while maintaining a satisfactory Sn content in nanostructured Sn/C electrodes. As shown in **Figure 4**, encouraging results have been reported by Chen *et al*. with Sn nanodots (1-2 nm) encapsulated in porous N-doped carbon nanofibers (Sn

NDs@PNC) with a Sn content higher than 60%. Such a material made through electrospinning and thermal reduction, exhibited extraordinary electrochemical performance. Specific capacities of 450 mAh g^{-1} at 10000 mA g^{-1} and 483 mAh g^{-1} over 1300 cycles at 2000 mA g^{-1} were achieved. This is the best performance ever reported for Sn-based anode materials for SIBs, which can be attributed to the ultrasmall size of Sn and high conductivity of nitrogen-doped carbon fibers. [33] Carbon fibers acting as current collector/conductive additive, can also reduce the inactive weight and volume of cells, raising the innovative design concept of "free-standing anode" to improve the energy density. To date, however, the rate capability and cycling performance of metallic Sn anodes are still limited. To shed light on the practical application of Sn-based anodes for SIBs, several issues still need to be addressed. In view of the requirement needed, nanostructured modification could be a good strategy for achieving better performance keeping in mind also the requirement of high density electrodes and improved volumetric energy density. These requirements, however, may not represent a crucial issue for the application of SIBs in stationary energy storage systems.

4.2. Antimony

Metallic Sb-based materials have also attracted much interest as alloying anodes for room-temperature SIBs due to its high theoretical capacity of about 660 mA h g^{-1} and the relatively limited volume expansion with respect to other Na-alloying metals. A first attempt of using Sb/C nanocomposite anode for SIBs was reported by Yang and co-workers, demonstrating interesting performances employing an FEC-based electrolyte over 100 cycles with a specific capacity of about 600 mAh g^{-1}. [81] The investigation of the alloying mechanism between micrometric Sb and Na, was performed by Darwiche *et al*. in 2012, pointing out that the reaction mechanism involves the intermediate formation of amorphous phases while the competition between the formation of the

hexagonal and cubic (unstable at atmospheric pressure) Na_3Sb polymorphs takes place toward the end of the process. [82] Elucidating investigations on the alloying mechanism between Na and Sb have been comprehensively performed through in situ X-Ray diffraction [82] and Mössbauer spectroscopic analysis [83] despite the difficulties raised by the formation of amorphous intermediate phases. Recently, Allan *et al.* supplied additional information on the alloying mechanism via *in operando* pair distribution function (PDF) analysis and *ex situ* ^{23}Na magic-angle spinning solid-state nuclear magnetic resonance (MAS ssNMR) spectroscopy. [84] The inferior volume expansion involving the Na–Sb alloying to form hexagonal Na_3Sb and intermediate amorphous phases buffering the strain associate to the process are accounted for the improved cycling stability of the Na/Sb system ensuring outstanding cycling performance. In addition, it is worth noting that the working potential of Sb with Na is above 0.5 V *vs* Na/Na^+, suggesting the electrolyte to be less sensitive to decomposition than for Na/Sn systems. [82, 85] However, despite the above mentioned advantages of Sb, the high volume change (about 390% for the formation of Na_3Sb phase) and sluggish reaction kinetics during sodiation inevitably affect cycling stability and rate capability performance.

Much efforts were also devoted to improve the rate capability and capacity retention of Sb-based electrodes. One proposed strategy to mitigate these issues is to alloy Sb with inactive elements forming intermetallic compounds through high-temperature treatments. Cu_2Sb, [86] Mo_3Sb_7, [87] NiSb, [88] and Zn_4Sb_3, [89] have been investigated as anodes for SIBs, where the role of the inactive metal is to provide a mechanical buffer for the accommodation of volume changes that otherwise would lead to disintegration of the active material particles. It has been reported that Zn-Sb intermetallic nanowires display about 161% volume expansion after the first sodiation and 83% reversible volume change without any cracking or facture during the following cycles, suggesting the material as high

rate and stable anode materials for SIBs. He *et al.* systematically investigated the particles size effect on the performance of the Sb anode synthesizing monodisperse Sb nanocrystals in the 10-20 nm range and comparing with bulk Sb. [51] Interestingly, the capacity values exhibited by the 20 nm Sb particles electrode were better than that displayed by the 10 nm particles and bulk Sb. Authors attributed the lower capacity of the 10 nm Sb particles based electrode to the presence of the larger amount of an amorphous surface oxide shell leading to a higher irreversible capacity loss due to the formation of Na_2O.

Loading Sb nanoparticles into conductive carbon matrix to prepare nanocomposite electrodes in which porous carbon can accommodate the large volume expansion and immobilize the active nanoparticles has also been pursued. Mechanochemical synthesis has been pursued involving the milling of commercial Sb powders with various carbon templates, such as Super P, multiwall carbon nanotubes and graphitic carbon. [81, 90, 91] The process enabled the downsizing of Sb particles while ensuring their homogeneous distribution within the conductive carbon matrix. The Sb nanoparticles/graphitic carbon composite prepared by ball milling exhibited after 160 cycles a reversible capacity of 280 mAh g^{-1} when cycled at 1C showing a small average capacity loss (ca. 0.04−0.05% per cycle). [91] The stable and enhanced performance of these materials was mainly attributed to the formation of stable SEI and improved conductivity due to the graphitic carbon matrix. Ko *et al.* prepared ultrafine Sb nanocrystals embedded in carbon microspheres via spray pyrolysis process and carbothermal reduction, providing a cost-effective method to fabricate nanostructured heterostructures. [92] The Sb-carbon composite exhibited initial discharge and charge capacities at 0.3 A g^{-1} of 625 and 402 mAh g^{-1}, respectively, with a capacity retention of 90% after 100 cycles. The low Sb content in the Sb/C composites, however, led to lower initial capacities. With

a similar synthesis method (aerosol spray technique) Zhang *et al.* synthesized ultrasmall Sb nanoparticles (~10 nm) uniformly embedded in porous carbon spheres increasing the Sb content in the composite to about 69% in weight. [93] The spherical nano-Sb/C composite exhibited excellent rate capability and capacity retention of 88.5% after 500 cycles at 100 mA g^{-1}.

Different morphologies have also been investigated, developing Sb@C coaxial nanotubes through a facile carbon-coating process coupled with a thermal-reduction strategy. As shown in **Figure 5**, the Sb@C nanotubes exhibited superior rate capability and retained a stable capacity of 240 mAh g^{-1} at 1.0 A g^{-1} even after 2000 cycles. [94] Other interesting conductive matrix candidates are heteroatom-doped carbons. Recent reports have demonstrated that the use of N-doped carbon/carbon nanotubes provide superior electronic conductivity and strong interaction between Sb and N-doped defects, which efficiently improve the cycling stability and rate capability. [95, 96] Additionally, graphene attracted the most intensive attention as the introduction of highly stretchy and robust graphene layers can effectively buffer the strain associate to the alloying process and simultaneously provide contact and protection of the active materials. [97-99] Firstly, Nithya *et al.* fabricated rGO/Sb nanocomposites, which showed higher cycling stability most likely attributable to the improved conductivity and high surface area of the rGO matrix. [100] However, the presence of residual functional groups in rGO generally leads to the trapping of small amounts of Na ions, which is responsible for the irreversible capacity losses and low coulombic efficiencies. Interestingly, an antimony/multilayer graphene hybrid (Sb/MLG) composite was prepared by a confined vapor deposition method, with less residual functional groups. As a result, high reversible sodium storage capacity (452 mAh g^{-1} at a current density of 100 mA g^{-1}) and stable long-term cycling performance (90% capacity retention after 200 cycles with an average coulombic efficiency of >99%) was achieved.

[101] The promising properties of Sb/rGO have been also reported in a flexible and binder free NVP/rGO//Sb/rGO sodium-ion full cell. The developed cell prototype delivered a high reversible capacity of ~400 mAh g^{-1} (respect to the total mass of the anode) at a current density of 100 mA g^{-1} after 100 cycles. [102]

4.3. Phosphorus

Phosphorus represents an attractive anode candidate for SIBs in view of its abundance and eco-friendliness. Elemental P mainly exists in three allotropic forms, i.e. white, red and black. Among them, white P (P4) is highly toxic and flammable in ambient conditions, black P is the thermodynamically stable form at ambient temperature and pressure, and red P is nontoxic and does not undergo spontaneous combustion. [103, 104] Considering the high reactivity of white P and the harsh synthesis condition required to obtain black P, the most studied system for application in sodium-ion batteries is red P which is easy to prepare and commercially available. P offers the theoretical capacity of 2596 mAh g^{-1} (for its highest sodiated phase, *i.e.* Na_3P,) and relatively safe working potential (~0.45 V vs. Na/Na^+), thus promising elevated energy density.

Red phosphorus (RP) presents a polymeric chain-like structure constituted by covalently bonded P4 tetrahedra. The low atomic weight, large Na-uptake ability, and commercial availability make RP as one of the most promising anode material for SIBs. However, amorphous RP presents poor electrical conductivity ($< 1 \times 10^{-14}$ S cm^{-1}) and large volume expansion upon full sodiation to Na_3P (about 440%) leading to sluggish reaction kinetics and fast capacity fading. [105] Moreover, the resultant Na_3P surface is highly reactive with the electrolyte implying large irreversible capacity. [106] Recently, a chemical synthetic approach for preparing nanostructured red P was reported. [107] The prepared

hollow phosphorous nanospheres (HPNs) exhibit superior electrochemical performance, even with high loading ratio of P (60 wt.% of the electrode weight). Mechanical milling has also been reported as an efficient way to prepare nanostructured carbon composite electrodes. [108] In 2013, Kim *et al.* prepared amorphous RP/C composite via ball-milling RP and Super P carbon in the 7:3 weight ratio. [109] The composite showed reversible capacity of 1890 mA h g^{-1} at a current density of 143 mA g^{-1} (ca. 0.05 C rate), working potential of ca. 0.4 V vs Na/Na^+, good rate capability (1540 mA h g^{-1} at a current density of 2.86 A g^{-1}, ca. 1 C rate), and excellent cycling performance with negligible capacity fading over 30 cycles. The successful implementation of nanosized carbon matrices has also been reported for the hand ground mixture of commercial microsized RP with multiwalled carbon nanotubes (MWCNT). This composite material exhibited promising performance attributable to the buffering effect of the MWCNT for the P volumetric expansion and their improved electron transport properties. [110] Highly conductive graphene stacks as host for RP nanoparticles has been employed by Song*et al.* Benefiting from the chemical bonding between the graphene nanosheet and P nanoparticles, the developed nanocomposite delivered a high reversible capacity of 2077 mAh g^{-1} with excellent cycling stability (1700 mAh g^{-1} after 60 cycles at 260 mA g^{-1}) and high coulombic efficiency (~99%). [111] In addition, a further improvement of the performance was obtained by the synergetic combination of chemically bonded phosphorus-carbon nanotube (P-CNT) hybrid and crosslinked polymer binder enabling a more stable cycling capacity (ca.1586 mAh g^{-1} at 520 mA g^{-1} after 100 cycles). [112]

The cycling stability of these composites is strongly related to the carbon content and the P nanoparticles distribution into the conductive network. Pei *et al.* synthesized P nanoparticles encapsulated in graphene scrolls (P-G) with different P contents. Among these, the P-G composite

with a phosphorus content of 52.2% showed the best performance, delivering a capacity of 2355 mAh g^{-1} at 250 mA g^{-1} with a capacity retention of 92.3 % after 150 cycles. [114] Despite the beneficial effect of the conductive matrix, high concentration of carbon in the composite may lead to decreased electrode energy density. It has been reported by Zhu *et al.* that thermally deposited RP nanoparticles onto singe-walled carbon nanotube (60 wt.% carbon content) show superior long-term cycling performance with 80% capacity retention after 2000 cycles but with limited overall capacity of about 300 mAh g^{-1}. [115] In an effort to improve the P loading, Guo and coworkers utilized a graphene aerogel as host to fabricate a 3D integrated C/RP/graphene aerogel composite (C@P/GA) via an advanced vapor-redistribution strategy to achieve a uniform distribution of phosphorus nanoparticles (NPs) within the 3D graphene-based architecture as shown in **Figure 6**. This strategy enabled a relatively high P loading of more than 80%. The as-prepared C@P/GA electrode delivered a high capacity of 1867 mAh g^{-1} after 100 cycles at 0.1 C and demonstrated significant capacity retention of 1095.5 mAh g^{-1} after 200 cycles at 1 C rate. [113] In addition, the use of graphene or nitrogen-doped graphene as flexible substrates to fabricate binder free electrodes provides a new direction to improve the overall energy density of RP anodes with carbon integration. [116, 117] An improvement of the rate capability of P based electrodes enhancing the kinetics of the processes involved may be obtained by downsizing the RP particles to several nanometers. Indeed, Li *et al.* confined amorphous RP in highly ordered mesoporous carbon matrix (CMK-3) with uniform pore size distribution of about 4 nm. [118] The composite displayed a reversible capacity of 1020 mAh g^{-1} after 210 cycles at 5C. In addition, it has been reported that by confining nanosized amorphous RP into zeolitic imidazolate framework-8 (ZIF-8)-derived nitrogen-doped microporous carbon matrix with well-defined pore size (<1 nm), as shown in **Figure 7**, delivering 1990 mAh g^{-1} upon 1000 cycles at 1 C

rate. Such a good performance is attributed to the size of RP particle and their confinement in the mesoporous conductive carbon matrix strongly enhancing charge transfer properties. [119]

In addition to RP, Black phosphorus (BP) has also been reported for use as anode material in SIBs. BP is nontoxic, thermodynamically stable and electrically conductive. [120] Moreover, bulk BP exists in three known crystalline phases (orthorhombic, rhombohedral, and simple cubic), as well as in an amorphous form. As the orthorhombic BP possesses a layered structure and semiconductive character, it has been intensively investigated in electronics and optoelectronics. [121] The first experimental exploration of BP anodes for SIBs was carried out in 2013 by Qian *et al.* [108] Although black P showed an increased charge capacity respect to RP, the first cycle efficiency was lower than 30%. The improvement of BP performance in SIBs requires a comprehensive understanding of the sodiation mechanisms. It has been reported that, since BP has a larger interlayer distance (5.4 Å) than graphite (3.4 Å), Na ions storage into the BP layers should be facilitated with respect to graphite. [122] First-principles calculations performed by Hembram *et al.* proposed a two-step sodiation mechanism for BP, including an intercalation process up to the composition of $Na_{0.25}P$ and a following alloying reaction. [123] On the basis of its structural properties, a volume expansion of 390% (i.e., lower than for RP) is expected. Recently, Chen *et al.* proposed the degradation mechanism of BP during sodiation to be dominated by the sodium diffusion directionality and insertion strain, which result from the low diffusion barrier in the [100] direction and gradual transformation of the layered structure into amorphous, respectively. [124] Based on these results, two strategies have been proposed to improve the electrochemical performance, *i.e.* delamination into phosphorene or few-layer phosphorenes and carbon coating processes. Kulish *et al.* calculated the Na diffusion in phosphorene finding a very low energy barrier of 0.04 eV, thus suggesting phosphorene as a very

promising anode material for SIBs. [125] Liquid exfoliation method shows great potential for large-scale synthesis of two-dimensional materials, like ultrasonic and electrochemical exfoliation, however, limited by the difficulties in solvent removal. [126, 127] Interestingly, Huang *et al.* prepared few layered phosphorene (2 to 11) *via* electrochemical cationic intercalation. [128] When directly serving as anode material in SIBs, phosphorene delivered a capacity of 1968 mAh g^{-1} at 100 mA g^{-1}. However, the structural instability at ambient conditions and the synthesis method may obstacle its implementation in SIBs. [129] A carbon coating approach has been adopted to stabilize the structure. [130] Xu *et al.* prepared nanostructured BP composites with Ketjen black-multiwalled carbon nanotubes via high energy ball milling, obtaining high initial coulombic efficiency (>90%) and superior reversible capacity (~1700 mAh g^{-1} after 100 cycles at 1.3 A g^{-1}). [130] The implementation of 2D composite materials has been achieved by integrating phosphorene with conductive graphene in a sandwich-like structure (**Figure 8**). A hybrid material made out of a few phosphorene layers sandwiched between graphene layers showed a specific capacity of 2440 mAh g^{-1} at a current density of 0.05 A g^{-1} with capacity retention of 83% after 100 cycles. [131]

In addition, the use of engineered binders and proper electrolyte additives selection, which can contribute for the formation of a more stable SEI, play a vital role in the improvement of the irreversible capacity fading and cycle life for P anodes. [132] Therefore, taking advantage of the highly conductive carbon additives, effective strategies should be devoted to optimize the gravimetric and volumetric energy density of the composites. Considering the high theoretical capacity and abundance, RP-based materials could certainly be among the most promising anodes for SIBs.

4.4. Other Elemental Alloying Anodes

Silicon, [133, 134] germanium, [135] bismuth, [136] lead, [133] and indium, [137] have also been studied as potential anode materials for SIBs. Unlikely, silicon, the "holy Grail" but yet-to-be-proven anode materials for LIBs, [138] appears to be most likely electrochemically inactive toward sodiation. The theoretical capacity predicted for the formation of the fully sodiated NaSi phase is about 954 mAh g^{-1} and is expected to lead to a volumetric deformation of about 244%. [139] Komaba *et al.* studied crystalline Si (c-Si) nanoparticles (~100 nm) as anodes for SIBs, however, observing no redox behavior. [58] Theoretical calculations confirmed that the limited electrochemical reactivity is related to the large insertion barrier and energy difference between surface and sub-surface sites for Na^+ inserting into c-Si. [140, 141] Besides, Kulish *et al.* predicted that efficient Na storage might be achieved employing polysilane and silicene (single or few layer silicon nanosheets) compounds. [142] While c-Si does not represent a suitable choice as anode for SIBs under standard conditions, amorphous Si (a-Si) can accommodate 0.76 Na atoms per Si atom, corresponding to a specific capacity of 725 mAh g^{-1} with a volume expansion of 114% and a Na diffusivity of 7×10^{-10} cm^2 s^{-1} at room temperature. [143] Xu *et al.* firstly reported reversible sodium uptake into Si nanoparticles with a capacity of 279 mAh g^{-1} when cycled at 10 mA g^{-1}. [144] Although the system could not release the full theoretical capacity, it is worth noting that the improved reactivity of the c-Si/a-Si/SiO_2 hybrid developed benefited from the nanosized Si particles (20 nm), which are advantageous for the kinetics of sodium ions diffusion and the favorable Na insertion in a-Si. Meanwhile, Hu et al. prepared the Si/C nanocomposite by high-energy balling of commercial Si microparticles and graphite powers, which achieved enhanced sodium-storage properties enabled by the formation of numerous nanodomains of Si and amorphization of graphite. [145] Inspired by the result, Zhang *et al.* revisited the investigation of sodium uptake into c-Si. [146] A specific capacity of 438.2 mAh g^{-1} at 50 mA g^{-1} was achieved and

superior reversible capacity was maintained at high rate (200 mAh g^{-1} at 5000 mA g^{-1} after 2000 cycles). The electrochemical activity observed is attributed to the irreversible crystal structure conversion of c-Si into a-Si during the first sodiation step, guaranteeing the formation of a new active phase for the reversible Na uptake. Moreover, the proposed carbon coating process and the nanostructured design further improved the conductivity and structural stability of the developed system.

Even though less studied, germanium (Ge) possesses a theoretical capacity of 396 mAh g^{-1} (based on the formation of the fully sodiated NaGe phase). A study on sodium diffusion at high temperature into crystalline germanium (c-Ge) conducted by Stojić *et al.* revealed slower kinetics when compared to those observed in lithium systems. [147] Indeed, c-Ge has been proved to be electrochemically inert for sodiation owing to the high diffusion barrier encountered by Na ions. [58] Nonetheless, Baggetto *et al.* [148] investigated amorphous germanium (a-Ge) thin films as negative electrode in SIBs achieving a reversible capacity of 350 mAh g^{-1}. Interestingly, preliminary XRD results indicated that the amorphous phase remained as such even after full sodiation. [148] Abel *et al.* prepared the nanocolumnar a-Ge film via glancing angle deposition, exhibiting a very high and promising capacity (430 mAh g^{-1}). This value is much higher than the theoretical value, thus suggesting the possibility of a different reaction mechanism involved. [135] In light of the higher electrochemical activity of the amorphous phases, activation of c-Ge nanowire and Ge thin films has been proposed through a preliminary lithiation-delithiation step to transform c-Ge into a-Ge. The strategy enabled the obtainment of a reversible capacity of 346 mAh g^{-1} and 418 mAh g^{-1} for c-Ge nanowires and thin films, respectively. [149] The same strategy has been employed by Lu *et al.* on c-Ge nanowires, which could be readily and reversibly sodiated by pre-amorphizing. [150] The results confirmed that a-Ge

exhibited a volume expansion of 300% during the formation of the $Na_{1.6}Ge$ sodiated phase. Moreover, it has been reported that the use of graphene for the obtainment of a hybrid composite, i.e. core-shell Ge@Graphene@TiO_2 nanofibers, exhibited superior cycling stability. [151]

Recently, it has been reported that bismuth (Bi) could be an interesting anode candidate for SIBs due to its theoretical capacity of 385 mAh g^{-1} (Na_3Bi), satisfactory working potential (0.6 V *vs* Na/Na^+) and relatively lower volumetric expansion (250%). [133] The Bi/graphene nanocomposite synthesized by Su *et al*. via hydrothermal reaction exhibited a high reversible sodium storage capacity of 561mAh g^{-1}. *Ex situ* XRD investigation evidenced that due to the large interlayer distance of the layered Bi structure, the reaction mechanism taking place is intercalation-like rather than alloying. [136] Other promising systems in terms of electrochemical performance have been proposed, such as Bi nanoparticles embedded on carbon spheres or nanofibers prepared by carbothermal reduction, enabling high reversible capacities. [152, 153] However, the flammability of Bi makes this element less appealing for future application in SIBs. Other elements with the ability to alloy with Na, such as lead (Pb) and indium (In), have been reported with theoretical capacities of 485 mAh g^{-1} ($Na_{15}Pb_4$) and 467 mAh g^{-1} (Na_2In). However, considering the associated cost, environmental and safety issues associated to their use, the interest is very limited.

Many efforts have been devoted to the improvement of alloying based systems and, as reported above, promising results have been achieved. However, as pointed out in this and previous reviews, [154, 155] the most common strategies to overcome the issues affecting the electrochemical performances consist of implementing nanosized active material particles, designing nanostructured electrode to better accommodate the volume expansion and/or using buffering matrixes or conductive agents to improve the alloying kinetics and cycling stability. The efficient implementation

of nanostructuration and engineered morphologies can certainly represent an efficient strategy for the improvement of the current state-of-art alloying anodes, however, much effort should be devoted to the stabilization of the sensitive SEI formed on alloying materials, which represents a quite thought challenge considering the high solubility of sodium-based SEI components into organic solvents of electrolytes. [30, 156] The development of artificial SEI and the use of optimized electrolyte solutions may represent a key turning point for the real application of alloying systems in SIBs.

5. Nanostructured Conversion-type Anode Materials

Conversion reactions have been studied for application in LIBs since the late 70s [168] and 80s [169], however, the turning point is represented by the pioneering work on nanosized transition-metal oxides conducted by Poizot *et al*. [170] Interestingly, after the discovery, great efforts and interest were devoted to the design of nanostructured materials for application in energy storage opening new avenues for the development of innovative and high performance electrochemical energy storage systems. The reaction generally occurring on transition metal compounds (M_aX_b, M = transition metal, X = H, F, O, S, N, P etc.), involves multiple electron exchange per transition metal and is characterized by high theoretical specific capacity. The conversion mechanism during sodiation implies the reduction of the active material into metallic nanoparticles embedded in a Na_2O matrix. The specific capacity of conversion-type electrode materials can be increased by using transition metals compounds with high oxidation state of the metal involved in the electrochemical process. Additionally, since the working potential at which the conversion occurs depend on the ionicity of M-X bond; the electrochemical potential can easily be tuned according to the desired application. [171, 172] Transition metal oxides, sulfides, nitrides and phosphides (with M_aX_b as general formula) are conversion-based electrode materials, which have been explored for both LIBs and SIBs.

[173] However, they generally suffer from low initial coulombic efficiency, poor cycling stability, and low energy efficiency due to the high voltage hysteresis observed upon cycling. The voltage hysteresis is an intrinsic feature of the conversion reaction and is the result of ohmic voltage drop, reaction overpotential (proportional to the ionicity of the M-X bond), and different spatial distributions of electrochemically active phases (*i.e.* compositional inhomogeneity). [174] In addition, the sodium storage behavior is strongly affected by the large volume expansion following the conversion reaction as well as the consequent electrolyte decomposition accelerated by the presence of new, freshly exposed electrode area after every conversion cycle. It has been proved that exploitation of nanostructured materials can effectively alleviate the strain derived from the volume change, resulting in enhanced capacity retention. [44, 148] Furthermore, nanostructured materials can provide large electrode-electrolyte contact area and shorten diffusion length of Na ions in electrode leading to higher rate capability, however, at the expense of faster electrolyte decomposition. The large hysteresis observed during the conversion reaction can be mitigated by rational design and optimization of material microstructure and electrode architecture, thus improving the energy efficiency of SIBs based on conversion chemistry. A wide range of oxides, sulfides and phosphides have been investigated as anode candidates in SIBs, such as Fe, Cu, Co, Ni, Mo, W, and other as well as their binary compositions. [175-181] Hereafter, we will provide an overview on nanostructured design and recent progress towards conversion-type electrodes in SIBs. A detailed list of materials with their performance is reported in **Table 2**.

5.1. Transition Metal Oxides

Transition metal oxides (TMOs) with general formula of M_xO_y (M = Fe, Co, Cu, Mn, Ni, Mo) have been studied as potential anode materials for SIBs, due to their ability to react with Na converting into

metal nanoparticles dispersed in a Na_2O matrix. Tirado *et al.* firstly reported the use TMOs as conversion-type anode for SIBs. [182] The proposed $NiCo_2O_4$ spinel delivered a reversible capacity approaching 200 mA h g^{-1} by forming Na_2O, Ni and Co upon sodiation. Following, other spinel-type materials such as $MnFe_2O_4$ [183] and $MgFe_2O_4$ [184], synthesized by hydrothermal and microwave assisted method, respectively, were tested. Beyond the interesting properties such as natural abundance, low cost and toxicity of the employed raw materials, the materials exhibited satisfactory electrochemical activity when processed into composites with graphene. Balaya *et al.* reported the study on α-MoO_3 showing a first sodiation and de-sodiation capacity of 771 and 410 mAh g^{-1} respectively, suggesting interesting sodium storage ability comparable to carbon based and $Na_2Ti_3O_7$ anode materials. [175] However, despite the promising properties of such materials, their electrochemical performance in Na cells is strongly affected by large volumetric and structural changes, poor cycling stability and low energy efficiency governed by the high voltage hysteresis.

Among the TMOs, iron oxides, in particular Fe_3O_4 and Fe_2O_3, have drawn particular attention because of their high theoretical capacity approaching 1000 mAh g^{-1}, non-toxicity, high abundance, low cost and high corrosion resistance. [186, 187] However, when tested in sodium half-cells, α-Fe_2O_3/C and Fe_3O_4/C nanowires electrodes exhibited very low reversible electrochemical activity. While a partial sodium insertion was observed, authors could not observe the conversion reaction suggesting that particle size may play a role in the reaction mechanism. [188] Balaya *et al.* proposed a dual-alkali ions conversion storage in Fe_3O_4 anode for both LIBs and SIBs. [189] While for the lithium based system the electrodes exhibited excellent performance both in half and full-cell configuration, in sodium cells, the electrode delivered a first sodiation capacity far below the theoretical value and a reversible charge capacity of about 366 mAh g^{-1}, suggesting the incompleteness and poor

reversibility of the conversion process. The limited performance may be primarily attributed to the sluggish kinetics of Na ions storage due to the large ionic radius of Na ions. [189] Kumar *et al.* investigated strategies to improve the redox activity of Fe_3O_4 by using alginate binder. [190] Due to the strong bonding between Fe_3O_4 nanoparticles/alginate, the developed composite maintained a stable discharge capacity of 248 mAh g^{-1} after 50 cycles with 98% coulombic efficiency. With the purpose of improving the cycling stability and the electronic properties of Fe_3O_4, Liu *et al.* synthesized Fe_3O_4 quantum dots with average size of 4.9 nm on 3D graphene foam by a facile one-pot hydrothermal approach. [191] The 3D-0D graphene-Fe_3O_4 hybrid composite exhibited high sodium storage capacity (525 mAh g^{-1} at 30 mA g^{-1}), outstanding cycling stability (312 mAh g^{-1} after 200 cycles at 50 mA g^{-1}) and superior rate performance (56 mAh g^{-1} at 10 A g^{-1}). Recently, Qi *et al.* demonstrated that MOF-derived Fe_3O_4 quantum dots embedded in mesoporous carbon could reach supercapacitor-like rate performance due to the short diffusion length and hierarchical conductive network. [185] Following, Oh *et al.* proposed the sodium-ion battery constituted of the nanosized Fe_3O_4/C anode coupled with layered $NaNi_{0.25}Fe_{0.5}Mn_{0.25}O_2$ cathode as a well-performing low-cost energy storage system. [193] Among all polymorphs of Fe_2O_3, the γ cubic phase has been investigated in sodium cells exhibiting a three electron reduction ($Fe^{3+} \rightarrow Fe^0$) starting at 0.5 V and a reversible two-step oxidation ($Fe^0 \rightarrow Fe^{2+}$ and $Fe^{2+} \rightarrow Fe^{3+}$) at ~1.0 and 1.4 V. [194] Chen and coworkers synthesized a 3D porous γ-Fe_2O_3/C nanocomposite by aerosol-assisted method as shown in **Figure 9.** The γ-Fe_2O_3 nanoparticles (5 nm) were uniformly embedded in the porous carbon matrix, showing a reversible capacity of 740 mAh g^{-1} after 200 cycles at 200 mA g^{-1} and high-rate performance with a discharge/charge capacity of 317 mAh g^{-1} at 8000 mA g^{-1}. [185] Benefiting from the wide investigations in LIBs, various nanostructured iron oxides were tested in SIBs. [186] Recently, Yu *et al.* indicated hydrated iron oxide in the β‑FeOOH

phase, simply synthesized via hydrolysis, as an interesting conversion-anode for SIBs. [195] However, the material with smaller particle size (5 nm) presented poorer kinetics and larger overpotential than the material with larger particles (53 nm). The reversible extraction of Na^+ from the Na_2O matrix seems to be thermodynamically unfavorable due to the large ionic radius of Na, suggesting that the alkali ion size may be an intrinsic limit to the reversibility of conversion reactions in SIBs.

Co_3O_4 presenting a theoretical capacity of 890 mAh g^{-1} has also been investigated as anode material for SIBs. Rahman *et al.* demonstrated the feasibility of the conversion reaction using nanostructured Co_3O_4, which exhibited a reversible capacity of 447 mA h g^{-1} at 25 mA g^{-1} and ~86% capacity retention after 50 cycles. [197] However, also in this case the full theoretical capacity was not achieved during the discharge process, resulting in inferior electrochemical performance. Longoni *et al.* investigated the conversion mechanism of Co_3O_4 powders and the morphology-performance correlation by synthesizing different morphologies prepared through hydrothermal method. [198] Needle-like, nanometric Co_3O_4 exhibited the most promising performance, especially in combination with a pre-sodiation treatment to reduce the initial irreversible capacity, further improving the cycling stability. [198] In order to improve the electronic conductivity of Co_3O_4, conductive carbon nanotubes have been introduced via co-precipitation and thermal decomposition. [199] The Co_3O_4/CNTs exhibited high capacity and good rate capability when used with an FEC-added electrolyte. Another promising approach to facilitate the conversion reaction of Co_3O_4 is the synthesis of well-defined mesoporous microstructures. Yang *et al.* investigated the dual porosity, mesoporous Co_3O_4 using mesoporous silica (KIT-6) as sacrificial template. [200] The defined porosity enabled the mass transport of electrolyte into the pores and provided a higher electrolyte adsorption generating improved transport pathways respect to the more common Co_3O_4

nanostructures. The material showed a capacity of 707 mA h g^{-1} at a current density of 90 mA g^{-1} and a satisfactory capacity retention after 100 cycles. Recently, metal-organic frameworks (MOFs), also known as porous coordination polymers (PCPs), synthesized by assembling metal ions with organic ligands have emerged as a new class of crystalline, but porous materials. Using MOFs as templates to design and fabricate electrochemically nanostructured active materials (porous carbons, metal oxides, metal oxide/carbon hybrids, etc.), which are rapidly explored for LIBs. [201, 202] Wang *et al.* proposed the use of ZIF-67 as template (the organic linkers contain N and C atoms) to synthesize Co_3O_4/nitrogen doped carbon (NC) core-shell structure (~5 nm Co_3O_4 is the core and 2-3 nm NC is the shell). When investigated as anode for SIBs, as shown in **Figure 10**, the composite delivered a capacity of 506 mAh g^{-1} at 100 mA g^{-1} and 263 mAh g^{-1} at 1000 mA g^{-1} with a capacity decay of only 0.03% per cycle for 1100 cycles. [196] A key structural feature of MOFs is their high porosity as well as high surface area, which play a crucial role in the functional properties. A stable Co-based MOFs (Co-TATB) was used to fabricate a composite of porous and hollow Co_3O_4 polyhedron with N-doped carbon coating offering high and stable capacity. [203] The impressive electrochemical performance of these MOF-derived materials is attributed to their ability to activate capacitive and conversion storage processes enabled by the superior conductivity of NC and the ultrafine nanostructure of Co_3O_4. Recently, capacitive charge storage, distinguished from the conventional diffusion-controlled process, has demonstrated to offer superior high-rate performance and reversibility for energy storage in battery systems. [204, 205] In this respect, Dou *et al.* synthesized atomically thin Co_3O_4 nanosheets via a bottom-up self-assembly approach, presenting excellent rate capability and the average discharge capacity of 427 mAh g^{-1} at 500 mA g^{-1}. [206] The results indicate that two-dimensional (2D) materials with extremely large surface area could provide

more active sites for capacitive Na^+ storage and contribute largely to the improved reversibility. Accordingly, Chen *et al.* demonstrated a scalable template-directed synthesis of 2D Co_3O_4 nanosheets with holey architecture (HACN) as shown in **Figure 11 a**. [207] The as-synthesized material, HACN-10 with 10 nm holes, delivered a high reversible capacity of 566 mAh g^{-1} at 100 mA g^{-1} and good cycling stability after 100 cycles (**Figure 11 b**). *In situ* TEM analysis revealed the conversion reaction to occur in the local interface of Co_3O_4 and Na_2O with short Na^+ diffusion length. Additionally, the holy structure greatly buffered the volume change (~6%) after sodiation. The above results suggest Co_3O_4 as a very promising anode to be used for long life and high-power SIBs.

In addition to Fe and Co oxides, also CuO has been investigated as potential conversion anode for application in SIBs due to its lower cost than Co, environmental friendliness and high theoretical capacity of about 674 mAh g^{-1}. [173, 208] Wang *et al.* prepared porous CuO nanowires exhibiting an initial capacity of 640 mAh g^{-1} and 303 mAh g^{-1} after 50 cycles at 50 mA g^{-1}, through a multi-step process. During the discharge step, Na ions insertion into CuO leads to the formation of the $Cu^{II}_{1-x}Cu^{I}_{x}O_{1-x/2}$ solid phase, followed, upon further sodiation, by the formation of Cu_2O (and Na_2O), which finally decomposes to metallic Cu nanoparticles embedded into a Na_2O matrix. The reversible charge process leads to the oxidation of the Cu nanoparticles to Cu_2O eventually converting back to CuO. [209] In an effort to facilitate the reaction mechanism, Yuan *et al.* fabricated *in situ* a flexible and porous CuO array by simply engraving commercial copper foils. [210] The binder-free electrode exhibited high capacity (over 640 mAh g^{-1}) even at a high current density of 200 mA g^{-1}, however, with limited cycling stability most likely attributable to the poor conductivity and large volume change upon cycling. To mitigate these issues, Jiao *et al.* synthesized CuO quantum dots (~2 nm) in carbon nanofibers via a facile electrospinning method. The material delivered a high reversible

capacity of 528 mAh g^{-1} at 500 mA g^{-1}, only slightly decreasing to 401 mAh g^{-1} after 500 cycles. Additionally, CuO/C composites derived from various Cu-based MOFs have been reported. [211-213] Interestingly, there is an inferior number of studies related to FeO, CoO, NiO and MnO anode materials in SIBs compared with LIBs, since they show poor electrochemical activity in Na-cells when compared to the excellent performance exhibited in Li-cells. [214] As a matter of fact, due to the larger Na^+ radius, the sodiation based on conversion reaction is expected to be thermodynamically poor in these oxides. Su *et al.* investigated the sodiation reaction mechanism of NiO nanosheets through *in situ* transmission electron microscopy (TEM) observation and molecular dynamic (MD) simulation, revealing that the sodiation process is hindered by the formation of a passivation layer of Na_2O formed at an early stage of the conversion, which result in sluggish kinetics. [215] This may explain the low rate capability of TMOs for SIBs. Some contradictory results on the Co/CoO/carbon, [216] NiO/Ni/Graphene, [217] and MnO/C nanorod [218] hybrids derived from their MOFs precursors have been reported. Indeed, the materials showed electrochemical activity with Na, however, the reaction mechanism still remains poorly understood and the complex intermediate species formed during sodiation still require detailed characterization for a deeper understanding.

5.2. Transition Metal Chalcogenides

Transition metal chalcogenides (TMCs) represent an additional class of conversion-type electrodes as promising alternative to conventional TMOs anode for SIBs. Assuming the complete reaction of TMCs with Na, metallic particles and sodium chalcogenides are eventually formed in the fully discharged state, giving rise to high theoretical capacities. One of the most promising compounds are sulfides, which are characterized by smaller volume changes during charge/discharge and more reversible conversion process respect to oxides, conferred by the higher conductivity of Na_2S and

weaker M-S bond. However, the critical issues of conversion based materials, even if mitigated, still need to be addressed. The voltage hysteresis related to the structural change, as defined in TMOs, may be relieved by the implementation of nanostructured electrode. In addition, the conversion mechanism of sulfides compounds generally proceeds through the formation of intermediated products such as polysulfide anions (S_x^{n-}), which are highly soluble in organic electrolytes representing a severe issue for the cycling stability, electrode integrity and, even safety. To date, many research efforts have been devoted to the improvement of the performance of metal sulfides via nanostructure design, composition tuning and hybridization with conductive/protective materials.

Pyrite FeS_2, a natural mineral, has been widely investigated in LIBs as positive electrodes. [220, 221] In the field of SIBs, natural FeS_2 has been investigated as potential anode material because of its high theoretical specific capacity (894 mAh g^{-1}). [222] However, it has been reported that both, natural and synthesized by mechanical alloying FeS_2 exhibited large capacity fading during repeated charge-discharge cycling. [223] The enhancement of the cycling performance relies so far in a deeper understanding of the sodiation mechanism during the conversion reaction. It has been reported that the conversion reaction of FeS_2 with Na proceeds through the intermediate formation of Na_xFeS_2 at about 0.8V (*vs* Na/Na^+), eventually ending into metallic Fe along with the formation of Na_2S. [224] Hu *et al.* confirmed that such an intercalation reaction also occurs in Na/FeS_2 cells suggesting that the cycling performance could be significantly enhanced via tuning the cut-off voltage to 0.8 V (*vs* Na/Na^+) while using $NaSO_3CF_3$/diglyme electrolyte. [225] Indeed, they observe that the electrically conductive, layered Na_xFeS_2 was formed upon sodiation, enabling reversible sodium intercalation to occur. Microspheres composed of tightly aggregated FeS_2 nanoparticles (~200 nm) delivered a surprisingly high-rate capability (170 mAh g^{-1} at 20 A g^{-1}), most likely attributable to capacitive behavior, and

unprecedented long-term cyclability (~90% capacity retention for 20 000 cycles). Walter *et al.* synthesized FeS_2 nanocrystals (NCs) in 50-100 nm via solution-based chemical method. [226] When tested in sodium cells within the 0.02-2.5 V (*vs* Na/Na^+) voltage range, FeS_2-NCs provided a capacity of 410 mAh g^{-1} for 600 cycles at 1 A g^{-1}. The reaction involved during cycling implies the formation of amorphous intermediated species, which are responsible of a reduced mechanical stress upon expansion and contraction. Recently, Liu *et al.* synthesized a unique FeS_2@C yolk-shell (FeS_2 core and carbon shell) nanostructured electrode using a facile etching method coupled with a novel sulfidation-in-nanobox strategy. The composites delivered a specific capacity of 511 mAh g^{-1} at 100 mA g^{-1} after 100 cycles and 330 mAh g^{-1} after 800 cycles at 2 A g^{-1}, showing excellent rate capability and ultra-long cycling stability. [227] To further address the structural stability and sulfur dissolution upon sodiation, composition tuning (ion doping) and carbon coating strategies have been proposed. It has been proved that the cobalt doping could enhance the redox activity of FeS_2 nanospheres by pseudo-capacitive behavior enabling fast Na storage. [228] Moreover, Chen *et al.* proposed the use of optimized binder for the improvement of cell performance. Using sodium polyacrylate (PAA) as binder and graphene coating, the electrode exhibited high specific capacity (524 mAh g^{-1}) and long cycle life (87.8% capacity retention after 800 cycles). [229]

FeS has also been investigated as anode for SIBs with a theoretical capacity of 609 mAh g^{-1}. The reaction mechanism proposed involves the formation of Na_xFeS_2 along with metallic Fe followed at about 0.1V (*vs* Na/Na^+) by the final reduction to Fe and formation of Na_2S. However, as for FeS_2, low conductivity, sluggish kinetics and severe volume changes have been demonstrated for FeS anodes. [230] Latest research provide results on the effect of downsizing the particle size and constructing 3D conductive networks to improve the electrochemical performance of FeS in SIBs. [219] As shown in

Figure 12 a, Wang *et al.* prepared a uniform FeS@C yolk-shell nanosphere (FeS yolks with an average size of ~170 nm, void spaces of ~20 nm and porous carbon shells with a thickness of ~30 nm) via a spatially confined sulfuration strategy using nano Fe_3O_4 as template. The electrode delivered a high reversible capacity of 722 mAh g^{-1} at 100 mA g^{-1} with a capacity retention of 67.6% after 300 cycles. The carbon coating acts as a stabilizer of the SEI film leading to the achievement of a relatively high initial coulombic efficiency (~70.2%). However, the unique yolk-shell structure was gradually damaged resulting from the large volume expansion experienced by FeS during the sodiation process leading to a gradual capacity fading, which was confirmed by TEM analysis as shown in **Figure 12 d**. [219] Lee *et al.* synthesized FeS/rGO composites via sulfidation of Fe_3O_4 by spray pyrolysis with H_2S gas. [231] The cycling stability and rate capability were in some extent improved by the large amount of graphene (37.4%). Meanwhile, Cho *et al.* fabricated porous FeS nanofibers via a simple sulfidation process driven by Kirkendall diffusion. [232] The discharge capacity reached during the first cycle at 500 mA g^{-1} was about 561 mAh g^{-1}, which then gradually increased to 592 mAh g^{-1} during the following cycles. Even at 5 A g^{-1}, a capacity of 353 mAh g^{-1} was maintained, confirming the superior rate performance.

Recently, several cobalt sulfides (Co_xS_y) with various nanostructures have been investigated as anode candidates for SIBs. [178, 234-236] CoS, known for its semiconducting properties, has a theoretical capacity of 589 mAh g^{-1}. Ramakrishna *et al.* firstly prepared CoS nanoplates on rGO via solvothermal method. [235] The hybrid composite exhibited a high capacity of 540 mAh g^{-1} at 1 A g^{-1} with extraordinarily cycling stability (420 mAh g^{-1} at 1 A g^{-1} after 1000 cycles). Moreover, Goodenough *et al.* demonstrated a low-cost hydrothermal method to synthesize CoS nanotubes coated with N-doped carbon, which were used as anodes in both LIBs and SIBs. [233] The synthesis process is shown

in **Figure 13 a**. A very high reversible capacity of 656 mAh g^{-1} was achieved at 500 mA g^{-1} while a satisfactory capacity of 396 mAh g^{-1} was still observed at 3 A g^{-1}, with a capacity retention of 55% after 1400 cycles (**Figure 13 b**). The good cycling stability of the electrode is most likely related to the implementation of coaxial nanotubes which enhanced the structural integrity of the electrode when compared with pristine CoS nanotubes. The unique electrode architecture designed, including the N-doped carbon shell and hollow CoS nanotube core, can effectively accommodate the large volume change of CoS and facilitate the charge transfer with high electrochemical reactivity, thus enhancing the overall electrochemical performance. [233] Carbon nanotubes were also employed as template to fabricate hollow structure of CoS/C nanocomposites. [237, 238] The use of CoS_2 as anode for SIBs was also reported with a theoretical capacity of 872 mAh g^{-1} via a reaction mechanism similar to that proposed for FeS_2. Indeed, the formation of Na_xCoS_2 as an intermediate phase above 1.0 V (*vs* Na/Na^+) is considered to be responsible for the reversible conversion reaction. [239] Additionally, also Co_3S_4 and Co_9S_8 have been synthesized and reported as anode for SIBs with theoretical capacities of about 702 and 544 mAh g^{-1}, respectively. However, due to the poor cycling performance in SIBs, rare breakthroughs are reported compared with LIBs. [240, 241] Thus, carbon coating is the general strategy adopted to cope with the poor performance. [242, 243] Other transition metal sulfides with higher abundance than Co analogues, such as CuS, [244] MnS, [245] Ni_2S_3, [246], have been investigated incorporating rGO to form composites and benefitting from the conductive nature of rGO and its effective buffering matrix effect. Xia *et al.* prepared thin Ni_3S_2 nanosheets anchored on cracked carbon submicron tubes via the hydrothermal method, showing high initial reversible capacity of 887 mAh g^{-1} at 50 mA g^{-1}, but with only 76% capacity retention after 260 cycles. [247] In view of the electrochemical performance shown by these materials, it is expected that further efforts and

research toward morphology tuning and electrode architecture design may lead to very promising results.

Owing to intrinsically good conductivity, which can facilitate the migration of Na^+ ions, layered transition-metal chalcogenides (*l*-TMC) such as MoS_2, WS_2, VS_2, have attracted great attention. MoS_2, well known for its semiconducting properties, presents a very interesting structure mainly composed by weakly bonded single layers of MoS_2. The van der Waals interactions between layers generate atypical interlayer distance of 0.62 nm. From this particular structure, one or several layers can be easily extracted using liquid-phase exfoliation. [248] Due to its high conductivity and chemical stability, nanostructured MoS_2 electrodes have been intensively studied as conversion-based anodes in LIBs showing very high theoretical capacities. [249] The favorable layered structure and interlayer distance of bulk MoS_2 also enable the insertion of Na ions, suggesting the applicability of this compound in SIBs. The first report on MoS_2 in SIBs was carried out by Part *et al.* [250], which was studied within the 0.4-2.6 V (*vs* Na/Na^+) voltage range, delivering a reversible capacity of about 160 mAh g^{-1} due to the intercalation of Na ions forming Na_xMoS_2 (above 0.4 V *vs* Na/Na^+, x<2). When discharged to a lower voltage (<0.4 V *vs* Na/Na^+), the sodiated Na_xMoS_2 could be fully transformed into metal Mo and Na_2S, contributing to a higher specific capacity. [251] However, the structural rearrangements and changes in the restacking sequence of the layers upon sodiation, combined with the volume expansion, accelerate the capacity fading upon cycling. Several strategies such as carbon incorporation and morphological design have been proposed to improve the reversible capacity and the cycling stability. One of the first reports on the effect of the incorporation of MoS_2 with graphene focused on the design of a binder-free, freestanding electrode. [252] Practically, a free-standing paper composed of few-layer MoS_2 nanosheets and rGO was fabricated by vacuum filtration, showing a

stable capacity of 230 mAh g^{-1}. [252] Maier *et al.* prepared single-layered MoS_2 nanoplates in carbon nanofibers via an electrospinning method combined with high-temperature pyrolysis treatment. [253] A high discharge capacity based on the conversion reaction was achieved, which however dropped to 57% of the initial value after 100 cycles. However, limiting the cycling up to 0.4V (*vs* Na/Na^+), thus avoiding the conversion reaction and exploiting only the intercalation, could greatly improve the electrochemical performance. Indeed, it has been reported that expanding the interlayer distance of a MoS_2-nanoflowers electrode enables a high capacity and superior stability due to the reduced Na^+ diffusion barrier and increased capacitive Na^+ storage. [254] When using the intercalation mechanism, in order to prevent the structural collapse and restacking, graphene was introduced into the interlayers of MoS_2 by Wang *et al.* [34] Computational and experimental results indicated that the MoS_2/rGO heterointerfaces could facilitate the Na^+ diffusion and provide more active sites for Na^+ storage, contributing to a high reversible capacity of 702 mAh g^{-1} with capacity retention of 61.3% after 100 cycles at 20 mA g^{-1}. To further improve the cycling stability, a strategy integrating the heterostructures with interlayer expansion has been used by Li *et al.*, who fabricated 2D MoS_2/polyaniline nanosheet heterostructures with large interlayer distance of 1.08 nm. [255] The hybrids exhibited a high sodium storage capacity of 734 mAh g^{-1} and a satisfactory cycle life (~93% capacity retention after 100 cycles), resulting from the remarkably improved Na^+ diffusion mobility in the interlayers and maintained structural stability. Moreover, Cheng *et al.* proposed MOFs-derived, N-doped carbon nanowall arrays as host for the growth of ultrathin MoS_2 (~4 nm) nanosheets with large interlayer spacing (~0.65 nm) prepared via hydrothermal method as shown in **Figure 14**. The obtained CC@CN@MoS_2 hybrids delivered high reversible capacities, 660 mAh g^{-1} and 306 mAh g^{-1} at

100 mA g^{-1} and 1.0 A g^{-1}, respectively. After 1000 cycles at 1.0 A g^{-1}, the capacity still remained satisfactory, showing excellent rate capacity and cycling life. [256]

With a similar layered structure, VS_2 and WS_2 have also been investigated as anode materials for SIBs. [257, 258] The Na storage includes the intercalation and conversion mechanisms. To improve the electrochemical performance of WS_2, the hierarchical WS_2 nanosheets/CNT-rGO aerogel nanostructure was designed by Yang *et al.* via a simple solvothermal method followed by freeze-drying and post annealing process. [259] This material delivered a capacity of 311.4 mAh g^{-1} at 100 mA g^{-1}, retaining a capacity of 252.9 mAh g^{-1} after 100 cycles at 200 mA g^{-1}. However, the rate capability was limited considering its high theoretical capacity (47.2 mAh g^{-1} at 10.0 A g^{-1}). The initial coulombic efficiency was about 33.9%, most likely attributable to the high reactivity the CNT-rGO carbon matrix with the electrolyte.

It has been proposed that embedding the active materials into ordered mesoporous carbon matrix could shorten the charge transfer, improve the electrical contact, mitigate the volume expansion and trap the polysulphides species formed upon cycling. [260] Chen *et al.* integrated ultrathin WS_2 nanosheets into CMK-3 matrix via hydrothermal method, and tested the developed electrode both in LIBs and SIBs. [261] In SIBs, the material delivered a capacity of 333 mAh g^{-1} at 100 mA g^{-1} without capacity fading after 70 cycles. At 2.0 A g^{-1}, a capacity of 230 mAh g^{-1} was maintained. It is worth noting that in this case the initial coulombic efficiency of about 60%, was greatly enhanced. On the other hand, metallic VS_2 is expected to have better structural stability during charging and discharging as anode for SIBs, which is crucial to obtain high-rate performance. Recently, Li *et al.* synthesized hierarchical VS_2 nanosheets via hydrothermal method followed by annealing treatment and suggested the developed material as a universal host for alkali metal ion (Li^+, Na^+, and K^+)

storage. [262] In SIBs, a remarkably high reversible capacity of 680 mAh g^{-1} was achieved at 100 mA g^{-1}, with an initial coulombic efficiency of 86%. Ramping the current to 1.0 A g^{-1}, a capacity of 550 mAh g^{-1} was achieved, which was retained after 200 cycles at 500 mAh g^{-1}, thus suggesting far better performance than MoS_2. Huang *et al.* reported the study of exfoliated V_5S_8 nanosheet-based electrodes combining both intercalation and conversion mechanisms. [263] As hybrid with graphite, the composites demonstrated high reversible discharge capacity (682 mAh g^{-1} at 0.1 A g^{-1}) and satisfactory cycle life (496 mA h g^{-1} at 1.0 A g^{-1} after 500 cycles) due to the unique three-dimensional monoclinic structure of V_5S_8, suggesting it as an interesting anode candidate for SIBs. Although these materials show promising properties for rechargeable alkali ion batteries, there are only a few reports to date, suggesting the possibility of new exiting findings and possible future applications.

It could generally be claimed that all the sulfides materials reported so far present interesting properties and performance, however, a deeper knowledge of the reaction mechanisms occurring may represent a key turning point for the real application of such materials. Indeed, NbS_2, which could be synthesized by solid-state sulfidation method, can reversibly store sodium ions only through an intercalation mechanism, strongly differing from its analogue VS_2. [264] The differences between analogues in the storage mechanism of sodium ions may suggest further need of understanding, which may lead to surprising findings in the near future.

Nanostructured transition metal selenides have also been studied as anodes for SIBs. [265] Most of the selenides can be synthesized by simple hydrothermal method. The first report on the use of transition metal selenides in SIBs was related to Cu_2Se, which could exhibit 171 mAh g^{-1} at 0.05 A g^{-1} with an average working potential of about 2.0 V (*vs* Na/Na^+), suggesting its application as cathode material. [266] Accordingly, $MoSe_2$, [267] $FeSe_2$, [268] CoSe, [269] $CoSe_2$, [270] Co_9Se_8, [271] WSe_2, [272] $NiSe_2$ [273]

and their nanostructures have been synthesized via solid-state selenization or hydrothermal/solvothermal methods, and applied as anodes for SIBs. Among them, cobalt selenides have attracted more attention due to their higher electrochemical activity. Chen *et al.* synthesized urchin-like $CoSe_2$ composed of nanorods via simple solvothermal method. [274] The as-prepared $CoSe_2$, cycled within the 0.5-3.0 V (*vs* Na/Na^+) voltage range, showed a high reversible capacity of 410 mAh g^{-1} after 1800 cycles at 1 A g^{-1} with a capacity retention of 98.6% and excellent high rate performance at 10 A g^{-1}, still delivering a capacity of 354 mAh g^{-1}. The outstanding electrochemical properties were attributed to the nanostructured design, allowing for a shorter Na^+ diffusion length, the high electrical conductivity of selenides, the use of an optimized ether-based electrolyte and the contribution of the pseudo-capacitive behavior to the redox reaction. Qiu *et al.* used cobalt-based MOFs (ZIF-67) as selenization precursors to fabricate hollow $CoSe_2$/C nanospheres bridged by CNTs. [275] The anode exhibited high reversible capacity (470 mAh g^{-1} at 0.2 A g^{-1}), good rate capability (373 mAh g^{-1} even at 10 A g^{-1}), and excellent cycling stability of over 1000 cycles (capacity retention of 100% after 70 cycles). Accordingly, Cao *et al.* synthesized a nitrogen-doped, yolk-shell CoSe/C mesoporous dodecahedra using ZIF-67 as template reaching specific capacities of about 597.2 and 361.9 mAh g^{-1} at 0.2 and 16 A g^{-1}, respectively. [276] When evaluated as novel anode materials for SIBs, selenides show much better electrochemical performance than their sulfides and oxides, however, it should also be considered that the sodium intercalation in selenides occurs at slightly higher potentials, affecting the final overall energy density of the cell when coupled with a cathode material. In addition, cost and toxicity represent two fundamental factors to be considered for selenides based electrodes.

5.3. Transition Metal Nitrides and Phosphides

Transition metal nitrides (TMNs) and phosphides (TMPs) have recently received attention as anodes for SIBs. They show Na-storage ability via the formation of transition metals embedded in sodium nitride/phosphide matrices. Theoretically, several transition metals, such as V, Co, Fe, Mn, Ni and Cu, nitrides and phosphides can react with sodium via conversion. Specifically, Cu_3N, [277] Fe_2N, [278] Mo_2N, [279] and VN [280] have been reported as anode materials for SIBs. However, the capacity fading and reversibility of the process still need to be clarified. For instance, vanadium nitride (VN) could deliver a very large reversible capacity of about 1200 mAh g^{-1}, much higher than other metal nitrides previously reported because of the high valence state of V. Song *et al.* prepared VN quantum dots on graphene nanosheets via a hydrothermal method followed by annealing treatment under ammonia gas. [280] The electrode delivered a specific capacity of 237 mAh g^{-1} when cycled at 74.4 mA g^{-1}, with better rate capability and cycling stability than pristine VN.

The exploration of phosphides for SIBs benefits from the achievements obtained on LIBs. Several transition metal phosphides (e.g. CuP_2, CoP, FeP_4, FeP_2, FeP, Zn_3P_2, Ni_2P) have been proved electrochemical active as anodes. [180, 281-286] Yan *et al.* reported the sodium storage properties of Cu_3P nanowires made via the in situ growth of $Cu(OH)_2$ templates and following phosphidation strategy by sodium hypophosphite. [287] The material demonstrated high reversible capacity (349 mAh g^{-1} at 50 mA g^{-1}), good rate capability and cycling stability (196 mAh g^{-1} at 1000 mA g^{-1} and capacity retention of 68% after 260 cycles, respectively). Among other TMPs, CoP represents a particularly promising compound due to its high theoretical capacity (about 894 mAh g^{-1}). Interestingly, strategies of integrating MOFs derivatives with *in situ* phosphidation process have been used to design CoP/C nanostructures.[179, 288, 289] For instance, Kang *et al.* fabricated CoP nanoparticles embedded in nitrogen-doped carbon nanosheets via a simple, one-step calcination of

Co-based MOFs and red P. [290] The composite delivered capacities of 831 mAh g^{-1} at 100 mA g^{-1}, and 174 mAh g^{-1} at 20 A g^{-1} with 98.5% capacity retention after 900 cycles at 1 A g^{-1}, thus showing excellent rate capability and long-term cyclability. Taking into account the limited studies on the electrochemical performance as well as on the reaction mechanisms, devoted deeper understanding is required to clarify the relation between performance and structure of these materials. However, it is important to point out that the current synthesis procedure of phosphides mostly employs sodium hypophosphite as a precursor, which may generate highly toxic PH_3 gas during phosphidation, and flammable red P as P sources. The cost and safety of the synthetic pathway to produce these materials still need to be improved thus facilitating their use for practical application.

Conclusively, several strategies have been proposed to improve the structural stability, electrode integrity upon cycling and consequent electrochemical activity of conversion-based electrode materials. One effective method relies on the design and synthesis of nanostructured electrode materials, which are all expected to promote the electrochemical performance. To maximize the advantages of nanostructured materials, the optimization of the morphology, composition, porosity, and surface characteristics play a fundamental role. Various nanostructures with beneficial properties were prepared via template-free approaches, among which hydrothermal method is a strong solution-phase method for structural design. Another approach is to integrate carbonaceous matrixes into the active materials to form hybrid nanostructures, which can better buffer the volume strain, due to the elastic feature of carbon supports, and increase the electrical conductivity. Additionally, direct carbonization of metal-organic-frameworks used as templates is a promising strategy to fabricate heterogeneous carbonaceous hybrids benefitting from the spectacular development of MOFs in the last years. Although the specific capacity and rate capability of the

conversion-based anodes can be improved by nanostructuration and electrode design optimization, still the formation of a stable SEI remains a quite challenging issue to be addressed for conversion-anodes (as for alloying anodes), which is further exacerbated in the case of nanostructured electrodes presenting enhanced reactivity toward the electrolytes.

6. Nanostructured Conversion-Alloying Materials

Recently an interesting group of oxides and sulfides based on group IV and V elements, herein named as conversion-alloying materials (CAMs), have received increasing attention as anode materials. These compounds offer the possibility to reach high specific capacities while lowering the average working potential of conversion anodes, generally occurring above 0.4 V (*vs* Na/Na^+). In addition, the Na_2O formed during the conversion reaction may act as buffering matrix for the subsequent alloying reaction, generally occurring at lower potentials. Moreover, these materials benefit from the enhanced conductivity of the electrode due to the formation of metallic nanoparticles upon the conversion reaction. [32] The most studied conversion-alloying materials are SnO_x, [291, 292] SnS_x, [293] Sb_2O_3 [294] and Sb_2S_3 [295]. However, despite the great advantages predicted for this class of compounds, still the common issues related to the separate conversion and alloying reactions need to be addressed. Nanostructured design and carbon coating have been widely reported to improve their electrochemical performance as listed in **Table 3**.

6.1. Conversion-alloying Materials

Tin oxides (SnO and SnO_2) have been considered as promising anodes for SIBs and recently attracted great interest due to their high theoretical capacity, environmental benignity and low cost. [296] Basically, SnO_x reacts with Na first via conversion reaction ($SnO_x + 2xNa^+ \rightarrow Sn + xNa_2O$) and then the

reduced Sn metal alloys with Na through alloying reaction ($4Sn + 15Na^+ \leftrightarrow Na_{15}Sn_4$), both contributing to the high specific capacity. The Na_2O matrix accommodates the volume expansion of Sn nanoparticles and alleviates the agglomeration during alloying reaction. Although tremendous efforts have been devoted to improve the electrochemical performance, such as the implementation of nanostructured electrodes and carbon coatings, still the reported specific capacity is much lower than the theoretical value, which may be due to the sluggish kinetics of the reaction with sodium. In addition, it should also be considered that Na_2O suffers, as many other oxides, of low electrical conductivity. To circumvent these issues, Chou *et al.* synthesized SnO_2 nanoparticles (5 nm) anchored onto a rGO framework, through hydrothermal method. [297] The resulting material delivered a reversible capacity of 330 mAh g^{-1} with satisfactory capacity retention of 81.3% over 150 cycles. It is worth noting that the use of FEC as electrolyte additive strongly improved the performance, indicating that kinetics could be improved by forming a highly conductive and stable SEI. Moreover, He *et al.* fabricated a sandwiched C@SnO_2@C hollow nanostructure with ultrasmall SnO_2 nanoparticles (2-5 nm) using NaCl as template and CVD technique for carbon coating. [298] The composite exhibited extremely high reversible capacity of 468 mAh g^{-1} at 50 mA g^{-1} and high-rate cycling stability with only 10% capacity loss after 3000 cycles at 4.6 A g^{-1}. The low initial coulombic efficiency, attributed to the formation of an unstable SEI layer and the degree of irreversibility related to the partial conversion of SnO_2 into Sn and Na_2O, represent the main challenge for these materials. In an attempt to overcome these issues, Sun *et al.* prepared amorphous SnO_2/graphene aerogel composites via hydrothermal method and compared its performance with that of crystalline SnO_2/graphene aerogel obtained after annealing. [299] It was found that the amorphous nanocomposites delivered a higher reversible capacity of 380.2 mAh g^{-1} after 100 cycles at 50 mA g^{-1}

than the crystalline one. The good performance could be attributed to the intrinsic isotropic nature and enhanced Na^+ diffusion coefficient in amorphous SnO_2. Aiming to fully achieve the expected theoretical capacity from the conversion reaction, Kim *et al.* synthesized amorphous SnO_2 nanoparticles (2-5 nm) on carbon nanotubes via hydrothermal method. [300] The SnO_2/CNTs anodes delivered a superior specific capacity of 630.4 mAh g^{-1} at 0.1 A g^{-1} and 324.1 mAh g^{-1} at 1.6 A g^{-1}, confirming the enhanced kinetics with Na in amorphous SnO_2 and offering a potential way to improve the capacity.

Recent reports on SnO suggested it as a promising anode due to the properties of its layered structure and improved reversibility. [301] However, SnO is thermodynamically less stable than SnO_2 and hence more difficult to be obtained. Chen *et al.* synthesized ultrathin SnO nanoflakes arrays (10 layers) on graphene foam via hydrothermal growth. [302] The material exhibited excellent Na ions storage capacity of 580 mAh g^{-1} at 0.1 A g^{-1} and high-rate cycling stability (75% capacity retention after 1000 cycles at 1 A g^{-1}). The fast kinetics and long durability were attributed to the enhanced pseudocapacitive contribution conferred by the 2D nature. Zhang *et al.* systematically investigated 2D SnO nanosheets with tunable number of atomic layers by controlling the hydrothermal reaction time. [303] The SnO-2L nanosheet anodes bearing two to six SnO monolayers, as shown in **Figure 15**, exhibited the best performance, with a reversible capacity of 848 mAh g^{-1} at 0.1 A g^{-1} and high capacity retention of 91.8% after 1000 cycles at 1 A g^{-1}. As the average number of atomic layers in the anode sheets increased, the performance degraded significantly. This study represents an interesting finding, suggesting a new pathway for materials design enabling high-performance. [302] More recently, a facile method to fabricate SnO microflowers using ultrafast ionic liquid-assisted microwave synthesis was reported, [304] which Sn-Na alloying mechanism was investigated via

combined *ex situ* XRD and XPS measurements. The initial alloy formed upon sodiation is then desodiated in two successive, but fully separated, steps not leading to the pristine SnO phase, suggesting a more complex reaction mechanism and a degree of irreversibility of the overall process.

Tin sulfides (SnS and SnS_2) exhibit higher theoretical capacities, better structural stability and greater reversibility as anodes in SIBs when compared to the analogous oxides. Similar to the oxides, SnS_x reacts with Na first *via* conversion reaction ($SnS_x + 2xNa^+ \leftrightarrow Sn + xNa_2S$) and then the reduced Sn metal alloys with Na through alloying reaction ($4Sn + 15Na^+ \leftrightarrow Na_{15}Sn_4$), with a combined reversible conversion and alloying electrochemical reaction mechanisms. [305] The layered structure of these materials enables also the feasibility of Na insertion/extraction. SnS_2, exhibiting a layered structure with interlayer distance of about 0.590 nm, shows very promising application as anode for SIBs with a theoretical capacity as high as 1137 mAh g^{-1}. The SnS_2/rGO hybrid structure, realized by Lee *et al. via* hydrothermal method, offered initial reversible capacity of 630 mAh g^{-1} at 0.2 A g^{-1} and very high stability (500 mAh g^{-1} after 400 cycles at 1 A g^{-1}). [306] Xiong *et al.* synthesized SnS_2 nanocrystals (2-4 nm) on amino-functionalized rGO with strong chemical bonding. The composite electrode maintained a capacity of 680 mAh g^{-1} after 100 cycles at 0.2 A g^{-1} and 480 mAh g^{-1} after 1000 cycles at 1 A g^{-1}, respectively. This unique electrode design and morphology could efficiently stabilize the structure and maintain the electrical contact upon cycling. [307] Moreover, a hybrid composed of few-layer SnS_2 nanosheets and rGO nanosheets obtained by liquid-phase exfoliation approach showed highly reversible Na storage (specific capacity of 843 mAh g^{-1} at 0.1 A g^{-1}) most likely enabled by the use of 2D nanostructures significantly shortening the ion diffusion length thus enhancing the electrochemical kinetics. In addition to SnS_2, SnS was also investigated as anode in SIBs. [308] Firstly, Cao *et al.* investigated a SnS/C nanocomposite synthesized by mechanical milling, which exhibited

high Na storage capacity (568 mAh g^{-1} at 20 mA g^{-1}). [309] An ex-situ XRD study performed on the developed electrode demonstrated that the overall electrochemical process evolves through the conversion and alloying mechanisms. Indeed, during the discharge process, the metallic Sn phase is detected followed by the appearance of crystalline $Na_{15}Sn_4$ alloy phase. The latter one disappears upon subsequent charge, suggesting the reversibility of the alloying reaction. Interestingly, even upon full charge, the initial SnS phase was not detected, indicating that Sn is converted back to an amorphous phase or to very small SnS nanoparticles not detectable through XRD analysis due to the small particle size. [309]

The SnS/C nanocomposite has been also investigated by Yu *et al.* via fabrication of a binder-free electrode by electrostatic spray deposition. [310] The obtained SnS nanorods with size of about 10-20 nm were assembled into a 3D porous structure delivering a reversible capacity of 310 mAh g^{-1} at 1.0 A g^{-1} with capacity retention of 80% after 300 cycles. This simple but versatile preparation procedure can be easily applied to other metal sulfides. Recently, Yun *et al.* reported a paper-type hybrid anode composed of SnS nanoparticles and acid-treated multiwalled carbon nanotubes. [311] Using 1 M solution of $NaPF_6$ in diethylene glycol dimethyl ether (DEGDME) as electrolyte, the electrode showed a high reversible capacity of ~1200 mAh g^{-1} and a high coulombic efficiency of ~90% in the first cycle. Even in a full cell configuration, the PNA//$Na_{1.5}VPO_{4.8}F_{0.7}$ battery showed a specific energy and power of ~256 Wh kg^{-1} and ~471 W kg^{-1}, respectively, with good cycling stability. Moreover, the conducted ex-situ XRD analysis revealed the reversibility of the process through the detection of SnS phase upon de-sodiation, despite the amorphous nature of the re-generated phase obtained at 2.7 V. [310] To improve the energy density of nanocomposites, Huang *et al.* synthesized SnS nanoparticles anchored on three-dimensional N-doped graphene (SnS/3DNG) via a simple electrostatic attraction

as displayed in **Figure 16 a**. [312] With only 8 wt.% carbon content, the composite had an unprecedented reversible capacity of 509.9 mAh g^{-1} after 1000 cycles at 2.0 A g^{-1}, corresponding to a capacity retention rate of 87.1%. The three-dimensional N-doped graphene could efficiently sustain the volume expansion of SnS during sodiation, as indicated in **Figure 16 b**. [312] Besides the overall good electrochemical performances exhibited, the work demonstrated a new strategy for the design of high performance nanocomposite electrodes for application in both LIBs and SIBs.

Antimony-based oxides (Sb_2O_3) and sulfides (Sb_2S_3) can also undergo combined conversion and alloying reaction, which in the case of Sb_2O_3 proceed according to the following reaction: Sb_2O_3 + $6Na^+ \leftrightarrow 2Sb + 3Na_2O$ (conversion) and $2Sb + 6\ Na^+ \leftrightarrow 2Na_3Sb$ (alloying). Hu *et al.* demonstrated that pristine Sb_2O_3 thin film could deliver a high specific charge capacity of 509 mAh g^{-1} at 0.05 A g^{-1} and retained a capacity as high as 265 mAh g^{-1} when cycled at a high current density of 5 A g^{-1}. [294] As for SnS, no crystalline peaks of Sb_2O_3 were observed after full recharge in the XRD study, suggesting the material's amorphization. [294] To further enhance the electrical conductivity, Pan *et al.* synthesized the Sb_2O_3/rGO composite *via* microwave-assisted approach. A capacity of 503 mAh g^{-1} at 0.1 A g^{-1} after 50 cycles was achieved, slightly improving the rate performance of non-composite Sb_2O_3 electrodes. [35] As the analogue of Sb_2O_3, Sb_2S_3 has also attracted significant attention as anode for SIBs, due to its ability to store 12 moles of Na per mole of Sb_2O_3 thus possessing a very high theoretical specific capacity of about 946 mAh g^{-1}. To unfold the reaction mechanism in sodium cells, Kim *et al.* [313] synthesized one dimensional Sb_2S_3/C nanorods via hydrothermal method followed by a calcination step providing carbon coating. The electrode exhibited reversible capacities of 415 and 337 mAh g^{-1} at 1.0 and 2.0 A g^{-1}, respectively. *In situ* TEM results combined with first-principles calculations revealed that the Na ions intercalated into the layered Sb_2S_3 crystal during the first

sodiation process form an intermediate phase, *i.e.* $Na_xSb_2S_3$ with an ultrafast speed of 146 nm s^{-1}. The latter phase, upon de-sodiation, reversibly converted into an amorphous de-sodiated Sb_2S_3 phase with a very small volume expansion of ~54%, suggesting Sb_2S_3 as a very promising anode material for SIBs. [313]

Tin phosphide has also been recently investigated as anode material for SIBs. The reaction mechanism involves the initial formation of Na_3P through conversion, and the following generation of the $Na_{15}Sn_4$ phase *via* alloying. Sn_4P_3 possesses a high theoretical volumetric capacity of 6650 mAh cm^{-3} (gravimetric capacity of 1132 mAh g^{-1}) and good electrical conductivity of 30.7 S cm^{-1}. Lee *et al.* prepared Sn_4P_3 via the facile high-energy mechanical ball milling achieving a high reversible capacity of 718 mAh g^{-1} with negligible capacity fading over 100 cycles. [314] Unlike tin oxides electrodes, the crystalline Sn_4P_3 phase was gradually re-formed upon desodiation, indicating a certain reversibility of the conversion-alloying reaction through formation of Na_xP and $Na_{15}Sn_4$. Additionally, it is worth noting that the redox potential of Sn_4P_3 is lower than that of phosphorus/carbon composites, enabling high energy densities in full cell configuration. [314] The carbon coating process was also adopted during the mechanical synthesis obtaining a Sn_4P_3/C nanocomposite exhibiting very high reversible capacity (850 mAh g^{-1} at 50 mA g^{-1}). Moreover, Yin *et al.* synthesized the Sn_4P_3 nanoparticles with an average size of 6 nm on rGO nanosheets via hydrothermal reaction. [315] The obtained 3D mesoporous nanostructure, despite the initial low coulombic efficiency of about 46%, showed improved electrochemical performance with a reversible capacity of 391 mAh g^{-1} at 2.0 A g^{-1} and limited capacity fading. The poor coulumbic efficiency is most likely attributable to the high loading of graphene, which is generally responsible for Na ions consumption during the initial formation of the SEI layer. Recently, Wang *et al.* synthesized uniform pomegranate-like Sn_4P_3@C

spheres by aerosol spray-pyrolysis phosphidation method. [316] By using a stable ether-based electrolyte ($NaPF_6$-glyme), a reversible capacity of 800 mAh g^{-1} at 0.1 A g^{-1} was achieved with an extremely low capacity decay rate (0.09% per cycle). A significantly high first cycle coulombic efficiency (90.7%) was observed for Sn_4P_3@C in $NaPF_6$-glyme electrolyte, representing so far the highest coulombic efficiency in all Sn and P compounds reported to date. [316] Besides, core-shell nanostructures have been designed to sustain the volume expansion of Sn_4P_3 anodes during sodiation. Yu *et al.* prepared yolk-shell Sn_4P_3@C nanospheres by a top-down phosphidation route. The materials as anodes exhibited a high reversible capacity of 790 mAh g^{-1} at 0.1 A g^{-1} and superior rate capability of 505 mAh g^{-1} at 3.0 A g^{-1}, however, with poor initial coulombic efficiency (43.8%) and relatively low capacity retention (71.3% after 400 cycles). [317] In an attempt to improve the cell performance through morphology optimization, Shen *et al.* designed Sn_4P_3@C yolk-shell nanocubes with a high capacity of 508 mAh g^{-1} at 2.0 A g^{-1}. The nanocubes presented slightly improved first cycle coulombic efficiency (63.7%) and cycling stability (72.4% after 500 cycles at 2.0 A g^{-1}), however, still requiring further improvement. [318] Such results call for further efforts to extend the long-term cycling stability of these materials, enabling the maximization of the achievable capacity and cycling stability for the development of the future generation anode materials for SIBs.

6.2. Hybrid Strategies: Alloy/Conversion Heterostructures

Carbon materials are suitable candidates for the obtainment of composite heterostructures due to their good conductivity and mechanical properties. Carbon coatings and/or carbon-based additives represent a simple and economic strategy to improve the cycling stability of conversion and alloying materials, however, their additional weight inevitably leads to a reduction of the energy density of the cell, as they are generally inactive with Na uptake. Recently, an interesting strategy was

proposed to avoid this issue, consisting in designing nanostructured heterostructures employing combination of active materials, e.g., introducing an additional active material possessing improved structural stability, as a coating layer. [319] Layered transition metal dichalcogenides (such as MoS_2), oxides and sulfides based on group IV and V elements (such as SnS_2) and transition metal chalcogenides or phosphites (such as TiO_2, Ni-P) have been employed to fabricate heterostructured nanostructures with alloying and conversion anode materials as superior electrodes for SIBs. Some promising results have been summarized and listed in **Table 4**. For instance, Yang *et al.* fabricated double-walled Sb@TiO_{2-x} nanotubes exhibiting very low capacity fading and good rate performance (300 mAh g^{-1} after 1000 cycles at 2.64 A g^{-1}). The result clearly confirms the role of TiO_2 in the stabilization of the sodium storage process in Sb, due to its small volume change upon cycling and superior stability. [321] Also, the beneficial effect of heterostructures may result from the interfacial properties of the coating layer. It has been reported that ultrafast charge transfer could be achieved in MoS_2/WS_2 heterostructures due to the enhanced surface reaction kinetics and charge transport at the heterointerfaces. [322] In an attempt to prevent the typical capacity decay observed in WS_x system, attributable to sulfur dissolution, Taylor *et al.* reported the synthesis of heterogeneous tungsten sulfide/oxide core-shell nanofibers obtained via electrospinning. The following, facile post-treatment in air, was responsible for the formation of the external oxide layer (**Figure 17)**. The electrode exhibited a high reversible capacity of 791 mAh g^{-1} and improved cycle performance over 100 cycles. The results indicate that the designed hierarchical structure is effectively reducing the sulfur dissolution generally affecting WS_x systems upon formation of a WS_x/WO_3 hybrid. [320] Moreover, Guo *et al*. constructed a SnS/SnO_2 heterostructure with carbon coating which delivered a reversible capacity of 729 mAh g^{-1} at 30 mA g^{-1} and 409 mAh g^{-1} after 500 cycles at 810 mA g^{-1} (ca. 73%

retention), showing a remarkable high-rate capability and ultra-long cycle life. [323] Therefore, a promising solution to enable efficient sodium storage of alloying/conversion anode mateirals for SIBs consists in the implementation of 2D heterostructures, assembled by stacking different conventional 2D mateirals (i.e., graphene, transition metal oxides, carbides, nitrides or chalcogenides), in hetero-layered architectures. Among them, MoS_2 in a typical 2D van der Waals layered structure appears to be an ideal candidate providing different 2D heterostructures with improved ion transfer kinetics, for electrochemical energy storage. Shen et al. proposed a highly porous hierarchical $MoS_2/Ni_3S_2@MoS_2$ structure with homogeneous atomic heterointerfaces, which exhibited superior electrochemical performance. As anode in SIBs, it exhibited a very high reversible capacity of 568 mAh g^{-1} at a current density of 200 mAg^{-1} with excellent high-rate stability (~73% capacity retention of 207 mAh g^{-1} after 400 cycles at 5A g^{-1}). [326] These results suggest the design of hybrid heterostructures as a potentially viable strategy for the obtainment of high-performance anode materials.

7. Conclusion and Remarks

The recent research progresses toward the development of nanostructured alloying and conversion anodes for application in SIBs was extensively reviewed herein (as shown in **Figure 18**). Advantages of high theoretical capacity and tunable operating potential, especially when using combined conversion-alloying-type anodes make them very promising alternatives to intercalation-type electrodes and carbon-based anodes. Despite the great advantages offered by anode material employing "beyond-insertion" sodium storage mechanism, still several issues need to be addressed in terms of cycling stability and durability of the cell combined with the poor electrochemical kinetics of Na in such systems. However, proper nanostructuration and architecture of the electrodes appear

to be viable approaches to efficiently improve the electrochemical performance, including the reversible capacity, rate capability and long-term stability. The main approaches employed to improve the electrochemical behavior of these systems so far can be divided into two strategies: *i)* nanosizing of the active materials particles to shorten the Na diffusion and buffer the volume changes caused by the sodiation process and *ii)* hybridization with robust templates to suppress active material aggregation and improve conductivity. In this context, various synthesis strategies have been developed and optimized for the rational design of outperforming materials. An efficient and clever use of nanotechnology combined with targeted morphological modification represent valid approaches to improve the reversible capacity, enhance the rate capability and cycling stability, which represent crucial parameters for the evaluation of the most promising anode materials and their future possible implementation in viably marketable SIBs. Among all the strategies, carbon inclusion is an efficient way to obtain nanocomposites due to the high conductivity and considerable variability of the obtainable morphologies.

Although great progresses on the performance improvement at lab-scale have been obtained, still some main challenges need to be faced. Indeed, nanostructuration of materials cannot be considered the only solution for all the issues characterizing “beyond-insertion” anode materials. One of the greatest disadvantages of nanostructured electrodes is represented by their low density, which inevitably affects the volumetric energy density of the battery. Thus, developing high volumetric energy density materials is certainly a challenging objective. However, considering that the main application field for SIBs is stationary energy storage, the limited volumetric energy density may not represent a too serious issue if the final system is characterized by satisfactory gravimetric energy density and, most important, high energy efficiency and long-term cycling performance.

Another main challenge remains the obtainment of systems characterized by stable interfaces. Indeed, nanostructured anode materials generally present a relatively low initial coulombic efficiency related to the high surface area and vigorous reactivity of nanoparticles with electrolyte solution. In addition, the rather unstable SEI layer formed during the first cycle induces a continuous consumption and trapping of sodium upon cycling with consequent capacity fading at increasing number of cycles. The instability of the SEI is exacerbated by the continuous volume changes of alloying- and conversion-type materials upon cycling, leading to the continuous regeneration of the SEI layer and the consequent electrolyte decomposition. In this context, the development of optimized electrolytes may play a key role in the stabilization of the electrode/electrolyte interphase through the formation of a stable SEI and the improvement of the overall coulombic efficiency. Thus, new electrolytes to stabilize the SEI formation and suppress the decomposition on the active surface should be developed to improve the longevity of sodium anodes.

Up to date, hard carbons represent the most promising negative electrode materials for SIBs because of their relatively high storage capacity and satisfactory cycling stability. [24, 25, 332] Most of the reported materials exhibit specific capacities around 300-350 mAh g^{-1}, with differences attributable to morphologies and structures related to the different precursors used in the synthesis step. Interestingly, the possibility of producing high-performance hard carbon anode materials from biomass or bio-waste enables the achievement of high specific energy while ensuring sustainability and environmental friendliness. [333] Nevertheless, despite the promising properties, still some issues affect the overall performance of hard carbons, such as the high surface area, resulting in rather high first cycle irreversible capacities attributed to the SEI formation and the low density resulting in loe energy density. [334] Additionally, for the future implementation of hard carbons in commercial SIBs

for large-scale energy storage application, a low-cost and abundant carbon precursor is still necessary. [335] Further research in this direction is necessary to obtain high performance and low cost anode materials. However, alongside with the development of anode materials, design and production of high-performance cathode materials are also needed for a successful combination in high-performance SIBs. As most of the cathodes possess lower operating potentials in SIBs respect to LIBs, new materials exploitation with higher operating voltage is critical to improve the energy density of SIBs. Although layered transition metal oxide cathodes show higher capacity, polyanionic compounds could be a promising class due to the high voltage and cycling stability. Considering that the sodium-ion technology is at an early stage when compared to the lithium ion system, great successes have been already achieved in the development of high performance electrode materials. We believe that future progresses toward the enhancement of the performances, in view of their future implementation in real and marketable cell prototypes, should be mainly focused on the optimization of the electrolyte components and its interaction with the anode and cathode materials. The stabilization of the interphases and interfaces, which governs the kinetic of sodium-ion batteries, may represent a key turning point for the success of the sodium-ion technology.

Acknowledgements

H.Z. gratefully acknowledges the financial support of Chinese Scholarship Council. I.H. acknowledges the Assistant Secretary for Energy Efficiency and Renewable Energy, Office of Vehicle Technologies of the U.S. Department of Energy under Contract No. DE-AC02-05CH11231, under the Applied Battery Research for Transportation (ABR) Program and Award Number DE-EE0006443. H.Z. and S.P. also acknowledge the financial support of Helmholtz Association.

Received: ((will be filled in by the editorial staff))
Revised: ((will be filled in by the editorial staff))
Published online: ((will be filled in by the editorial staff))

References

[1] M. Hightower, S. A. Pierce, *Nature* **200**8, *452*, 285.

[2] B. Dunn, H. Kamath, J.-M. Tarascon, *Science* **2011**, *334*, 928.

[3] M. Armand, J. M. Tarascon, *Nature* **2008**, *451*, 652.

[4] B. Scrosati, J. Garche, *J. Power Sources* **2010**, *195*, 2419.

[5] J. B. Goodenough, K.-S. Park, *J. Am. Chem. Soc.* **2013**, *135*, 1167.

[6] Lithium supply and demand, https://www.dakotaminerals.com.au/lithium/lithium-supply-demand, accessed: August, 2017.

[7] T. G. Goonan, **2012**, Lithium use in batteries: U.S. Geological Survey Circular 1371, 14 p., available at http://pubs.usgs.gov/circ/1371/.

[8] The trouble with lithium, http://www.meridian-int-res.com/Projects/EVRsrch.htm, accessed: August, 2017.

[9] L. Gaines, P. Nelson, "Lithium-ion batteries: examining material demand and recycling issues", presented at 2010 TMS Annual Meeting and Exhibition, Seattle Washington, February 14-18, 2010.

[10] M. S. Whittingham, *Science* **1976**, *192*, 1126.

[11] C. Delmas, J.-J. Braconnier, C. Fouassier, P. Hagenmuller, *Solid State Ionics* **1981**, *3*, 165.

[12] V. Palomares, P. Serras, I. Villaluenga, K. B. Hueso, J. Carretero-Gonzalez, T. Rojo, *Energy Environ. Sci.* **2012**, *5*, 5884.

[13] M. D. Slater, D. Kim, E. Lee, C. S. Johnson, *Adv. Funct. Mater.* **2013**, *23*, 947.

[14] D. Kundu, E. Talaie, V. Duffort, L. F. Nazar, *Angew. Chem., Int. Ed.* **2015**, *54*, 3431.

[15] K. Kubota, S. Komaba, *J. Electrochem. Soc.* **2015**, *162*, A2538.

[16] S. Y. Hong, Y. Kim, Y. Park, A. Choi, N.-S. Choi, K. T. Lee, *Energy Environ. Sci.* **2013**, *6*, 2067.

[17] Sodium-ion technology, http://www.faradion.co.uk/technology/sodium-ion-technology/, accessed: August, 2017.

[18] I. Hasa, D. Buchholz, S. Passerini, B. Scrosati, J. Hassoun, *Adv. Energy Mater.* **2014**, *4*, 1400083.

[19] H. Zhang, I. Hasa, B. Qin, T. Diemant, D. Buchholz, R. J. Behm, S. Passerini, *ChemElectroChem* **2017**, *4*, 1256.

[20] K. Kubota, N. Yabuuchi, H. Yoshida, M. Dahbi, S. Komaba, *MRS Bull.* **2014**, *39*, 416.

[21] Q. Ni, Y. Bai, F. Wu, C. Wu, *Adv. Sci.* **2017**, *4*, 1600275.

[22] H. Pan, Y.-S. Hu, L. Chen, *Energy Environ. Sci.* **2013**, *6*, 2338.

[23] D. A. Stevens, J. R. Dahn, *J. Electrochem. Soc.* **2000**, *147*, 1271.

[24] C. Bommier, X. Ji, *Isr. J. Chem.* **2015**, *55*, 486.

[25] X. Dou, I. Hasa, M. Hekmatfar, T. Diemant, R. J. Behm, D. Buchholz, S. Passerini, *ChemSusChem* **2017**, *10*, 2668.

[26] A. Ponrouch, A. R. Goñi, M. R. Palacín, *Electrochem. Commun.* **2013**, *27*, 85.

[27] J. B. Goodenough, Y. Kim, *Chem. Mater.* **2010**, *22*, 587.

[28] M. Gauthier, T. J. Carney, A. Grimaud, L. Giordano, N. Pour, H.-H. Chang, D. P. Fenning, S. F. Lux, O. Paschos, C. Bauer, F. Maglia, S. Lupart, P. Lamp, Y. Shao-Horn, *J. Phys. Chem. Lett.* **2015**, *6*, 4653.

[29] C. Liu, Z. G. Neale, G. Cao, *Mater. Today* **2016**, *19*, 109.

[30] R. Mogensen, D. Brandell, R. Younesi, *ACS Energy Lett.* **2016**, *1*, 1173.

[31] B. L. Ellis, L. F. Nazar, *Curr. Opin. Solid State Mater. Sci.* **2012**, *16*, 168.

[32] D. Bresser, S. Passerini, B. Scrosati, *Energy Environ. Sci.* **2016**, *9*, 3348.

[33] Y. Liu, N. Zhang, L. Jiao, J. Chen, *Adv. Mater.* **2015**, *27*, 6702.

[34] X. Xie, Z. Ao, D. Su, J. Zhang, G. Wang, *Adv. Funct. Mater.* **2015**, *25*, 1393.

[35] D. Li, D. Yan, J. Ma, W. Qin, X. Zhang, T. Lu, L. Pan, *Ceram. Int.* **2016**, *42*, 15634.

[36] E. de la Llave, V. Borgel, K.-J. Park, J.-Y. Hwang, Y.-K. Sun, P. Hartmann, F.-F. Chesneau, D. Aurbach, *ACS Appl. Mater. Interfaces* **2016**, *8*, 1867.

[37] I. Hasa, X. Dou, D. Buchholz, Y. Shao-Horn, J. Hassoun, S. Passerini, B. Scrosati, *J. Power Sources* **2016**, *310*, 26.

[38] I. Hasa, S. Passerini, J. Hassoun, *RSC Adv.* **2015**, *5*, 48928.

[39] G. Singh, B. Acebedo, M. C. Cabanas, D. Shanmukaraj, M. Armand, T. Rojo, *Electrochem. Commun.* **2013**, *37*, 61.

[40] D. Shanmukaraj, S. Grugeon, S. Laruelle, G. Douglade, J.-M. Tarascon, M. Armand, *Electrochem. Commun.* **2010**, *12*, 1344.

[41] S. Komaba, T. Ishikawa, N. Yabuuchi, W. Murata, A. Ito, Y. Ohsawa, *ACS Appl. Mater. Interfaces* **2011**, *3*, 4165.

[42] J. W. Choi, D. Aurbach, *Nat. Rev. Mater.* **2016**, *1*, 16013.

[43] Y. Kim, K.-H. Ha, S. M. Oh, K. T. Lee, *Chem. Eur. J.* **2014**, *20*, 11980.

[44] A. S. Arico, P. Bruce, B. Scrosati, J.-M. Tarascon, W. van Schalkwijk, *Nat. Mater.* **2005**, *4*, 366.

[45] P. S. Herle, B. Ellis, N. Coombs, L. F. Nazar, *Nat. Mater.* **2004**, *3*, 147.

[46] H. Huang, S.-C. Yin, L. F. Nazar, *Electrochem. Solid-State Lett.* **2001**, *4*, A170.

[47] P. Gibot, M. Casas-Cabanas, L. Laffont, S. Levasseur, P. Carlach, S. Hamelet, J.-M. Tarascon, C. Masquelier, *Nat. Mater.* **2008**, *7*, 741.

[48] A. K. Padhi, K. S. Nanjundaswamy, J. B. Goodenough, *J. Electrochem. Soc.* **1997**, *144*, 1188.

[50] D. Larcher, C. Masquelier, D. Bonnin, Y. Chabre, V. Masson, J.-B. Leriche, J.-M. Tarascon, *J. Electrochem. Soc.* **2003**, *150*, A133.

[51] M. He, K. Kravchyk, M. Walter, M. V. Kovalenko, *Nano Lett.* **2014**, *14*, 1255.

[52] A. Manthiram, A. Vadivel Murugan, A. Sarkar, T. Muraliganth, *Energy Environ. Sci.* **2008**, *1*, 621.

[53] P. G. Bruce, B. Scrosati, J.-M. Tarascon, *Angew. Chem., Int. Ed.* **2008**, *47*, 2930.

[54] Y. Xu, Y. Zhu, Y. Liu, C. Wang, *Adv. Energy Mater.* **2013**, *3*, 128.

[55] V. L. Chevrier, G. Ceder, *J. Electrochem. Soc.* **2011**, *158*, A1011.

[56] L. D. Ellis, T. D. Hatchard, M. N. Obrovac, *J. Electrochem. Soc.* **2012**, *159*, A1801.

[57] J. W. Wang, X. H. Liu, S. X. Mao, J. Y. Huang, *Nano Lett.* **2012**, *12*, 5897.

[58] S. Komaba, Y. Matsuura, T. Ishikawa, N. Yabuuchi, W. Murata, S. Kuze, *Electrochem. Commun.* **2012**, *21*, 65.

[59] L. Baggetto, P. Ganesh, R. P. Meisner, R. R. Unocic, J.-C. Jumas, C. A. Bridges, G. M. Veith, *J. Power Sources* **2013**, *234*, 48.

[60] L. Baggetto, J.-C. Jumas, J. Gorka, C. A. Bridges, G. M. Veith, *Phys. Chem. Chem. Phys.* **2013**, *15*, 10885.

[61] P. R. Abel, M. G. Fields, A. Heller, C. B. Mullins, *ACS Appl. Mater. Interfaces* **2014**, *6*, 15860.

[62] B. Farbod, K. Cui, W. P. Kalisvaart, M. Kupsta, B. Zahiri, A. Kohandehghan, E. M. Lotfabad, Z. Li, E. J. Luber, D. Mitlin, *ACS Nano* **2014**, *8*, 4415.

[63] H. Xie, W. P. Kalisvaart, B. C. Olsen, E. J. Luber, D. Mitlin, J. M. Buriak, *J. Mater. Chem. A* **2017**, *5*, 9661.

[64] T. Křenek, P. Bezdička, N. Murafa, J. Šubrt, J. Pola, *Eur. J. Inorg. Chem.* **2009**, *2009*, 1464.

[65] B. Reddy, P. Bhattacharya, B. Singh, K. Chattopadhyay, *J. Mater. Sci.* **2009**, *44*, 2257.

[66] S. Fan, L. Y. Lim, Y. Y. Tay, S. S. Pramana, X. Rui, M. K. Samani, Q. Yan, B. K. Tay, M. F. Toney, H. H. Hng, *J. Mater. Chem. A* **2013**, *1*, 14577.

[67] Y. Wang, J. Y. Lee, *Angew. Chem., Int. Ed.* **2006**, *45*, 7039.

[68] L. Xiao, Y. Cao, J. Xiao, W. Wang, L. Kovarik, Z. Nie, J. Liu, *Chem. Commun.* **2012**, *48*, 3321.

[69] A. Darwiche, M. T. Sougrati, B. Fraisse, L. Stievano, L. Monconduit, *Electrochem. Commun.* **2013**, *32*, 18.

[70] L. Li, K. H. Seng, D. Li, Y. Xia, H. K. Liu, Z. Guo, *Nano Res.* **2014**, *7*, 1466.

[71] L. Ji, M. Gu, Y. Shao, X. Li, M. H. Engelhard, B. W. Arey, W. Wang, Z. Nie, J. Xiao, C. Wang, J.-G. Zhang, J. Liu, *Adv. Mater.* **2014**, *26*, 2901.

[72] Y. Jeon, X. Han, K. Fu, J. Dai, J. H. Kim, L. Hu, T. Song, U. Paik, *J. Mater. Chem. A* **2016**, *4*, 18306.

[73] B. Luo, T. Qiu, D. Ye, L. Wang, L. Zhi, *Nano Energy* **2016**, *22*, 232.

[74] Y. Liu, Y. Xu, Y. Zhu, J. N. Culver, C. A. Lundgren, K. Xu, C. Wang, *ACS Nano* **2013**, *7*, 3627.

[75] X. Xie, K. Kretschmer, J. Zhang, B. Sun, D. Su, G. Wang, *Nano Energy* **2015**, *13*, 208.

[76] M. Sha, H. Zhang, Y. Nie, K. Nie, X. Lv, N. Sun, X. Xie, Y. Ma, X. Sun, *J. Mater. Chem. A* **2017**, *5*, 6277.

[77] S. Li, Z. Wang, J. Liu, L. Yang, Y. Guo, L. Cheng, M. Lei, W. Wang, *ACS Appl. Mater. Interfaces* **2016**, *8*, 19438.

[78] Y. Liu, N. Zhang, L. Jiao, Z. Tao, J. Chen, *Adv. Funct. Mater.* **2015**, *25*, 214.

[79] H. Zhu, Z. Jia, Y. Chen, N. Weadock, J. Wan, O. Vaaland, X. Han, T. Li, L. Hu, *Nano Lett.* **2013**, *13*, 3093.

[80] K. Dai, H. Zhao, Z. Wang, X. Song, V. Battaglia, G. Liu, *J. Power Sources* **201**4, *263*, 276.

[81] J. Qian, Y. Chen, L. Wu, Y. Cao, X. Ai, H. Yang, *Chem. Commun.* **2012**, *48*, 7070.

[82] A. Darwiche, C. Marino, M. T. Sougrati, B. Fraisse, L. Stievano, L. Monconduit, *J. Am. Chem. Soc.* **2012**, *134*, 20805.

[83] L. Baggetto, H.-Y. Hah, J.-C. Jumas, C. E. Johnson, J. A. Johnson, J. K. Keum, C. A. Bridges, G. M. Veith, *J. Power Sources* **2014**, *267*, 329.

[84] P. K. Allan, J. M. Griffin, A. Darwiche, O. J. Borkiewicz, K. M. Wiaderek, K. W. Chapman, A. J. Morris, P. J. Chupas, L. Monconduit, C. P. Grey, *J. Am. Chem. Soc.* **2016**, *138*, 2352.

[85] H. Che, S. Chen, Y. Xie, H. Wang, K. Amine, X.-Z. Liao, Z.-F. Ma, *Energy Environ. Sci.* **2017**, *10*, 1075.

[86] L. Baggetto, E. Allcorn, A. Manthiram, G. M. Veith, *Electrochem. Commun.* **2013**, *27*, 168.

[87] L. Baggetto, E. Allcorn, R. R. Unocic, A. Manthiram, G. M. Veith, *J. Mater. Chem. A* **2013**, *1*, 11163.

[88] J. Liu, Z. Yang, J. Wang, L. Gu, J. Maier, Y. Yu, *Nano Energy* **2015**, *16*, 389.

[89] A. Nie, L.-y. Gan, Y. Cheng, X. Tao, Y. Yuan, S. Sharifi-Asl, K. He, H. Asayesh-Ardakani, V. Vasiraju, J. Lu, F. Mashayek, R. Klie, S. Vaddiraju, U. Schwingenschlögl, R. Shahbazian-Yassar, *Adv. Funct. Mater.* **2016**, *26*, 543.

[90] X. Zhou, Z. Dai, J. Bao, Y.-G. Guo, *J. Mater. Chem. A* **2013**, *1*, 13727.

[91] X. Zhao, S. A. Vail, Y. Lu, J. Song, W. Pan, D. R. Evans, J.-J. Lee, *ACS Appl. Mater. Interfaces* **2016**, *8*, 13871.

[92] Y. N. Ko, Y. C. Kang, *Chem. Commun.* **2014**, *50*, 12322.

[93] N. Zhang, Y. Liu, Y. Lu, X. Han, F. Cheng, J. Chen, *Nano Res.* **2015**, *8*, 3384.

[94] Z. Liu, X.-Y. Yu, X. W. Lou, U. Paik, *Energy Environ. Sci.* **2016**, *9*, 2314.

[95] X. Liu, Y. Du, X. Xu, X. Zhou, Z. Dai, J. Bao, *J. Phys. Chem. C* **2016**, *120*, 3214.

[96] T. Wu, H. Hou, C. Zhang, P. Ge, Z. Huang, M. Jing, X. Qiu, X. Ji, *ACS Appl. Mater. Interfaces* **2017**, *9*, 26118.

[97] K. Li, D. Su, H. Liu, G. Wang, *Electrochim. Acta* **2015**, *177*, 304.

[98] H.-Y. Lü, F. Wan, L.-H. Jiang, G. Wang, X.-L. Wu, *Part. Part. Syst. Charact.* **2016**, *33*, 204.

[99] F. Wan, H.-Y. Lü, X.-H. Zhang, D.-H. Liu, J.-P. Zhang, X. He, X.-L. Wu, *J. Alloys Compd.* **2016**, *672*, 72.

[100] C. Nithya, S. Gopukumar, *J. Mater. Chem. A* **2014**, *2*, 10516.

[101] L. Hu, X. Zhu, Y. Du, Y. Li, X. Zhou, J. Bao, *Chem. Mater.* **2015**, *27*, 8138.

[102] W. Zhang, Y. Liu, C. Chen, Z. Li, Y. Huang, X. Hu, *Small* **2015**, *11*, 3822.

[103] A. Pfitzner, *Angew. Chem., Int. Ed.* **2006**, *45*, 699.

[104] J. M. Sangster, *J. Phase Equilib. Diffus.* **2010**, *31*, 62.

[105] P. Extance, S. R. Elliott, *Philos. Mag. B* **1981**, *43*, 469.

[106] N. Yabuuchi, Y. Matsuura, T. Ishikawa, S. Kuze, J.-Y. Son, Y.-T. Cui, H. Oji, S. Komaba, *ChemElectroChem* **2014**, *1*, 580.

[107] J. Zhou, X. Liu, W. Cai, Y. Zhu, J. Liang, K. Zhang, Y. Lan, Z. Jiang, G. Wang, Y. Qian, *Adv. Mater.* **2017**, *29*, 1700214.

[108] J. Qian, X. Wu, Y. Cao, X. Ai, H. Yang, *Angew. Chem.* **2013**, *125*, 4731.

[109] Y. Kim, Y. Park, A. Choi, N.-S. Choi, J. Kim, J. Lee, J. H. Ryu, S. M. Oh, K. T. Lee, *Adv. Mater.* **2013**, *25*, 3045.

[110] W.-J. Li, S.-L. Chou, J.-Z. Wang, H.-K. Liu, S.-X. Dou, *Nano Lett.* **2013**, *13*, 5480.

[111] J. Song, Z. Yu, M. L. Gordin, S. Hu, R. Yi, D. Tang, T. Walter, M. Regula, D. Choi, X. Li, A. Manivannan, D. Wang, *Nano Lett.* **2014**, *14*, 6329.

[112] J. Song, Z. Yu, M. L. Gordin, X. Li, H. Peng, D. Wang, *ACS Nano* **2015**, *9*, 11933.

[113] H. Gao, T. Zhou, Y. Zheng, Y. Liu, J. Chen, H. Liu, Z. Guo, *Adv. Energy Mater.* **2016**, *6*, 1601037.

[114] L. Pei, Q. Zhao, C. Chen, J. Liang, J. Chen, *ChemElectroChem* **2015**, *2*, 1652.

[115] Y. Zhu, Y. Wen, X. Fan, T. Gao, F. Han, C. Luo, S.-C. Liou, C. Wang, *ACS Nano* **2015**, *9*, 3254.

[116] C. Zhang, X. Wang, Q. Liang, X. Liu, Q. Weng, J. Liu, Y. Yang, Z. Dai, K. Ding, Y. Bando, J. Tang, D. Golberg, *Nano Lett.* **2016**, *16*, 2054.

[117] Y. Liu, A. Zhang, C. Shen, Q. Liu, X. Cao, Y. Ma, L. Chen, C. Lau, T.-C. Chen, F. Wei, C. Zhou, *ACS Nano* **2017**, *11*, 5530.

[118] W. Li, Z. Yang, M. Li, Y. Jiang, X. Wei, X. Zhong, L. Gu, Y. Yu, *Nano Lett.* **2016**, *16*, 1546.

[119] W. Li, S. Hu, X. Luo, Z. Li, X. Sun, M. Li, F. Liu, Y. Yu, *Adv. Mater.* **2017**, *29*, 1605820.

[120] R. W. Keyes, *Phys. Rev.* **1953**, *92*, 580.

[121] W. Lei, G. Liu, J. Zhang, M. Liu, *Chem. Soc. Rev.* **2017**, *46*, 3492.

[122] Y. Du, C. Ouyang, S. Shi, M. Lei, *J. Appl. Phys.* **2010**, *107*, 093718.

[123] K. P. S. S. Hembram, H. Jung, B. C. Yeo, S. J. Pai, S. Kim, K.-R. Lee, S. S. Han, *J. Phys. Chem. C* **2015**, *119*, 15041.

[124] T. Chen, P. Zhao, X. Guo, S. Zhang, *Nano Lett.* **2017**, *17*, 2299.

[125] V. V. Kulish, O. I. Malyi, C. Persson, P. Wu, *Phys. Chem. Chem. Phys.* **2015**, *17*, 13921.

[126] V. Nicolosi, M. Chhowalla, M. G. Kanatzidis, M. S. Strano, J. N. Coleman, *Science* **2013**, *340*, 1226419.

[127] L. Niu, J. N. Coleman, H. Zhang, H. Shin, M. Chhowalla, Z. Zheng, *Small* **2016**, *12*, 272.

[128] Z. Huang, H. Hou, Y. Zhang, C. Wang, X. Qiu, X. Ji, *Adv. Mater.* **2017**, *29*, 1702372.

[129] C. Chowdhury, S. Karmakar, A. Datta, *ACS Energy Lett.* **2016**, *1*, 253.

[130] G.-L. Xu, Z. Chen, G.-M. Zhong, Y. Liu, Y. Yang, T. Ma, Y. Ren, X. Zuo, X.-H. Wu, X. Zhang, K. Amine, *Nano Lett.* **2016**, *16*, 3955.

[131] J. Sun, H.-W. Lee, M. Pasta, H. Yuan, G. Zheng, Y. Sun, Y. Li, Y. Cui, *Nat. Nanotechnol.* **2015**, *10*, 980.

[132] M. Dahbi, N. Yabuuchi, M. Fukunishi, K. Kubota, K. Chihara, K. Tokiwa, X.-f. Yu, H. Ushiyama, K. Yamashita, J.-Y. Son, Y.-T. Cui, H. Oji, S. Komaba, *Chem. Mater.* **2016**, *28*, 1625.

[133] L. D. Ellis, B. N. Wilkes, T. D. Hatchard, M. N. Obrovac, *J. Electrochem. Soc.* **2014**, *161*, A416.

[134] A. Mali, A. Petric, *J. Phase Equilib. Diffus.* **2013**, *34*, 453.

[135] P. R. Abel, Y.-M. Lin, T. de Souza, C.-Y. Chou, A. Gupta, J. B. Goodenough, G. S. Hwang, A. Heller, C. B. Mullins, *J. Phys. Chem. C* **2013**, *117*, 18885.

[136] D. Su, S. Dou, G. Wang, *Nano Energy* **2015**, *12*, 88.

[137] S. A. Webb, L. Baggetto, C. A. Bridges, G. M. Veith, *J. Power Sources* **2014**, *248*, 1105.

[138] J. R. Szczech, S. Jin, *Energy Environ. Sci.* **2011**, *4*, 56.

[139] J. Songster, A. D. Pelton, *J. Phase Equilib.* **1992**, *13*, 67.

[140] O. Malyi, V. V. Kulish, T. L. Tan, S. Manzhos, *Nano Energy* **2013**, *2*, 1149.

[141] F. Legrain, O. I. Malyi, S. Manzhos, *Comput. Mater. Sci.* **2014**, *94*, 214.

[142] V. V. Kulish, O. I. Malyi, M.-F. Ng, Z. Chen, S. Manzhos, P. Wu, *Phys. Chem. Chem. Phys.* **2014**, *16*, 4260.

[143] S. C. Jung, D. S. Jung, J. W. Choi, Y.-K. Han, *J. Phys. Chem. Lett.* **2014**, *5*, 1283.

[144] Y. Xu, E. Swaans, S. Basak, H. W. Zandbergen, D. M. Borsa, F. M. Mulder, *Adv. Energy Mater.* **2016**, *6*, 1501436.

[145] Q. Zhao, Y. Huang, X. Hu, *Electrochem. Commun.* **2016**, *70*, 8.

[146] L. Zhang, X. Hu, C. Chen, H. Guo, X. Liu, G. Xu, H. Zhong, S. Cheng, P. Wu, J. Meng, Y. Huang, S. Dou, H. Liu, *Adv. Mater.* **2017**, *29*, 1604708.

[147] M. Stojić, D. Kostić, B. Stošić, *Physica B+C* **1986**, *138*, 125.

[148] L. Baggetto, J. K. Keum, J. F. Browning, G. M. Veith, *Electrochem. Commun.* **2013**, *34*, 41.

[149] A. Kohandehghan, K. Cui, M. Kupsta, J. Ding, E. Memarzadeh Lotfabad, W. P. Kalisvaart, D. Mitlin, *Nano Lett.* **2014**, *14*, 5873.

[150] X. Lu, E. R. Adkins, Y. He, L. Zhong, L. Luo, S. X. Mao, C.-M. Wang, B. A. Korgel, *Chem. Mater.* **2016**, *28*, 1236.

[151] X. Wang, L. Fan, D. Gong, J. Zhu, Q. Zhang, B. Lu, *Adv. Funct. Mater.* **2016**, *26*, 1104.

[152] F. Yang, F. Yu, Z. Zhang, K. Zhang, Y. Lai, J. Li, *Chem. Eur. J.* **2016**, *22*, 2333.

[153] H. Yin, Q. Li, M. Cao, W. Zhang, H. Zhao, C. Li, K. Huo, M. Zhu, *Nano Res.* **2017**, *10*, 2156.

[154] H. Kang, Y. Liu, K. Cao, Y. Zhao, L. Jiao, Y. Wang, H. Yuan, *J. Mater. Chem. A* **2015**, *3*, 17899.

[155] I. Hasa, J. Hassoun, S. Passerini, *Nano Res.* **2017** DOI:10.1007/s12274-017-1513-7.

[156] A. Ponrouch, D. Monti, A. Boschin, B. Steen, P. Johansson, M. R. Palacin, *J. Mater. Chem. A* **2015**, *3*, 22.

[157] M. K. Datta, R. Epur, P. Saha, K. Kadakia, S. K. Park, P. N. Kumta, *J. Power Sources* **2013**, *225*, 316.

[158] D. Bresser, F. Mueller, D. Buchholz, E. Paillard, S. Passerini, *Electrochim. Acta* **2014**, *128*, 163.

[159] X. Han, Y. Liu, Z. Jia, Y.-C. Chen, J. Wan, N. Weadock, K. J. Gaskell, T. Li, L. Hu, *Nano Lett.* **2014**, *14*, 139.

[160] Y. Yang, X. Yang, Y. Zhang, H. Hou, M. Jing, Y. Zhu, L. Fang, Q. Chen, X. Ji, *J. Power Sources* **2015**, *282*, 358.

[161] H. Hou, M. Jing, Y. Zhang, J. Chen, Z. Huang, X. Ji, *J. Mater. Chem. A* **2015**, *3*, 17549.

[162] T. Ramireddy, N. Sharma, T. Xing, Y. Chen, J. Leforestier, A. M. Glushenkov, *ACS Appl. Mater. Interfaces* **2016**, *8*, 30152.

[163] S. Liao, G. Yang, C. Wang, *RSC Adv.* **2016**, *6*, 114790.

[164] C. Yang, W. Li, Z. Yang, L. Gu, Y. Yu, *Nano Energy* **2015**, *18*, 12.

[165] D.-H. Nam, K.-S. Hong, S.-J. Lim, M.-J. Kim, H.-S. Kwon, *Small* **2015**, *11*, 2885.

[166] H. Hou, M. Jing, Y. Yang, Y. Zhang, W. Song, X. Yang, J. Chen, Q. Chen, X. Ji, *J. Power Sources* **2015**, *284*, 227.

[167] J. Duan, W. Zhang, C. Wu, Q. Fan, W. Zhang, X. Hu, Y. Huang, *Nano Energy* **2015**, *16*, 479.

[168] J. P. Gabano, V. Déchenaux, G. Gerbier, J. Jammet, *J. Electrochem. Soc.* **1972**, *119*, 459.

[169] M. M. Thackeray, W. I. F. David, J. B. Goodenough, *Mater. Res. Bull.* **1982**, *17*, 785.

[170] P. Poizot, S. Laruelle, S. Grugeon, L. Dupont, J. M. Tarascon, *Nature* **2000**, *407*, 496.

[171] M. Jiang, X. Wang, Y. Shen, H. Hu, Y. Fu, X. Yang, *Electrochim. Acta* **2015**, *186*, 7.

[172] J. Nava-Avendaño, M. E. Arroyo-de Dompablo, C. Frontera, J. A. Ayllón, M. R. Palacín, *Solid State Ionics* **2015**, *278*, 106.

[173] F. Klein, B. Jache, A. Bhide, P. Adelhelm, *Phys. Chem. Chem. Phys.* **2013**, *15*, 15876.

[174] L. Li, R. Jacobs, P. Gao, L. Gan, F. Wang, D. Morgan, S. Jin, *J. Am. Chem. Soc.* **2016**, *138*, 2838.

[175] S. Hariharan, K. Saravanan, P. Balaya, *Electrochem. Commun.* **2013**, *31*, 5.

[176] Z. Jian, B. Zhao, P. Liu, F. Li, M. Zheng, M. Chen, Y. Shi, H. Zhou, *Chem. Commun.* **2014**, *50*, 1215.

[177] Y. Liu, N. Zhang, C. Yu, L. Jiao, J. Chen, *Nano Lett.* **2016**, *16*, 3321.

[178] Q. Zhou, L. Liu, Z. Huang, L. Yi, X. Wang, G. Cao, *J. Mater. Chem. A* **2016**, *4*, 5505.

[179] Z. Li, L. Zhang, X. Ge, C. Li, S. Dong, C. Wang, L. Yin, *Nano Energy* **2017**, *32*, 494.

[180] F. Zhao, N. Han, W. Huang, J. Li, H. Ye, F. Chen, Y. Li, *J. Mater. Chem. A* **2015**, *3*, 21754.

[181] X. Song, X. Li, Z. Bai, B. Yan, D. Li, X. Sun, *Nano Energy* **2016**, *26*, 533.

[182] R. Alcántara, M. Jaraba, P. Lavela, J. L. Tirado, *Chem. Mater.* **2002**, *14*, 2847.

[183] P. Kollu, P. R. Kumar, C. Santosh, D. K. Kim, A. N. Grace, *RSC Adv.* **2015**, *5*, 63304.

[184] X. Zhang, T. Chen, D. Yan, W. Qin, B. Hu, Z. Sun, L. Pan, *Electrochim. Acta* **2015**, *180*, 616.

[185] N. Zhang, X. Han, Y. Liu, X. Hu, Q. Zhao, J. Chen, *Adv. Energy Mater.* **2015**, *5*, 1401123.

[186] L. Zhang, H. B. Wu, X. W. Lou, *Adv. Energy Mater.* **2014**, *4*, 1300958.

[187] M. C. López, P. Lavela, G. F. Ortiz, J. L. Tirado, *Electrochem. Commun.* **2013**, *27*, 152.

[188] B. Huang, K. Tai, M. Zhang, Y. Xiao, S. J. Dillon, *Electrochim. Acta* **2014**, *118*, 143.

[189] S. Hariharan, K. Saravanan, V. Ramar, P. Balaya, *Phys. Chem. Chem. Phys.* **2013**, *15*, 2945.

[190] P. R. Kumar, Y. H. Jung, K. K. Bharathi, C. H. Lim, D. K. Kim, *Electrochim. Acta* **2014**, *146*, 503.

[191] H. Liu, M. Jia, Q. Zhu, B. Cao, R. Chen, Y. Wang, F. Wu, B. Xu, *ACS Appl. Mater. Interfaces* **2016**, *8*, 26878.

[192] L.-Y. Qi, Y.-W. Zhang, Z.-C. Zuo, Y.-L. Xin, C.-K. Yang, B. Wu, X.-X. Zhang, H.-H. Zhou, *J. Mater. Chem. A* **2016**, *4*, 8822.

[193] S.-M. Oh, S.-T. Myung, C. S. Yoon, J. Lu, J. Hassoun, B. Scrosati, K. Amine, Y.-K. Sun, *Nano Lett.* **2014**, *14*, 1620.

[194] M. Valvo, F. Lindgren, U. Lafont, F. Björefors, K. Edström, *J. Power Sources* **2014**, *245*, 967.

[195] L. Yu, L. P. Wang, S. Xi, P. Yang, Y. Du, M. Srinivasan, Z. J. Xu, *Chem. Mater.* **2015**, *27*, 5340.

[196] Y. Wang, C. Wang, Y. Wang, H. Liu, Z. Huang, *J. Mater. Chem. A* **2016**, *4*, 5428.

[197] M. M. Rahman, A. M. Glushenkov, T. Ramireddy, Y. Chen, *Chem. Commun.* **2014**, *50*, 5057.

[198] G. Longoni, M. Fiore, J.-H. Kim, Y. H. Jung, D. K. Kim, C. M. Mari, R. Ruffo, *J. Power Sources* **2016**, *332*, 42.

[199] Z. Jian, P. Liu, F. Li, M. Chen, H. Zhou, *J. Mater. Chem. A* **2014**, *2*, 13805.

[200] J. Yang, T. Zhou, R. Zhu, X. Chen, Z. Guo, J. Fan, H. K. Liu, W.-X. Zhang, *Adv. Mater. Interfaces* **2016**, *3*, 1500464.

[201] Q.-L. Zhu, Q. Xu, *Chem. Soc. Rev.* **2014**, *43*, 5468.

[202] Y. Zhao, Z. Song, X. Li, Q. Sun, N. Cheng, S. Lawes, X. Sun, *Energy Storage Mater.* **2016**, *2*, 35.

[203] W. Kang, Y. Zhang, L. Fan, L. Zhang, F. Dai, R. Wang, D. Sun, *ACS Appl. Mater. Interfaces* **2017**, *9*, 10602.

[204] V. Augustyn, P. Simon, B. Dunn, *Energy Environ. Sci.* **2014**, *7*, 1597.

[205] C. Chen, Y. Wen, X. Hu, X. Ji, M. Yan, L. Mai, P. Hu, B. Shan, Y. Huang, *Nat. Commun.* **2015**, *6*, 6929.

[206] D. Yuhai, W. Yunxiao, T. Dongliang, X. Jiantie, Z. Zhijia, L. Qiannan, R. Boyang, M. Jianmin, S. Ziqi, D. Shi Xue, *2D Mater.* **2017**, *4*, 015022.

[207] D. Chen, L. Peng, Y. Yuan, Y. Zhu, Z. Fang, C. Yan, G. Chen, R. Shahbazian-Yassar, J. Lu, K. Amine, G. Yu, *Nano Lett.* **2017**, *17*, 3907.

[208] S. Ko, J.-I. Lee, H. S. Yang, S. Park, U. Jeong, *Adv. Mater.* **2012**, *24*, 4451.

[209] L. Wang, K. Zhang, Z. Hu, W. Duan, F. Cheng, J. Chen, *Nano Res.* **2014**, *7*, 199.

[210] S. Yuan, X.-l. Huang, D.-l. Ma, H.-g. Wang, F.-z. Meng, X.-b. Zhang, *Adv. Mater.* **2014**, *26*, 2273.

[211] Z. Zhang, J. Feng, L. Ci, Y. Tian, S. Xiong, *Mater. Technol.* **2016**, *31*, 497.

[212] D. Li, D. Yan, X. Zhang, J. Li, T. Lu, L. Pan, *J. Colloid Interface Sci.* **2017**, *497*, 350.

[213] A. Y. Kim, M. K. Kim, K. Cho, J.-Y. Woo, Y. Lee, S.-H. Han, D. Byun, W. Choi, J. K. Lee, *ACS Appl. Mater. Interfaces* **2016**, *8*, 19514.

[214] S.-W. Kim, D.-H. Seo, X. Ma, G. Ceder, K. Kang, *Adv. Energy Mater.* **2012**, *2*, 710.

[215] K. He, F. Lin, Y. Zhu, X. Yu, J. Li, R. Lin, D. Nordlund, T.-C. Weng, R. M. Richards, X.-Q. Yang, M. M. Doeff, E. A. Stach, Y. Mo, H. L. Xin, D. Su, *Nano Lett.* **2015**, *15*, 5755.

[216] Y. V. Kaneti, J. Zhang, Y.-B. He, Z. Wang, S. Tanaka, M. S. A. Hossain, Z.-Z. Pan, B. Xiang, Q.-H. Yang, Y. Yamauchi, *J. Mater. Chem. A* **2017**, *5*, 15356.

[217] F. Zou, Y.-M. Chen, K. Liu, Z. Yu, W. Liang, S. M. Bhaway, M. Gao, Y. Zhu, *ACS Nano* **2016**, *10*, 377.

[218] X. Zhang, G. Zhu, D. Yan, T. Lu, L. Pan, *J. Alloys Compd.* **2017**, *710*, 575.

[219] Y.-X. Wang, J. Yang, S.-L. Chou, H. K. Liu, W.-x. Zhang, D. Zhao, S. X. Dou, *Nat. Commun.* **2015**, *6*, 8689.

[220] Y. Shao-Horn, S. Osmialowski, Q. C. Horn, *J. Electrochem. Soc.* **2002**, *149*, A1499.

[221] J. Liu, Y. Wen, Y. Wang, P. A. van Aken, J. Maier, Y. Yu, *Adv. Mater.* **2014**, *26*, 6025.

[222] T. B. Kim, J. W. Choi, H. S. Ryu, G. B. Cho, K. W. Kim, J. H. Ahn, K. K. Cho, H. J. Ahn, *J. Power Sources* **2007**, *174*, 1275.

[223] T. B. Kim, W. H. Jung, H. S. Ryu, K. W. Kim, J. H. Ahn, K. K. Cho, G. B. Cho, T. H. Nam, I. S. Ahn, H. J. Ahn, *J. Alloys Compd.* **2008**, *449*, 304.

[224] Z. Shadike, Y.-N. Zhou, F. Ding, L. Sang, K.-W. Nam, X.-Q. Yang, Z.-W. Fu, *J. Power Sources* **2014**, *260*, 72.

[225] Z. Hu, Z. Zhu, F. Cheng, K. Zhang, J. Wang, C. Chen, J. Chen, *Energy Environ. Sci.* **2015**, *8*, 1309.

[226] M. Walter, T. Zund, M. V. Kovalenko, *Nanoscale* **2015**, *7*, 9158.

[227] Z. Liu, T. Lu, T. Song, X.-Y. Yu, X. W. Lou, U. Paik, *Energy Environ. Sci.* **2017**, *10*, 1576.

[228] K. Zhang, M. Park, L. Zhou, G.-H. Lee, J. Shin, Z. Hu, S.-L. Chou, J. Chen, Y.-M. Kang, *Angew. Chem., Int. Ed.* **2016**, *55*, 12822.

[229] K. Chen, W. Zhang, L. Xue, W. Chen, X. Xiang, M. Wan, Y. Huang, *ACS Appl. Mater. Interfaces* **2017**, *9*, 1536.

[230] L. Fei, Q. Lin, B. Yuan, G. Chen, P. Xie, Y. Li, Y. Xu, S. Deng, S. Smirnov, H. Luo, *ACS Appl. Mater. Interfaces* **2013**, *5*, 5330.

[231] S. Y. Lee, Y. C. Kang, *Chem. Eur. J.* **2016**, *22*, 2769.

[232] J. S. Cho, J.-S. Park, Y. C. Kang, *Nano Res.* **2017**, *10*, 897.

[233] Y. Chen, X. Li, K. Park, L. Zhou, H. Huang, Y.-W. Mai, J. B. Goodenough, *Angew. Chem., Int. Ed.* **2016**, *55*, 15831.

[234] Y. N. Ko, S. H. Choi, S. B. Park, Y. C. Kang, *Chem. Asian J.* **2014**, *9*, 572.

[235] S. Peng, X. Han, L. Li, Z. Zhu, F. Cheng, M. Srinivansan, S. Adams, S. Ramakrishna, *Small* **2016**, *12*, 1359.

[236] Z. Shadike, M.-H. Cao, F. Ding, L. Sang, Z.-W. Fu, *Chem. Commun.* **2015**, *51*, 10486.

[237] F. Han, C. Y. Jun Tan, Z. Gao, *J. Power Sources* **2017**, *339*, 41.

[238] F. Han, C. Zhang, B. Sun, W. Tang, J. Yang, X. Li, *Carbon* **2017**, *118*, 731.

[239] Z. Li, W. Feng, Y. Lin, X. Liu, H. Fei, *RSC Adv.* **2016**, *6*, 70632.

[240] N. Mahmood, C. Zhang, J. Jiang, F. Liu, Y. Hou, *Chem. Eur. J.* **2013**, *19*, 5183.

[241] P. Long, Z. Zhang, G. Peng, Q. Zhang, D. Liu, X. Xu, X. Yao, *New J. Chem.* **2017**, *41*, 9184.

[242] Y. Du, X. Zhu, X. Zhou, L. Hu, Z. Dai, J. Bao, *J. Mater. Chem. A* **2015**, *3*, 6787.

[243] X. Liu, H. Liu, Y. Zhao, Y. Dong, Q. Fan, Q. Kuang, *Langmuir* **2016**, *32*, 12593.

[244] J. Li, D. Yan, T. Lu, W. Qin, Y. Yao, L. Pan, *ACS Appl. Mater. Interfaces* **2017**, *9*, 2309.

[245] X. Xu, S. Ji, M. Gu, J. Liu, *ACS Appl. Mater. Interfaces* **2015**, *7*, 20957.

[246] X. Xia, Q. Wang, Q. Zhu, J. Xie, J. Wang, D. Zhuang, S. Zhang, G. Cao, X. Zhao, *Mater. Today Energy* **2017**, *5*, 99.

[247] X. Xia, J. Xie, S. Zhang, B. Pan, G. Cao, X. Zhao, *Inorg. Chem. Front.* **2017**, *4*, 131.

[248] B. Radisavljevic, A. Kis, *Nat. Mater.* **2013**, *12*, 815.

[249] N. Mahmood, T. Tang, Y. Hou, *Adv. Energy Mater.* **2016**, *6*, 1600374.

[250] J. Park, J.-S. Kim, J.-W. Park, T.-H. Nam, K.-W. Kim, J.-H. Ahn, G. Wang, H.-J. Ahn, *Electrochim. Acta* **2013**, *92*, 427.

[251] Y.-X. Wang, K. H. Seng, S.-L. Chou, J.-Z. Wang, Z. Guo, D. Wexler, H.-K. Liu, S.-X. Dou, *Chem. Commun.* **2014**, *50*, 10730.

[252] L. David, R. Bhandavat, G. Singh, *ACS Nano* **2014**, *8*, 1759.

[253] C. Zhu, X. Mu, P. A. van Aken, Y. Yu, J. Maier, *Angew. Chem., Int. Ed.* **2014**, *53*, 2152.

[254] Z. Hu, L. Wang, K. Zhang, J. Wang, F. Cheng, Z. Tao, J. Chen, *Angew. Chem.* **2014**, *126*, 13008.

[255] H. Wang, H. Jiang, Y. Hu, N. Li, X. Zhao, C. Li, *J. Mater. Chem. A* **2017**, *5*, 5383.

[256] W. Ren, H. Zhang, C. Guan, C. Cheng, *Adv. Funct. Mater.* **2017**, *27*, 1702116.

[257] Y. Liu, N. Zhang, H. Kang, M. Shang, L. Jiao, J. Chen, *Chem. Eur. J.* **2015**, *21*, 11878.

[258] D. B. Putungan, S.-H. Lin, J.-L. Kuo, *ACS Appl. Mater. Interfaces* **2016**, *8*, 18754.

[259] Y. Wang, D. Kong, W. Shi, B. Liu, G. J. Sim, Q. Ge, H. Y. Yang, *Adv. Energy Mater.* **2016**, *6*, 1601057.

[260] X. Ji, K. T. Lee, L. F. Nazar, *Nat. Mater.* **2009**, *8*, 500.

[261] Q. Pang, Y. Gao, Y. Zhao, Y. Ju, H. Qiu, Y. Wei, B. Liu, B. Zou, F. Du, G. Chen, *Chem. Eur. J.* **2017**, *23*, 7074.

[262] J. Zhou, L. Wang, M. Yang, J. Wu, F. Chen, W. Huang, N. Han, H. Ye, F. Zhao, Y. Li, Y. Li, *Adv. Mater.* **2017**, *29*, 1702061.

[263] C. Yang, X. Ou, X. Xiong, F. Zheng, R. Hu, Y. Chen, M. Liu, K. Huang, *Energy Environ. Sci.* **2017**, *10*, 107.

[264] X. Ou, X. Xiong, F. Zheng, C. Yang, Z. Lin, R. Hu, C. Jin, Y. Chen, M. Liu, *J. Power Sources* **2016**, *325*, 410.

[265] Z. Hu, Q. Liu, S.-L. Chou, S.-X. Dou, *Adv. Mater.* **2017** DOI: 10.1002/adma.201700606.

[266] J.-L. Yue, Q. Sun, Z.-W. Fu, *Chem. Commun.* **2013**, *49*, 5868.

[267] Y. N. Ko, S. H. Choi, S. B. Park, Y. C. Kang, *Nanoscale* **2014**, *6*, 10511.

[268] K. Zhang, Z. Hu, X. Liu, Z. Tao, J. Chen, *Adv. Mater.* **2015**, *27*, 3305.

[269] C. Wu, Y. Jiang, P. Kopold, P. A. van Aken, J. Maier, Y. Yu, *Adv. Mater.* **2016**, *28*, 7276.

[270] Y. N. Ko, S. H. Choi, Y. C. Kang, *ACS Appl. Mater. Interfaces* **2016**, *8*, 6449.

[271] X. Wang, D. Kong, Z. X. Huang, Y. Wang, H. Y. Yang, *Small* **2017**, *13*, 1603980.

[272] Z. Zhang, X. Yang, Y. Fu, *RSC Adv.* **2016**, *6*, 12726.

[273] X. Ou, J. Li, F. Zheng, P. Wu, Q. Pan, X. Xiong, C. Yang, M. Liu, *J. Power Sources* **2017**, *343*, 483.

[274] K. Zhang, M. Park, L. Zhou, G.-H. Lee, W. Li, Y.-M. Kang, J. Chen, *Adv. Funct. Mater.* **2016**, *26*, 6728.

[275] Y. Tang, Z. Zhao, X. Hao, Y. Wang, Y. Liu, Y. Hou, Q. Yang, X. Wang, J. Qiu, *J. Mater. Chem. A* **2017**, *5*, 13591.

[276] Y. Zhang, A. Pan, L. Ding, Z. Zhou, Y. Wang, S. Niu, S. Liang, G. Cao, *ACS Appl. Mater. Interfaces* **2017**, *9*, 3624.

[277] X. Li, A. L. Hector, J. R. Owen, *J. Phys. Chem. C* **2014**, *118*, 29568.

[278] S. Liu, J. Liu, W. Wang, L. Yang, K. Zhu, H. Wang, *RSC Adv.* **2016**, *6*, 86131.

[279] S.-L. Liu, J. Huang, J. Liu, M. Lei, J. Min, S. Li, G. Liu, *Mater. Lett.* **2016**, *172*, 56.

[280] L. Wang, J. Sun, R. Song, S. Yang, H. Song, *Adv. Energy Mater.* **2016**, *6*, 1502067.

[281] W.-J. Li, S.-L. Chou, J.-Z. Wang, H.-K. Liu, S.-X. Dou, *Chem. Commun.* **2015**, *51*, 3682.

[282] W.-J. Li, Q.-R. Yang, S.-L. Chou, J.-Z. Wang, H.-K. Liu, *J. Power Sources* **2015**, *294*, 627.

[283] F. Han, C. Y. J. Tan, Z. Gao, *ChemElectroChem* **2016**, *3*, 1054.

[284] W. Zhang, M. Dahbi, S. Amagasa, Y. Yamada, S. Komaba, *Electrochem. Commun.* **2016**, *69*, 11.

[285] X. Li, W. Li, J. Yu, H. Zhang, Z. Shi, Z. Guo, *J. Alloys Compd.* **2017**, *724*, 932.

[286] C. Wu, P. Kopold, P. A. van Aken, J. Maier, Y. Yu, *Adv. Mater.* **2017**, *29*, 1604015.

[287] M. Fan, Y. Chen, Y. Xie, T. Yang, X. Shen, N. Xu, H. Yu, C. Yan, *Adv. Funct. Mater.* **2016**, *26*, 5019.

[288] X. Ge, Z. Li, L. Yin, *Nano Energy* **2017**, *32*, 117.

[289] K. Zhu, J. Liu, S. Li, L. Liu, L. Yang, S. Liu, H. Wang, T. Xie, *Adv. Mater. Interfaces* **2017**, *4*, 1700377.

[290] K. Zhang, M. Park, J. Zhang, G.-H. Lee, J. Shin, Y.-M. Kang, *Nano Res.* **2017** DOI: 10.1007/s12274-017-1649-5.

[291] D. Su, X. Xie, G. Wang, *Chem. Eur. J.* **2014**, *20*, 3192.

[292] Y. Wang, D. Su, C. Wang, G. Wang, *Electrochem. Commun.* **2013**, *29*, 8.

[293] T. Zhou, W. K. Pang, C. Zhang, J. Yang, Z. Chen, H. K. Liu, Z. Guo, *ACS Nano* **2014**, *8*, 8323.

[294] M. Hu, Y. Jiang, W. Sun, H. Wang, C. Jin, M. Yan, *ACS Appl. Mater. Interfaces* **2014**, *6*, 19449.

[295] D. Y. W. Yu, P. V. Prikhodchenko, C. W. Mason, S. K. Batabyal, J. Gun, S. Sladkevich, A. G. Medvedev, O. Lev, *Nat. Commun.* **2013**, *4*, 3922.

[296] Z. Li, J. Ding, D. Mitlin, *Acc. Chem. Res.* **2015**, *48*, 1657.

[297] Y.-X. Wang, Y.-G. Lim, M.-S. Park, S.-L. Chou, J. H. Kim, H.-K. Liu, S.-X. Dou, Y.-J. Kim, *J. Mater. Chem. A* **2014**, *2*, 529.

[298] J. Qin, N. Zhao, C. Shi, E. Liu, F. He, L. Ma, Q. Li, J. Li, C. He, *J. Mater. Chem. A* **2017**, *5*, 10946.

[299] L. Fan, X. Li, B. Yan, J. Feng, D. Xiong, D. Li, L. Gu, Y. Wen, S. Lawes, X. Sun, *Adv. Energy Mater.* **2016**, *6*, 1502057.

[300] J. Cui, Z.-L. Xu, S. Yao, J. Huang, J.-Q. Huang, S. Abouali, M. A. Garakani, X. Ning, J.-K. Kim, *J. Mater. Chem. A* **2016**, *4*, 10964.

[301] Y. C. Lu, C. Ma, J. Alvarado, T. Kidera, N. Dimov, Y. S. Meng, S. Okada, *J. Power Sources* **2015**, *284*, 287.

[302] M. Chen, D. Chao, J. Liu, J. Yan, B. Zhang, Y. Huang, J. Lin, Z. X. Shen, *Adv. Funct. Mater.* **2017**, *27*, 1606232.

[303] F. Zhang, J. Zhu, D. Zhang, U. Schwingenschlögl, H. N. Alshareef, *Nano Lett.* **2017**, *17*, 1302.

[304] B. Qin, H. Zhang, T. Diemant, D. Geiger, R. Raccichini, R. J. Behm, U. Kaiser, A. Varzi, S. Passerini, *ACS Appl. Mater. Interfaces* **2017**, *9*, 26797.

[305] Y. Xiao, S. H. Lee, Y.-K. Sun, *Adv. Energy Mater.* **2017**, *7*, 1601329.

[306] B. Qu, C. Ma, G. Ji, C. Xu, J. Xu, Y. S. Meng, T. Wang, J. Y. Lee, *Adv. Mater.* **2014**, *26*, 3854.

[307] Y. Jiang, M. Wei, J. Feng, Y. Ma, S. Xiong, *Energy Environ. Sci.* **2016**, *9*, 1430.

[308] F. Tu, X. Xu, P. Wang, L. Si, X. Zhou, J. Bao, *J. Phys. Chem. C* **2017**, *121*, 3261.

[309] L. Wu, H. Lu, L. Xiao, J. Qian, X. Ai, H. Yang, Y. Cao, *J. Mater. Chem. A* **2014**, *2*, 16424.

[310] C. Zhu, P. Kopold, W. Li, P. A. van Aken, J. Maier, Y. Yu, *Adv. Sci.* **2015**, *2*, 1500200.

[311] J. Choi, N. R. Kim, K. Lim, K. Ku, H. J. Yoon, J. G. Kang, K. Kang, P. V. Braun, H.-J. Jin, Y. S. Yun, *Small* **2017**, *13*, 1700767.

[312] X. Xiong, C. Yang, G. Wang, Y. Lin, X. Ou, J.-H. Wang, B. Zhao, M. Liu, Z. Lin, K. Huang, *Energy Environ. Sci.* **2017**, *10*, 1757.

[313] S. Yao, J. Cui, Z. Lu, Z.-L. Xu, L. Qin, J. Huang, Z. Sadighi, F. Ciucci, J.-K. Kim, *Adv. Energy Mater.* **2017**, *7*, 1602149.

[314] Y. Kim, Y. Kim, A. Choi, S. Woo, D. Mok, N.-S. Choi, Y. S. Jung, J. H. Ryu, S. M. Oh, K. T. Lee, *Adv. Mater.* **2014**, *26*, 4139.

[315] Q. Li, Z. Li, Z. Zhang, C. Li, J. Ma, C. Wang, X. Ge, S. Dong, L. Yin, *Adv. Energy Mater.* **2016**, *6*, 1600376.

[316] X. Fan, T. Gao, C. Luo, F. Wang, J. Hu, C. Wang, *Nano Energy* **2017**, *38*, 350.

[317] J. Liu, P. Kopold, C. Wu, P. A. van Aken, J. Maier, Y. Yu, *Energy Environ. Sci.* **2015**, *8*, 3531.

[319] E. Pomerantseva, Y. Gogotsi, *Nature Energy* **2017**, *2*, 17089.

[318] L. Ma, P. Yan, s. wu, G. Zhu, Y. Shen, *J. Mater. Chem. A* **2017**, *5*, 16994.

[320] W.-H. Ryu, H. Wilson, S. Sohn, J. Li, X. Tong, E. Shaulsky, J. Schroers, M. Elimelech, A. D. Taylor, *ACS Nano* **2016**, *10*, 3257.

[321] N. Wang, Z. Bai, Y. Qian, J. Yang, *Adv. Mater.* **2016**, *28*, 4126.

[322] X. Hong, J. Kim, S.-F. Shi, Y. Zhang, C. Jin, Y. Sun, S. Tongay, J. Wu, Y. Zhang, F. Wang, *Nat. Nanotechnol.* **2014**, *9*, 682.

[323] Y. Zheng, T. Zhou, C. Zhang, J. Mao, H. Liu, Z. Guo, *Angew. Chem., Int. Ed.* **2016**, *55*, 3408.

[324] C. W. Lee, J.-C. Kim, S. Park, H. J. Song, D.-W. Kim, *Nano Energy* **2015**, *15*, 479.

[325] Y. Jiang, Y. Guo, W. Lu, Z. Feng, B. Xi, S. Kai, J. Zhang, J. Feng, S. Xiong, *ACS Appl. Mater. Interfaces* **2017**, DOI: 10.1021/acsami.7b06572.

[326] J. Wang, J. Liu, H. Yang, D. Chao, J. Yan, S. V. Savilov, J. Lin, Z. X. Shen, *Nano Energy* **2016**, *20*, 1.

[327] S. Dong, C. Li, X. Ge, Z. Li, X. Miao, L. Yin, *ACS Nano* **2017**, *11*, 6474.

[328] S. Liu, J. Feng, X. Bian, J. Liu, H. Xu, Y. An, *Energy Environ. Sci.* **2017**, *10*, 1222.

[329] W. Ren, H. Zhang, C. Guan, C. Cheng, *Green Energy Environ.* **2017**, DOI: 10.1016/j.gee.2017.09.005.

[330] W. Ren, W. Zhou, H. Zhang, C. Cheng, *ACS Appl. Mater. Interfaces* **2017**, *9*, 487.

[331] T. Wu, S. Zhang, Q. He, X. Hong, F. Wang, X. Wu, J. Yang, Z. Wen, *ACS Appl. Mater. Interfaces* **2017**, *9*, 28549.

[332] M. Á. Muñoz-Márquez, D. Saurel, J. L. Gómez-Cámer, M. Casas-Cabanas, E. Castillo-Martínez, T. Rojo, *Adv. Energy Mater.* **2017**, *7*, 1700463.

[333] K.-l. Hong, L. Qie, R. Zeng, Z.-q. Yi, W. Zhang, D. Wang, W. Yin, C. Wu, Q.-j. Fan, W.-x. Zhang, Y.-h. Huang, *J. Mater. Chem. A* **2014**, *2*, 12733.

[334] E. Memarzadeh Lotfabad, P. Kalisvaart, A. Kohandehghan, D. Karpuzov, D. Mitlin, *J. Mater. Chem. A* **2014**, *2*, 19685.

[335] Y. Li, Y.-S. Hu, X. Qi, X. Rong, H. Li, X. Huang, L. Chen, *Energy Storage Mater.* **2016**, *5*, 191.

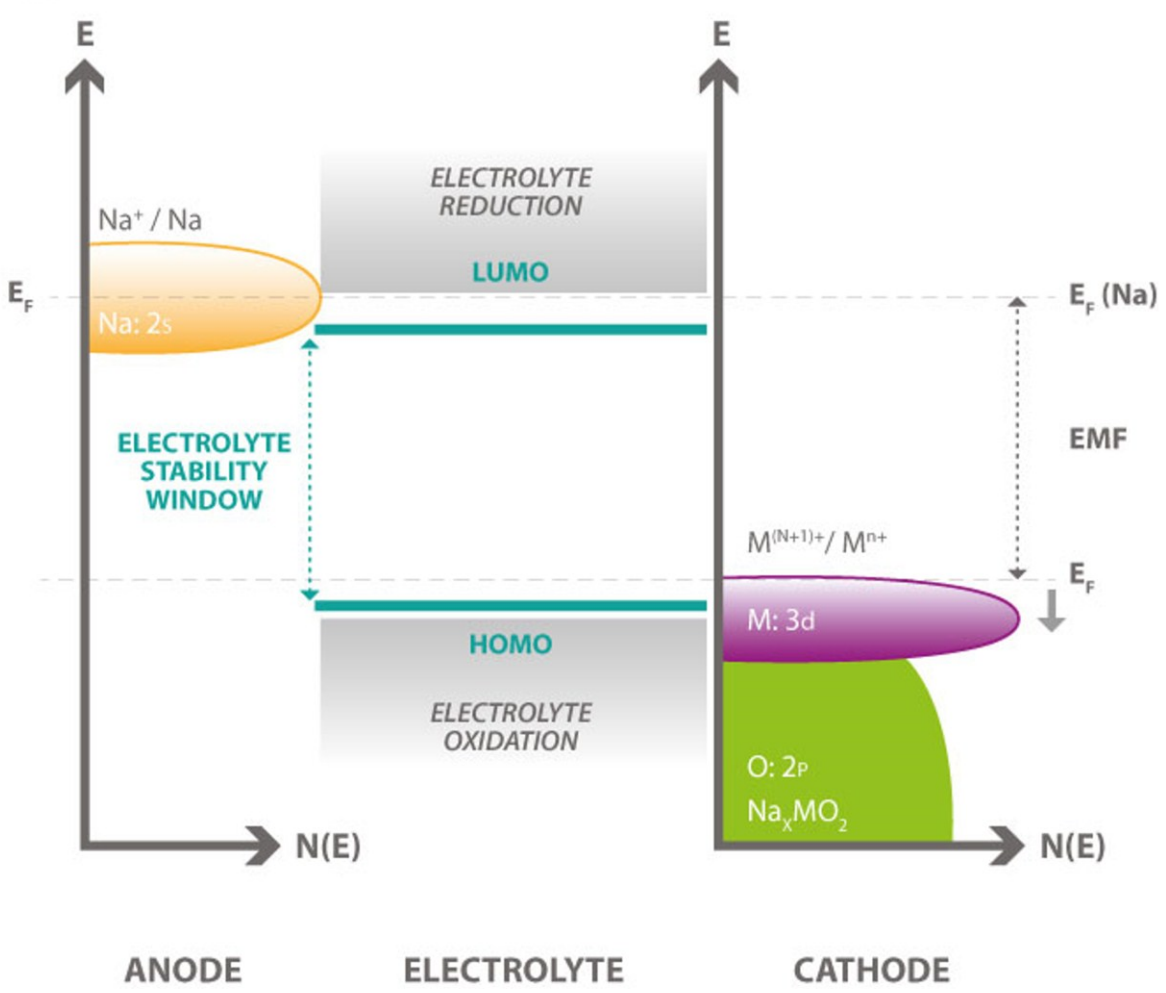

Figure 1. Schematic energy level diagram illustrating the origin of the EMF (electromotive force). The Fermi level of the Na metal anode is reported above the LUMO of the electrolyte indicating reduction of electrolyte and SEI interphase formation. During de-intercalation of sodium at the cathode, the Fermi level will shift down as indicated by the grey arrow.

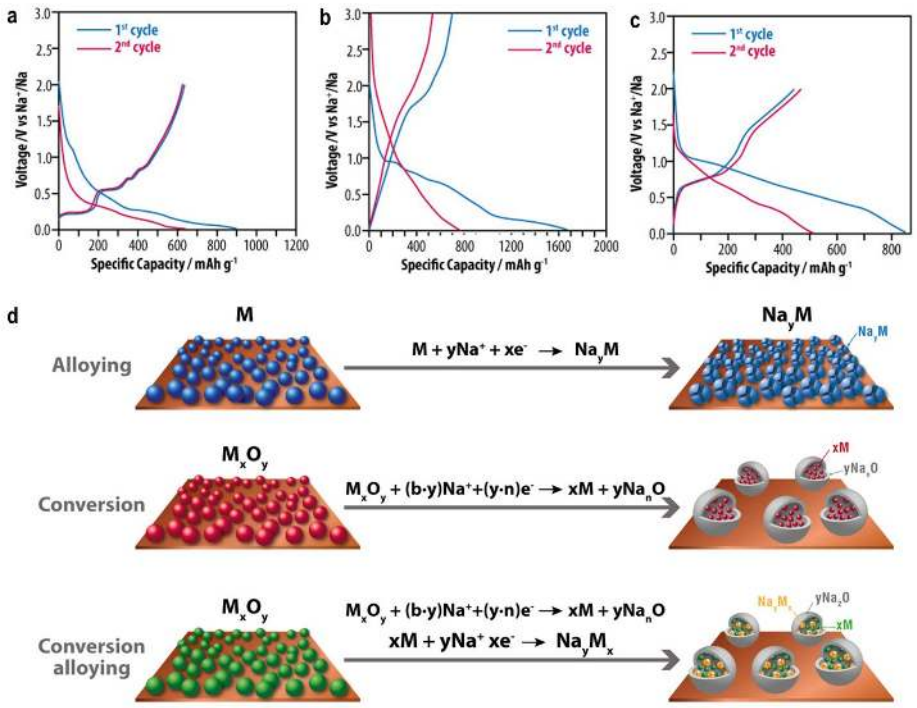

Figure 2. a) Typical voltage profile of alloying Sn NDs@PNC anode. Reproduced with permission.[33] Copyright 2015, Wiley-VCH.b) Typical voltage profile of conversion MoS_2/RGO anode. Reproduced with permission.[34] Copyright 2015, Wiley-VCH.c) Typical voltage profile of conversion-alloying Sb_2O_3/RGO anode. Reproduced with permission.[35] Copyright 2016, Elsevier. d) Schematic reaction mechansims of alloying, conversion and conversion-alloying.

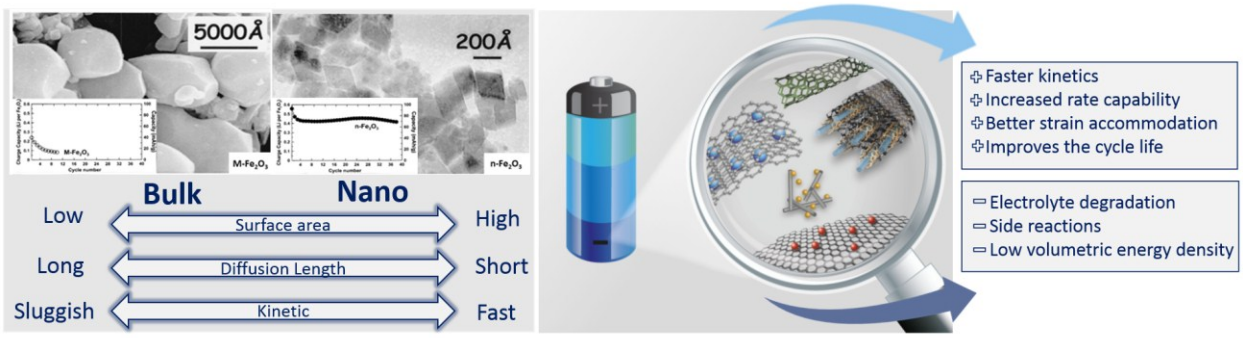

Figure 3. Comparison of nano-Fe_2O_3 and micro-Fe_2O_3 hematite samples with corresponding cycling behavior. Reproduced with permission.[50] Copyright 2003, The Electrochemical Society. Schematic summary of properties of nanostructures for application as anodes in sodium-ion batteries with related advantages and disadvantages.

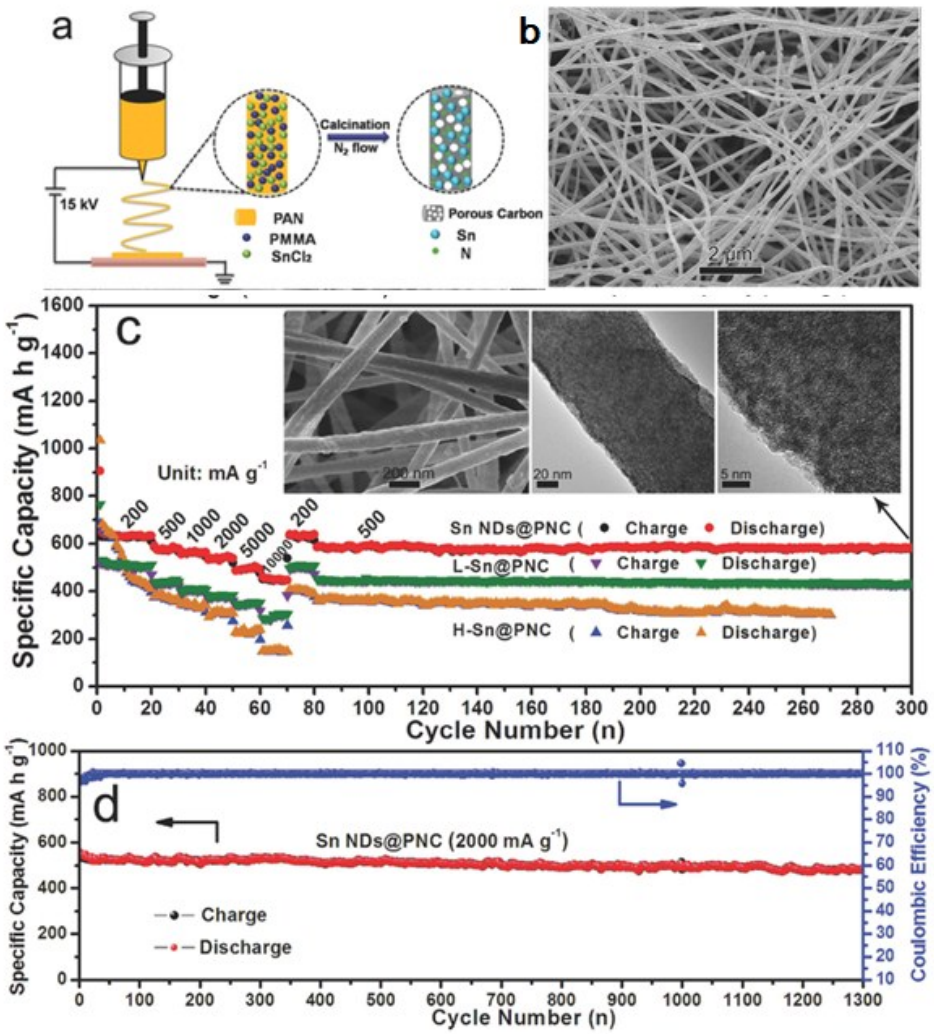

Figure 4. a) Schematic illustration of the preparation process for Sn NDs@PNC nanofibers. b) SEM images of Sn NDs@PNC nanofibers. c) Rate capability of Sn NDs@PNC, lower Sn content (L-Sn@PNC), and higher Sn content (H-Sn@PNC) electrodes, inset: SEM, TEM, and HRTEM images of Sn NDs@PNC after 300 cycles. d) Long-term cycling stability of Sn NDs@PNC electrode at a current density of 2000 mA g^{-1}. Reproduced with permission.[33] Copyright 2015, Wiley-VCH.

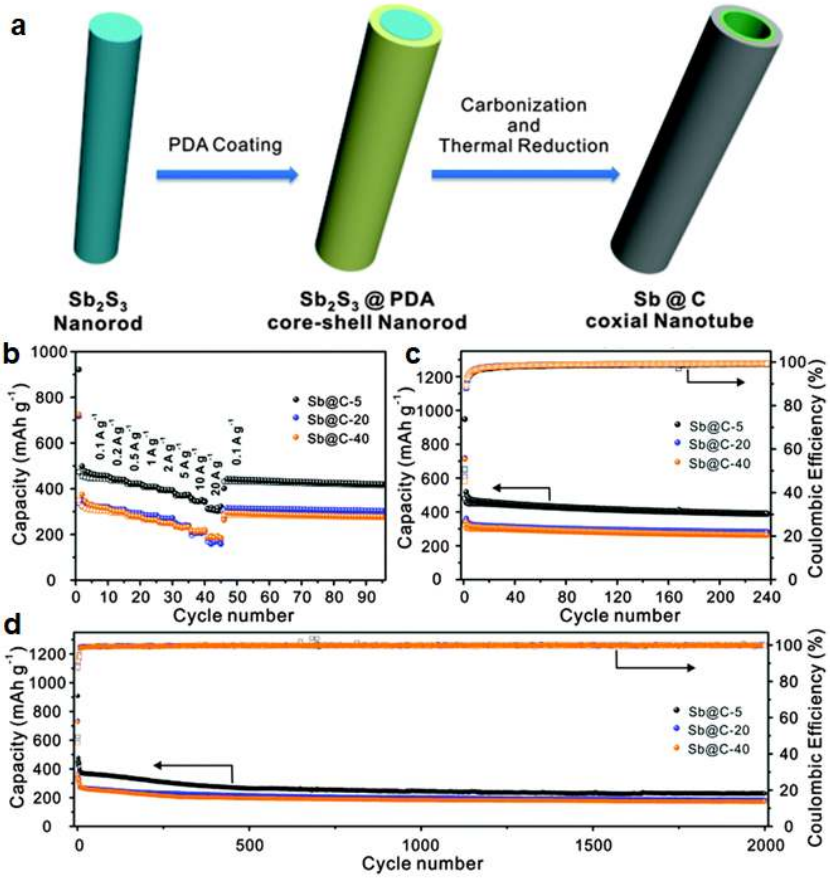

Figure 5. a) Schematic illustration of the formation of Sb@C coaxial nanotubes. b) Rate performance of Sb@C-5, Sb@C-20, and Sb@C-40 at various current densities from 100 mA g^{-1} to 20 A g^{-1}, c, d) cycling performance of Sb@C-5, Sb@C-20, and Sb@C-40 at a current density of 100 mA g^{-1} and 1.0 A g^{-1}, respectively, and the corresponding Coulombic efficiency. Reproduced with permission.[94] Copyright 2016, Royal Society of Chemistry.

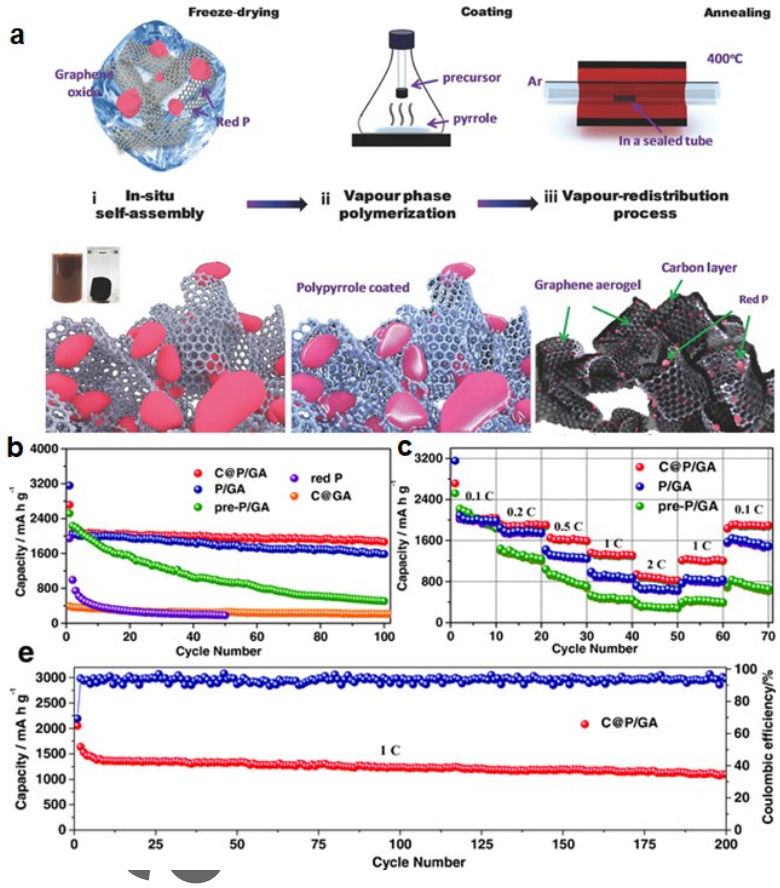

Figure 6. a) Schematic illustration of the synthesis process for C@P/GA composite in three steps. (i) An in situ self-assembly process to obtain the 3D porous graphene-hydrogel-encapsulated red P precursor. (ii) Vapor phase deposition of polypyrrole on the precursor in a chamber. (iii) Vapor-redistribution of red P by annealing the precursor in pure argon atmosphere to obtain the C@P/GA composite. b) Cycling performance of pre-P/GA, P/GA, C@P/GA, red P, and C@GA composites at 0.1 C. c) Rate performance of pre-P/GA, P/GA, and C@P/GA composites at different current densities. d) Cycling performance of C@P/GA composite at 1 C (1 C = 2600 mA g^{-1}). Reproduced with permission.[113] Copyright 2016, Wiley-VCH.

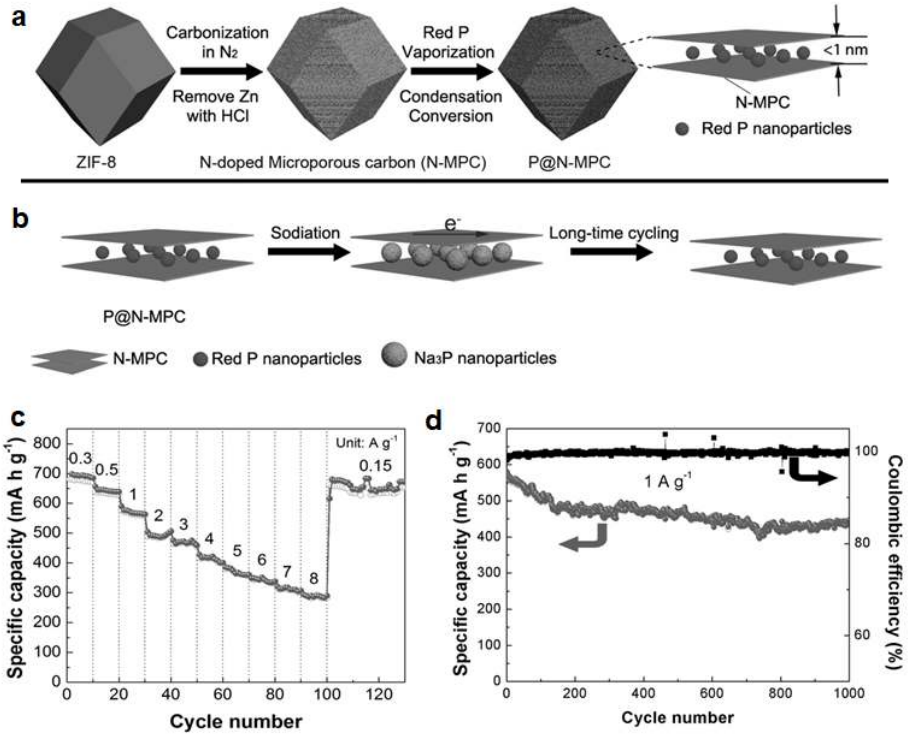

Figure 7. a) Schematic illustration of the preparation process for P@N-MPC. b) Sodiation process of P@N-MPC. c) Capacity of P@N-MPC composite as a function of cycling rate (0.3–8 A g^{-1}). d) Cycling test of P@N-MPC electrodes at 1 A g^{-1} with activation first at low current density. The capacities and current densities here are calculated based on the mass of the P@N-MPC composite. Reproduced with permission.[119] Copyright 2017, Wiley-VCH.

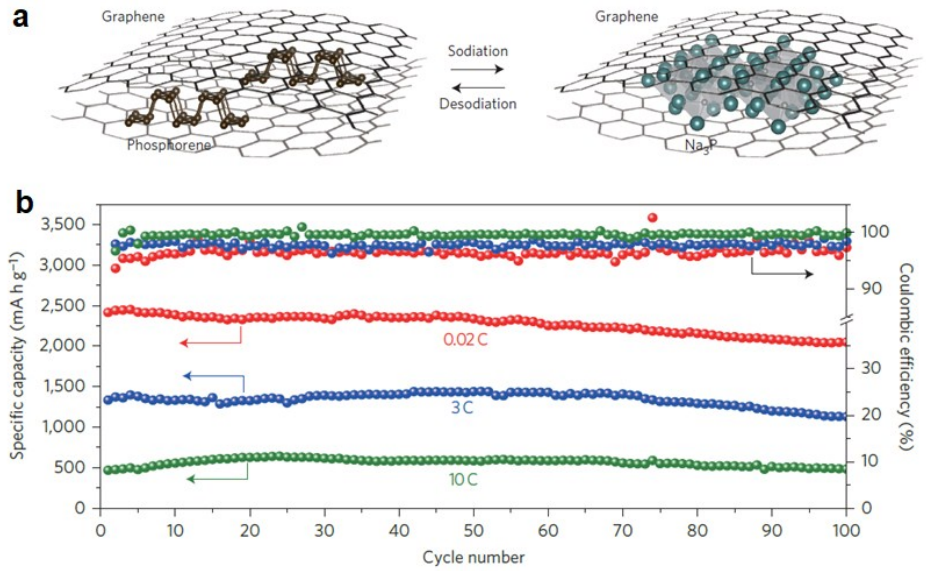

Figure 8. a) Structural evolution of the sandwiched phosphorene–graphene structure during sodiation. b) Reversible desodiation capacity and Coulombic efficiency for the first 100 galvanostatic cycles of the phosphorene/graphene (48.3 wt% P) anode tested under different currents. Reproduced with permission.[131] Copyright 2015, Macmillan Publishers Limited.

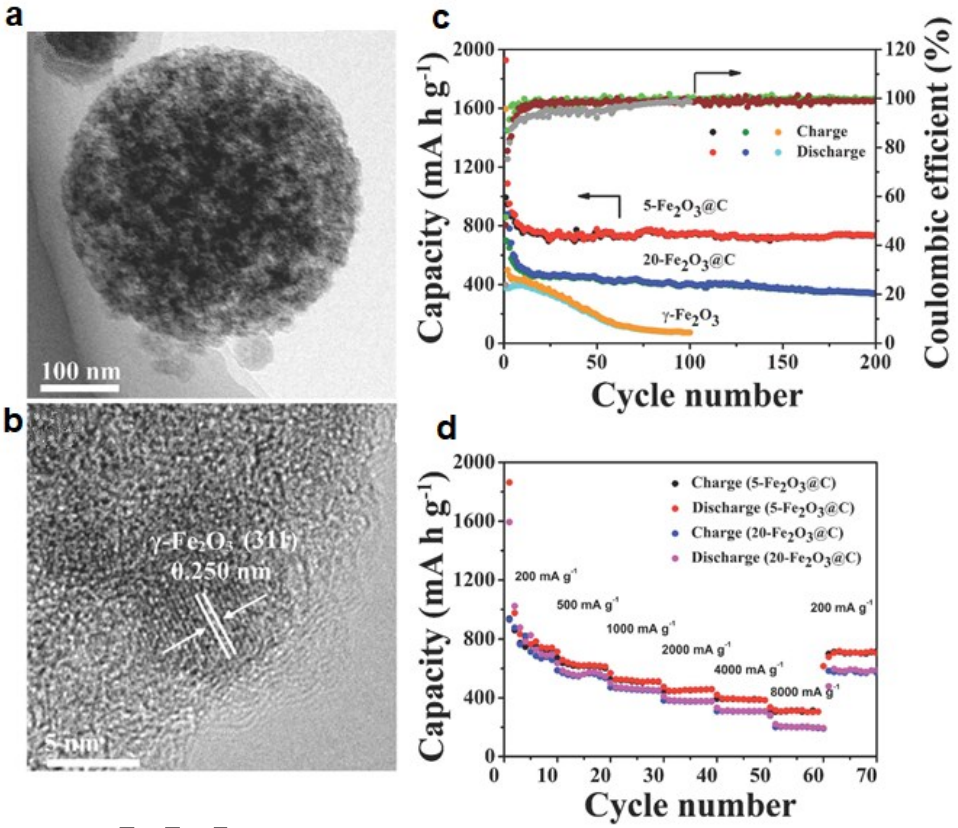

Figure 9. a) TEM and b) HRTEM images of 5- Fe_2O_3@C. c) Cycling performance of 5-Fe_2O_3@C, 20-Fe_2O_3@C, and γ-Fe_2O_3 composites at a current density of 200 mA g^{-1}. d) Rate capability of 5-Fe_2O_3@C and 20-Fe_2O_3@C at different current densities. Reproduced with permission.[185] Copyright 2014, Wiley-VCH.

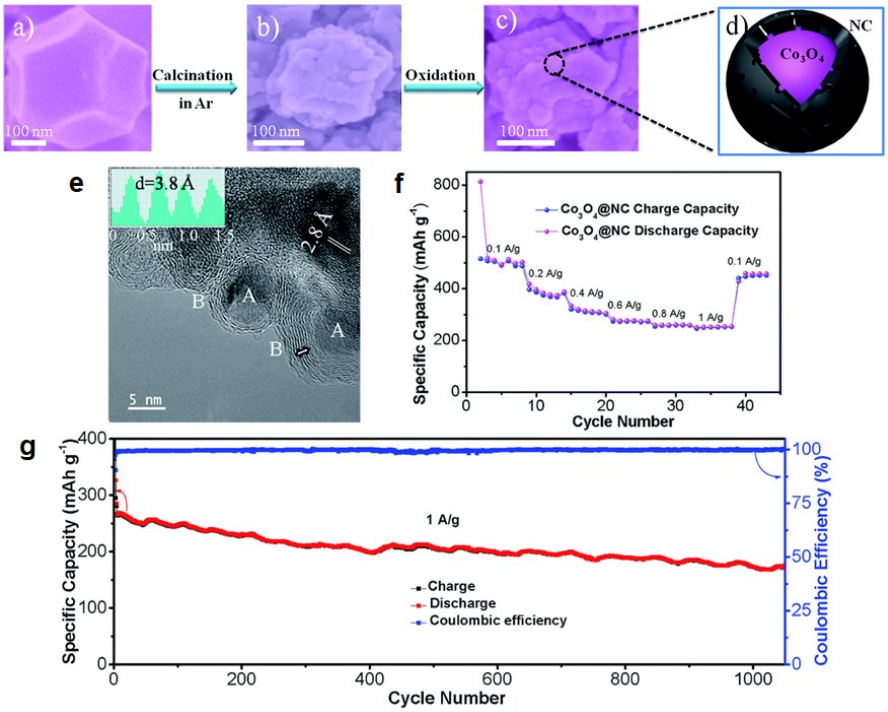

Figure 10. Illustration of the formation of Co_3O_4@NC. Scanning electron microscope (SEM) images of a) ZIF-67 precursor, b) Co@NC intermediate, and c) Co_3O_4@NC. The subunit composition, consisting of a Co_3O_4 core and a NC shell, is illustrated in d). e) TEM images of Co_3O_4@NC at different magnifications. A and B in (f) represent the Co_3O_4 core and the NC shell, respectively. f) Rate capability and g) long-term cycling stability of Co_3O_4@NC electrode. Reproduced with permission.[196] Copyright 2016, Royal Society of Chemistry.

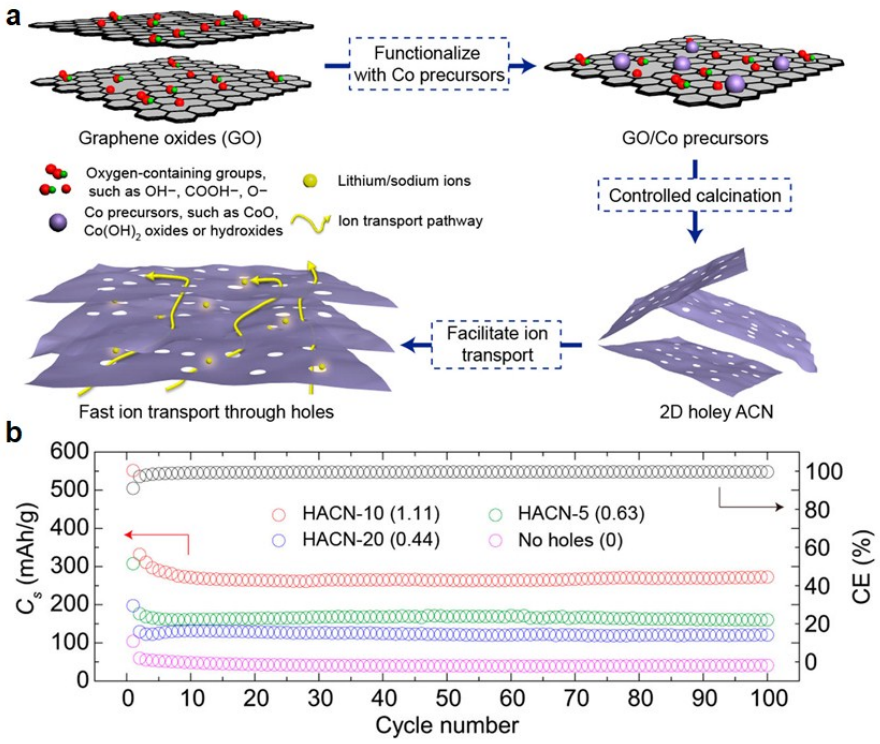

Figure 11. a) Schematic illustration of the formation of 2D holey Co_3O_4 nanosheets and their advantages for ion transport. b) Cycling performance of the holey Co_3O_4 with different pores at 0.8 A g^{-1}. Reproduced with permission.[207] Copyright 2017, American Chemical Society.

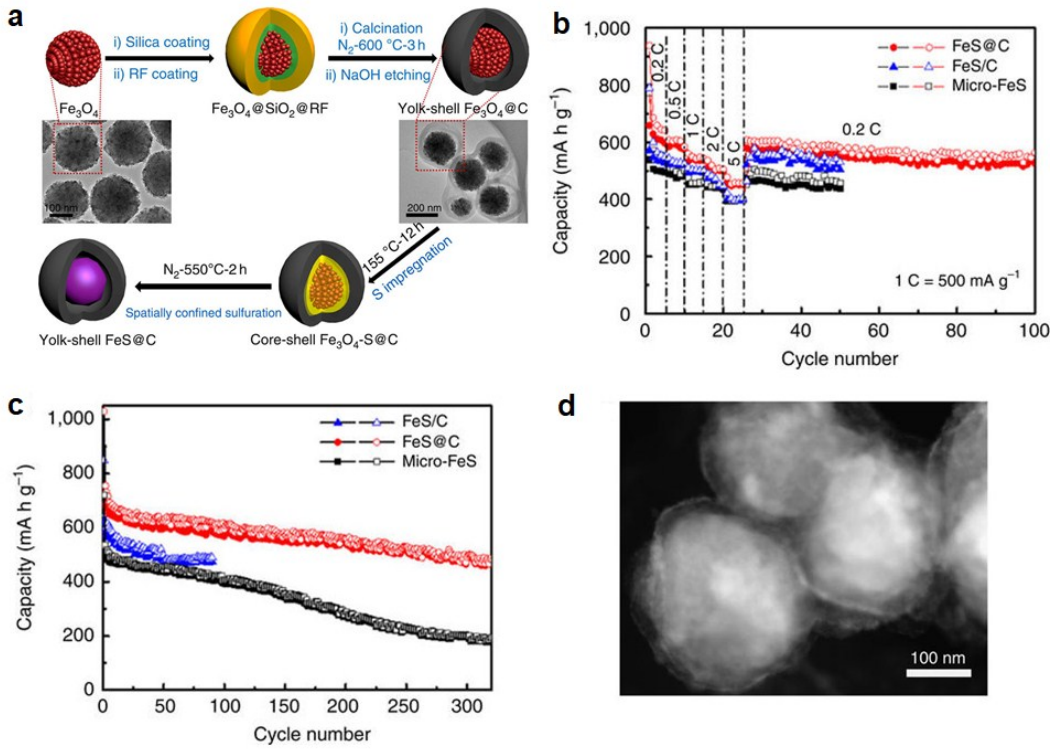

Figure 12. a) Schematic illustration of the synthesis of yolk-shell FeS@C. b) Rate capability at various current rates and c) cycling performances at 0.2 C (100 mA g^{-1}) of the micro-FeS, core-shell FeS/C nanospheres and yolk-shell FeS@C nanospheres. d) Scanning TEM image of the yolk-shell FeS@C electrode after 50 cycles at the current rate of 0.2 C. Reproduced with permission.[219] Copyright 2015, Macmillan Publishers Limited.

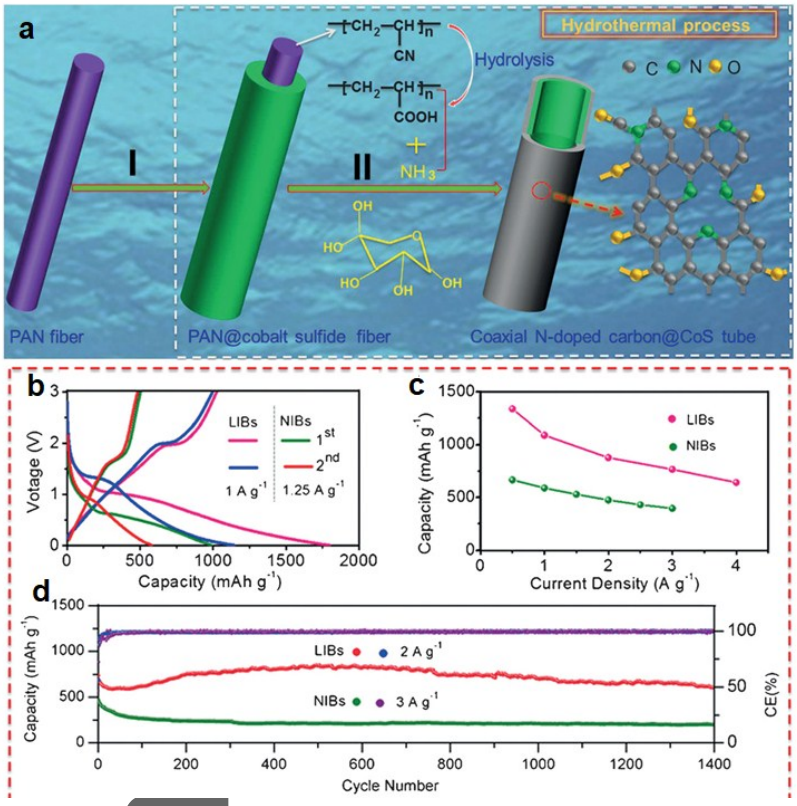

Figure 13. a) Schematic illustration of the synthesis of the N-doped carbon@CoS coaxial nanotubes. b) Charge–discharge profiles; LIBs=lithium-ion batteries, NIBs=sodium ion batteries. c) Rate capability and d) cycling performance of the N-doped carbon@CoS coaxial nanotubes. Reproduced with permission.[233] Copyright 2017, Wiley-VCH.

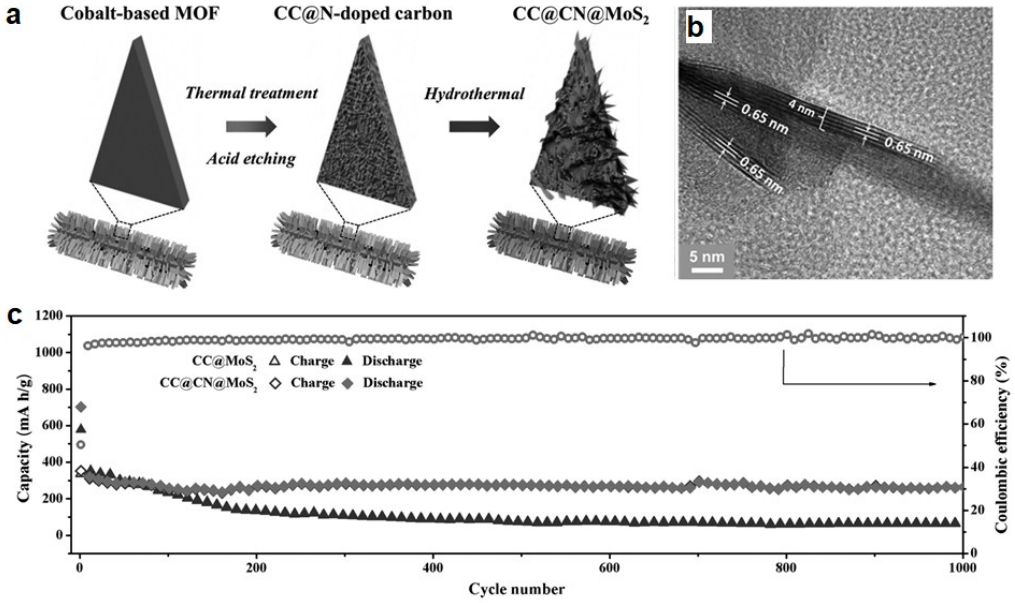

Figure 14. a) Schematic illustration of synthesis of the CC@CN@MoS_2 arrays. b) HR-TEM images of the CC@CN@MoS_2. c) Cycling performances at 1 A g^{-1} for the CC@CN@MoS_2 and CC@MoS_2. Reproduced with permission.[256] Copyright 2017, Wiley-VCH.

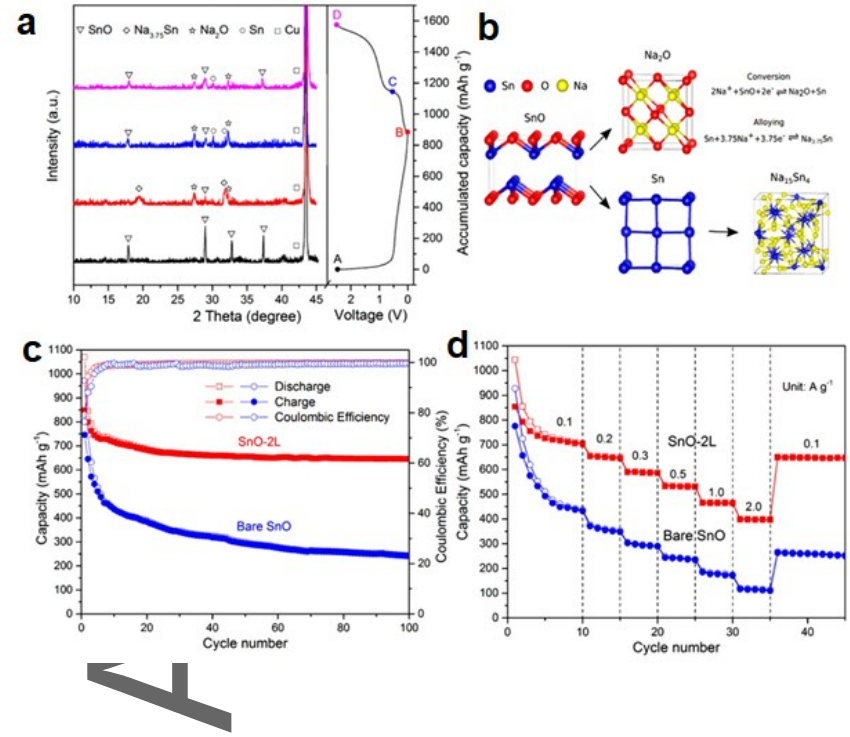

Figure 15. a) Ex situ XRD profiles of bare SnO electrode over the first charge−discharge cycle. b) Schematic illustration of the reaction mechanism during the sodiation process. c) Cycling performances of bare SnO and SnO-2L electrodes at 0.1 A g^{-1} for 100 cycles. d) Rate capabilities of bare SnO and SnO-2L electrodes. Reproduced with permission.[303] Copyright 2017, American Chemical Society.

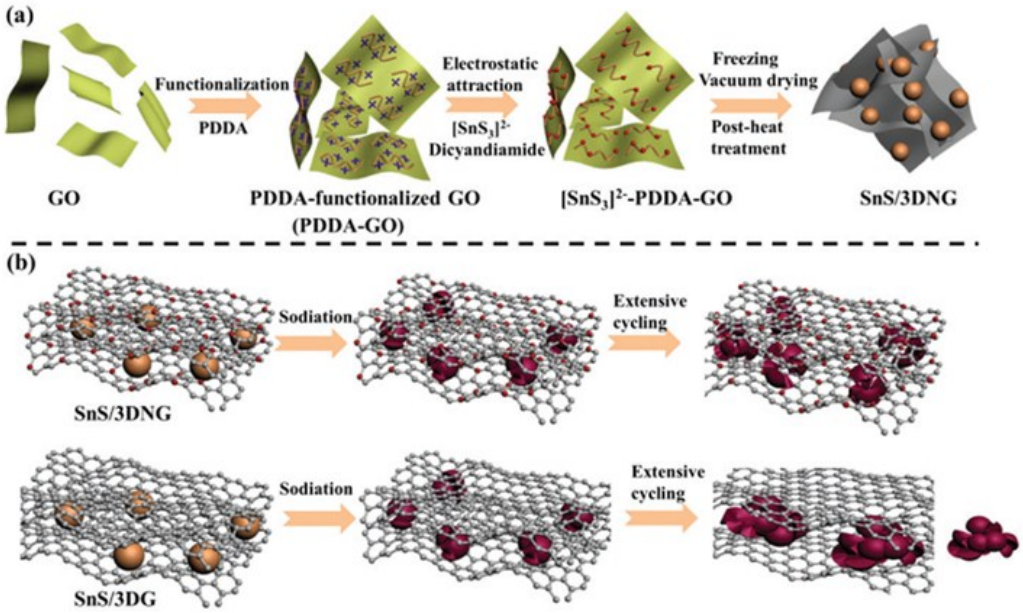

Figure 16. a) Schematic illustration of the fabrication process of SnS/3DNG. b) The sodiation process in SnS/3DNG and SnS/3DG, respectively. Reproduced with permission.[312] Copyright 2017, Royal Society of Chemistry.

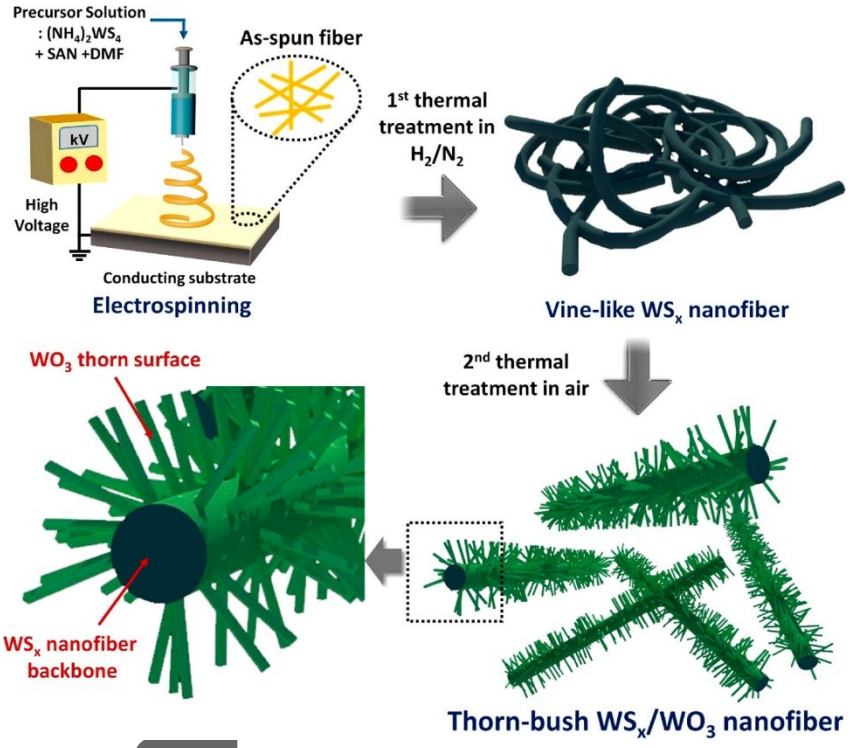

Figure 17. Schematic illustration of the synthetic strategy used to create the heterogeneous WS_x/WO_3 thorn-bush nanofibers. Reproduced with permission.[319] Copyright 2016, American Chemical Society.

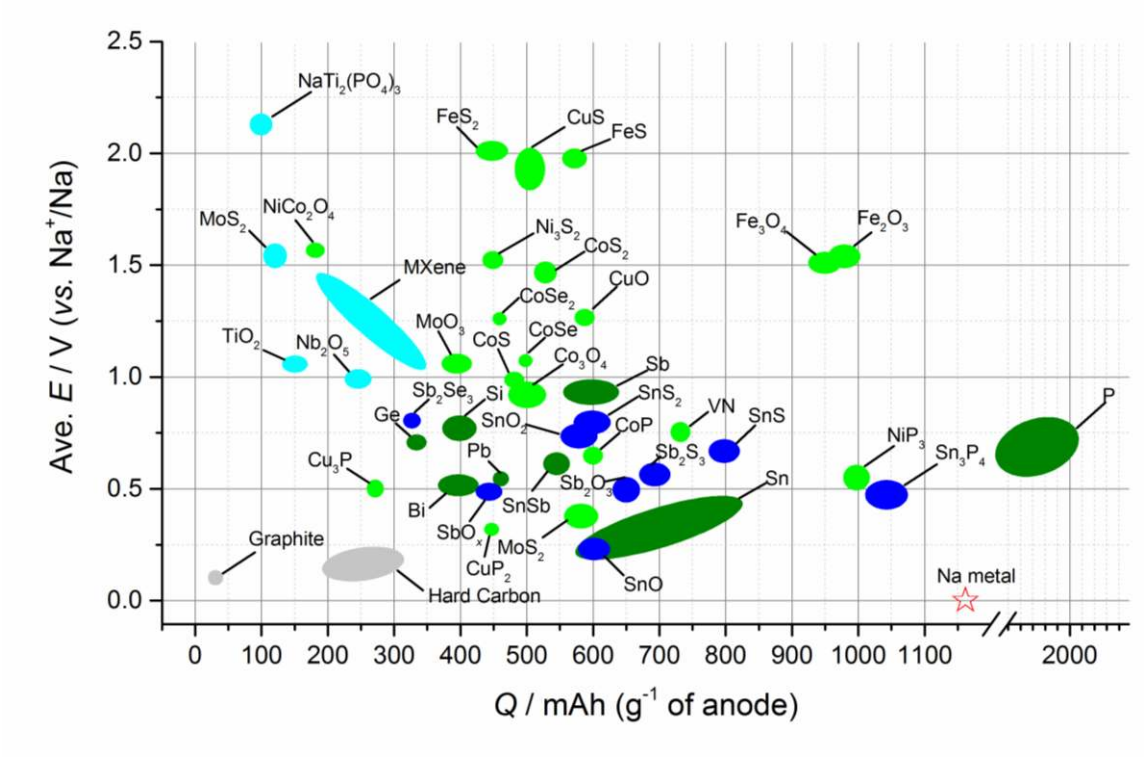

Figure 18. Average working potential versus gravimetric capacity for various negative electrode materials for NIBs; (cyan) typical intercalation anode materials, (grey) graphite and hard carbon materials, (olive) alloying anode materials, (green) conversion-based anode materials, and (blue) conversion-alloying materials. The gravimetric capacity is calculated in Na half cells according to the reports.

Table 1. Summary of nanostructured alloy-based anodes for SIBs.

Materials	Synthesis	Mass Loading total electrode / mg cm^{-2}	Active material % w in material	Electrode composition /%	Electrolyte	Potential range / V vs Na^+/Na	Current density / mA g^{-1}	1st sodiation capacity / mAh g^{-1}	1st cycle irreversibility / %	Number of cycles	Capacity retention after (x) cycles/ %	Coulombic Efficiency after (x) cycles / %	Ref.
Sn/graphite	High energy mechanical milling	--	30	AM:SP:PVdF 80:10:10	1 M $NaClO_4$ EC:DMC (1:2v)	0.01-1.2	50	584	30	20	86	~98	[157]
Mesoporous Sn/C	Carbothermal of SnO_2 in polymer matrix	0.5	66	AM:CB:CMC 70:15:15	1 M $NaClO_4$ EC:DMC (1:2v	0.02-1.5	20	750	61	15	~67	--	[54]

)

Sn/C	Carbothermal of acetate precursors	1.7 – 2.0	33	AM: SC:CMC 75:20:5	0.5 M $NaPF_6$ PC+ 2%v FEC	0.01-1.25 0.025-1.25	12.2 12.2	565 --	57 --	20 130	~77 ~87	97 99	[158]
Sn/C/Ni nanoforests	PVD, magnetron sputtering electroless deposition	~0.5	--	AM: 100	1 M $NaClO_4$ EC: DEC (1:1v)	0.05-1.5	50	~920	20	150	55	97	[74]
Al_2O_3/SnNPs@CNF	Electrospinning, carbonization and ALD coating	--	26	AM: 100	1 M $NaPF_6$ in EC: DEC (1:1, m/m)	0.02-1.5	84.7	~1000	40	40	100	~98	[159]
Sn@CNT	Freeze-drying	1.2	40.7	AM: 100	1 M NaCl	0.01-	50 μA	1085	18	100	~97	97	[75]

nanopillars	and CVD				$LiClO_4$ EC:PC (1:1v) + 5%v FEC	2.6	cm^{-2}	µAh cm^{-2}					
Sn-polyacrilate	Mechanochemical synthesis	--	80	AM:AB:PPA 80:10:10	1 M $NaClO_4$ PC +2%v FEC	0.0-1.5 0.0-0.8	50 50	650 590	15 20	10 20	-- --	~50 >100	[58]
Sn NPs/ wood fibers	Electrodeposition	--	--	AM: 100	1 M $NaPF_6$ EC:DEC (1:1 v)	0.0-1.5	84	--	~77	400	~42	~72	[79]
Ultrasmall Sn NPs in carbon	Aerosol spray pyrolysis technique	1.5–2.0	46	AM:SP:CMC 70:15:15	1 M $NaClO_4$ EC:DEC (1:1v)	0.01-2.0	200 1000	736	33	200 after rate cap.	-100 ~100	-100 ~100	[78]

Yolk−shell Sn@C	Solvothermal and carbothermal	1.2−1.5	--	AM:SP:PAA 80:10:10	1 M $NaClO_4$ EC:DEC (1:1v)+ 1% FEC	0.02-2.0	100 200	980 ~800	-- --	50; 1000	~44 ~40	-100 ~100	[77]
Sn@N-CNFs	Electrospinning technique	--	46	AM:100	1 M $NaClO_4$ EC:PC (1:1v) +5% FEC	0.02.5	84.7 847	1560	44 --	200 1000	-80 ~100	-100 ~100	[76]
Sn@rGO@GO	Flash reduction and Sn electrophoretic deposition	3.9 (Sn loading)	90	AM:100	1M $NaClO_4$ EC:DEC (3:7v)	0.01-2.0	0.5 C	1000	39	100	-64	-100	[72]
Sn NDs@PNC	Electrospinning technique followe	1.5	63	AM:100	1 M $NaClO_4$ PC +5%	0.01-2.0	200 2000	905.4	30	20 +Rate Cap	100 -10	~100 -100	[33]

	d by a heat treatment				FEC					1300	0		
$Sn_{50}Ge_{25}Sb_{25}$ alloy	Dc Magnetron Sputtering	--	50 % Sn 25 % Ge 25 % Bi	AM: 100	1 M $NaClO_4$ EC/ DEC (1:1 v)	0.01-2.0	85	~110	25	50	84	~93	[62]
$Sn_{10}Bi_{10}Sb_{80}$ alloy	Co-sputtering	0.05 mg	10 % Sn 10 % Bi 80 % Sb	AM: 100	1 M $NaClO_4$ EC/ DEC, 1:1 v/v + 5wt % FEC	0.01-2.0	--	830	~30	100	>100	~97	[63]
SnSb/CNF	Electrospinning	1.5-2.0 mg	60	AM: SC:CMC 80:10	1 M $NaPF_6$ EC/ DEC, 1:1	0.0001-2.0	0.2 C	654	47	200	~100	96-97 %	[71]

				:10	v/v + 5wt % FEC								
Spherical nano-Sb@C	Aerosol spray pyrolysis method	-0.8 1.2 1.6	68.8	AM:SP:CMC 80:10:10	1 M $NaClO_4$ (PC +5% FEC)	0.01-2.0	100	657	36.5	500	88.5	-100	[93]
Hexagonal/amorphous Sb	Electrochemically cathodic corrosion	-1.5	100	AM:SP:CMC 70:15:15	1 M $NaClO_4$ (PC +5% FEC)	0.01-2.0	100	H Sb-800 A Sb-840	H-25 A-26	50	-100	> 98.5	[160]
Cypress Leaf-Like Sb	Chemical replacement reaction	--	--	AM:SP:CMC 70:15:15	1 M $NaClO_4$ (PC +5% FEC)	0.01-2.0	100 660	916.5 ~800	-30 ~30	120 120	-99 ~99	-100 -100	[161]
Nano Sb/C	Infiltration and calcination	2.48	30	AM:SP:PVdF 80:10:10	1 M $NaClO_4$ PC:F	0.01-2.0	50	375	44	50	-90	99	[38]

					EC (8:2 w)								
Sb-C nanocomposites	Magneto ball milling	1.2 - 1.5	80	AM: SP:CMC 80:10:10	1 M $NaClO_4$ PC +2% FEC	0.01-2.0	100	650	20	150	~75	--	[162]
Ultrafinel Sb/C	Hydrothermal synthesis followed by a thermal reduction	0.25	56.6	AM: SP:SA 70:20:10	1 M $NaClO_4$ EC: DEC (1:1 v) + 5%w FEC	0.01-2.5	100	1031	33.6	110	91	97	[163]
Sb@S,N-3D macroporous carbon	Carbonization route using silica opals template	1.0	56	AM: SP:PVdF 80:10:10	1 M $NaPF_6$ EC: DEC (1:1v) + 5%w FEC	0.001 - 2.0	100	1074	55.1	500	93	- 100	[164]
3D	Electrod	0.6	87	AM:	1 M	0.0	66	61	24	10	98	99	[1

Sb/Sb_2O_3 @PPy	epositio n method	7		100	NaCl O_4 PC +2% FEC)	1-1.5		1		0			65]
Sb/CNFs	Wet preparat ion+ carboni zation	--	80.8	AM: SP:C MC 70:15 :15	1 M NaCl O_4 PC +5% FEC	0.01-2.0	100	794.6	30	100	--	96.7	[166]
Sb/C/graphene	Electros pinning/ spray process	--	15	AM 100%	1 M NaCl O_4 EC: DMC (1:1 v)	0.01-2.0	100	892	38	100	98	80	[97]
Self-wrapped Sb/C	Freeze-drying self-wrappin g method	2.0	41	AM: SP:C MC 80:5: 15	1 M NaCl O_4 EC:P C (1:1 v) + 5%w FEC	0.01-2.0	500	558	28	100	--	94	[167]
Sb Nanocry	Spray pyrolysi	--	46	AM: CB:C	1 M NaCl	0.001-	300	62	36	10	--	92.	[9

stals/carbon microspheres	s process			MC 70:20:10	O_4 EC: DMC (1:1 v) + 5%w FEC	2.0		5		0		5	2]
Nanocomposite Sb/C	Mechanical milling	3.0	--	AM: SP:CMC 80:10:10	1 M $NaPF_6$ EC: DEC + 5% FEC	0.01-2.0	100	717	15	80 100 (FEC)	0 94(FEC)	--	[81]
Sb/N-C-CNT	Ball-milling	1.0−1.2	64	AM: SP:CMC 70:20:10	1 M $NaClO_4$ EC: DEC :FEC (1:1:0.1v)	0.01-2.0	100	837	35	200	97.2	87	[95]
Sb/Multilayer Graphene Hybrid	Confined vapor deposition method	1.0−1.5	40	AM: SP:CMC 80:10:10	1 M $NaClO_4$ EC: DEC FEC (1:1:	0.01-2.0	100	593	23	200	99	89	[101]

					0.1v)								
β-Zn_4Sb_3 nanowires	Chemical vapor deposition	1.0	--	AM:SP:PVdF 70:15:15	1 M $NaClO_4$ PC +5% v FEC	0.01-2.0	207 414	675 700	42 50	-- 200	-- 99	-- ~100	[89]
RP/C	Mechanical ball milling	2.0-3.0	70	AM:SP:PAA 70:10:20	0.8 M $NaClO_4$ EC:DEC (1:1v)	0.0-1.5	143	~2250	15	30	~95	>98	[109]
RP/CNT	Hand grinding	--	70	AM:SP:PAA 70:10:20	1 M $NaClO_4$ EC:DEC (1:1v) + 5%w FEC	0.0-1.5	143	2210	30	10	76	--	[110]
P-CNT-crosslinked polymer	Mechanical ball milling	0.8-1.0	70	AM:CA:CMC-CA	1 M $NaClO_4$ EC:DEC	0.01-2.0	260 (1^{st} cycle)	2100	19	100	91	~99	[112]

hybrid				70:15:15	(1:1v) + 10% v FEC		520 after activation						
C@RP@Graphene Aerogel	Advanced Vapor-Redistribution	--	47	AM:SP:CMC 70:20:10	1 M $NaClO_4$ EC:DEC (1:1v) + 10% v FEC	0.01-2.0	260	~2700	17	100	80	~99	[113]
P/graphene scrolls	Quick-freezing process	2.0-2.5	52.2	AM:CB:PVdF 80:10:10	1 M $NaClO_4$ EC:DEC + 5% v FEC	0.0-2.0	250	2939	20	150	92.3	--	[114]
RP/SWCNT	Vaporization-condensation method	0.7-1.2	40	AM:CB:PVdF 85:5:15	1 M $NaClO_4$ FEC:DMC	0.01-2.0 0.001-2.0	50 2000	980	34 --	50 2000	>100 80	99 ~100	[115]

					(1:1 v)								
Amorphous RP@N-Microporous Carbon	Carbonization of ZIF-8 Red P encapsulated by vaporization–condensation–conversion method	1.1 - 1.5	22.6	AM: AB:PVdF 80:10:10	1 M $NaClO_4$ in EC: DMC (1:1 v)	0.01-2.0	1500 1000	1321	46	100 1000	84 80	100 100	[119]

Table 2. Summary of nanostructured conversion-based anodes for SIBs

Materials	Synthesis	Mass Loading total electrode / mg cm^{-2}	Active material % w in material	Electrode composition /%	Electrolyte	Potential range / V	Current density / mA g^{-1}	1st sodiation capacity / mAh g^{-1}	1st cycle irreversibility / %	Number of cycles	Capacity retention after (x) cycles/ %	Coulombic Efficiency after (x) cycles / %	Ref.

Fe_3O_4 nanoparticles	Hydrothermal reaction	0.97	100	AM:SP: SA 70:20:10	1 M $NaClO_4$ PC	0.01-3.0	83	~720	55	50	75	~98	[190]
3D-0D Graphene-Fe_3O_4 Quantum Dot Hybrids	Hydrothermal process	~0.9	50	AM:SP: SA 80:10:10	1 M $NaClO_4$ EC:DEC (1:1 v)	0.001-3.0	30 50 500	779 659 ~430	32 33 ~35	10 200 200	83 71 80	~98 99.7 ~100	[191]
3D Porous γ-Fe_2O_3@C	Template-free aerosol spray pyrolysis	1.0	60	AM:SP: PVdF 70:20:10	1 M $NaClO_4$ EC:DEC (1:1 v)	0.04-3.0	200	1927	48.5	200	74	~100	[185]
Ordered Dual Porosity Mesoporous Co_3O_4	Template synthesis	~1.0	100	AM:SP: CMC-PA 70:20:10	1 M $NaClO_4$ EC:PC (1:1 v)+ 5% w FEC	0.01-2.5	90	~700	~29	100	~59	~100	[200]

Porous Hollow Co_3O_4/N-C	MOF via solvothermal reaction followed by annealing step	1.5	97.5	AM:CB:SA 60:20:20	1 M $NaClO_4$ PC + 5%v FEC	0.01-3.0	100 500	712 ~600	34 ~33	50 50	~74 ~73	~97 97-99	[203]
2D holey Co_3O_4 Nanosheets	Template-directed synthesis	~1.0	--	AM:CB:CMC 80:10:10	1 M $NaClO_4$ PC + 2% FEC	0.01-3.0	400	553	45	100	~90	~98	[197]
Porous CuO nanowires	Precipitation method	--	100	AM:SP:CMC 70:20:10	1 M $NaCF_3SO_3$ DEGDME	0.01-3.0	500 500	640 420	16 10	50 50	~57 ~63	~100 ~100	[209]
CuO Nanorod Arrays	In-situ engraving commercial	2.0	100	AM:100	1 M $NaPF_6$ EC:DMC +	0.0-3.0	20 50 200	935 ~990 ~72	29 41 12	10 30 450	>100 ~100	~100 ~100	[210]

	Cu foil			5% FEC			0			~45	~100	
α-MoO_3	Wet chemistry and precipitation	1.5-1.7	100	AM:SP:PVdF 75:15:10	1 M $NaPF_6$ EC:PC	0.04-3.0	11 1.7	~773	47	20	~55	~99	[175]
Yolk-shell FeS@C (reported a cathode)	Spatially confined sulfuration	1.5-2.0	83	AM:CB:PVdF 80:10:10	1 M $NaClO_4$ EC:PC (1:1 v)+ 5% w FEC	0.01-2.3	100	1029	30	300	67.6	~100	[219]
FeS_2@C yolk-shell nanoboxes	Etching method coupled with a novel sulfidation-in-nanobox strate	1.2	85.5	AM:CB:PVdF 70:20:10	1 M $NaCF_3SO_3$ DEGDME + 5% FEC	0.1-2.0	100 2000	957 --	38 --	100 800	~87 ~66	~100 ~100	[227]

	gy												
FeS_2 nanocrystals (reported as cathode)	Solution-phase chemical synthesis	0.5	100	AM:CB:CMC 64:21:15	1 M $NaClO_4$ PC + 10% FEC	0.02-2.5	1000	~1250	32	600	~50	~99	[226]
MoS_2 Nanoflowers	Hydrothermal method	--	100	AM:KS-6:CMC 80:10:10	1 M $NaCF_3SO_3$ DEGDME	0.4-3.0	200	243	10	300	>100	~100	[254]
MoS_2/Graphene	Hydrothermal method	1.0	44.2	AM:CB:PVdF 70:20:10	1 M $NaClO_4$ EC:PC (1:1 v)	0.01-3.0	20	~1150	30	100	~60	--	[34]
WS_2@CMK-3	Hydrothermal method	1.0	65	AM:SP:SBR-CMC 70:20:10	1 M $NaClO_4$ EC:PC (1:1 v)+ 5% FEC	0.01-3.0	100	477	40	70	>100	~97	[261]
VS_2	Solvo	1.0	10	AM:S	1 M	--	10	790	14	10	100	100	[2

Nanosheet	thermal reaction	0	P:CMC 60:20:20	$NaClO_4$ EC:DEC (1:1 v)+ 6%v FEC	0 10 00	~550	0 20 0	>100	100	[62]

Table 3. Summary of nanostructured conversion-alloying anodes for SIBs.

Materials	Synthesis	Mass Loading total electrode/mg cm^{-2}	Active material % w in material	Electrode composition /%	Electrolyte	Potential range/V	Current density /mA g^{-1}	1st sodiation capacity/ mAh g^{-1}	1st cycle irreversibility/%	Number of cycles	Capacity retention after (x) cycles/ %	Coulombic Efficiency after (x) cycles / %	Ref.
SnO_2-RGO	Hydrothermal method	--	76.4	AM:SP:CMC-PAA 80:10	1 M $NaClO_4$ EC:PC	0.005-2.5	100	~1230	~67	150	81	~100	[297]

				:10	(1:1 w) + 5%w FEC								
Sandwiched C@SnO_2@C hollow nanostructures	Template synthesis, calcination and CVD	0.8 - 1.2	54	AM: CB: PVdF 70:15 :15	1 M $NaClO_4$ EC: DEC (1:1v)	0.005-2.5	100 460 0	~1200 ~780	~44 ~50	35 300 0	~65 ~50	~100 >99.5	[298]
Amorphous SnO_2/graphene aerogel	Hydrothermal method	0.44	50.7	AM: CB:PVdF 70:20 :10	1 M $NaClO_4$ EC:PC (2:1v) +10 %v FEC	0.01-3.0	50	541.6	54	100	~80	--	[299]
Amorphous SnO_2/C/CNT	$SnCl_2$ solution-based	--	72	AM: SP:CMC 60:20 :20	1 M $NaClO_4$ EC:PC (1:1v	0.005-3.0	100 1600	1106 ~1100	43 45	100 300	~70 ~40	~98 ~98	[300]

	precipitation method			) +5% w FEC									
2D ultrathin SnO@CNT	Hydrothermal method	1.9-5	--	AM:100	1 M $NaPF_6$ EC:DEC:FEC (1:1:0.05v)	0.01-3.0	100 1000	1318	56	600 1000	91 75	~100 ~100	[302]
Few layer SnO@carbon cloth	Hydrothermal method	0.9	--	AM:100	1 M $NaClO_4$ EC:DMC (1:1 w)	0.005-2.5	100 1000(after 10 cycle at 100)	1072 492(after 10 cycle at 100)	21	100 1000	78 ~92	~100 ~100	[303]
SnO Microflowers	Ultrafast Ionic Liquid-Assisted Micr	1.2-1.4	100	AM:CB:CMC 70:20:10	1 M $NaPF_6$ EC:PC (1:1 w)+ 2%w	0.005-2.0	25 (activation) 100	~1070 ~440 (after activation)	53 --	3 (activation) 50	>100 >100	93.3 ~98	[304]

	owave synthesis				FEC								
Layered SnS_2-RGO	Hydrothermal route	0.8-1.0	--	AM:AB:CMC 80:10:10	1 M $NaClO_4$ EC:DEC (1:1v)	0.01-2.5	100 1000	839 594(after activation 5 cycles at 200)	25 --	100 400	~100 ~84	>99 >99	[306]
SnS_2 nanocrystals on amino-functionalized RGO	Freeze-drying method	~1.0	75	AM:CB:CMC 80:10:10	1 M $NaClO_4$ EC:DEC +5% w FEC	0.01-3.0	200 1000(after 5 cycle at 200)	1025 ~560 (after 5 cycle at 200)	27 --	100 1000	~91 ~85	~100 ~100	[307]
SnS@C	High-energy mechanical milli	2.0	--	AM:SP:PAA 70:20:10	1 M $NaPF_6$ EC:DEC (1:1v)	0.01-2.0	100	~730	35	80	~100	~100	[309]

	ng												
3D Porous SnS/C	Electrostatic spray deposition technique	0.6 - 0.8	69	AM:100	1 M $NaClO_4$ PC +5% FEC	0.01-3.0	100 1000	523 --	21 --	3 300	~100 80	~100 ~100	[310]
SnS/acid-treated MWCNT	Colloidal synthetic route	2.2	60.3	AM:100	1 M $NaPF_6$ DEGDME	0.01-2.7	300	~1300	10	50	~80	>99	[311]
SnS@3D N-graphene	Wet-chemical and freeze-drying process	1.1 - 1.3 g cm^{-3}	92	AM:SP:CMC 70:15:15	1 M $NaClO_4$ PC +5% FEC	0.01-2.5	100 2000	~1100 ~620	20 5	10 1000	100 87	~99 ~99	[312]
Sb_2O_3/RGO	Microwave-assisted	--	39	AM:AB:CMC 70:20	1 M $NaClO_4$ EC:PC	0.005-3.0	100	854.6	48	50	>100	97.6	[35]

	synthesis		:10	(1:1 w) +5% w FEC								
Carbon-coated van der Waals stacked Sb_2S_3 nanorods	Hydrothermal method	--	89.5	AM:SP:CMC 70:20:10	1 M $NaClO_4$ PC +5% w FEC	0.0-2.0	100	~1200	~40	100	~71	96	[313]
Sn_4P_3	High-energy mechanical ball milling	--	100	AM:CB:PAA 70:10:20	1 M $NaClO_4$ EC:DEC (1:1v) +5% w FEC	0.0-1.5	100	~880	~23	50	100	~98	[314]
Sn_4P_3/RGO nano	Solvothermal	--	89.6	AM:AB:PVdF	1 M $NaClO_4$	0.01-3.0 100	100	1640 ~160	46 ~43	100 150	~86	~100	[315]

hybrids	route			80:10:10	PC +5% FEC		0	0		0	~52	~100	
Pomegranate-like Sn_4P_3/C nanospheres	Spray-pyrolysis and phosphidation	--	76	AM:CB:SA 70:15:15	1 M $NaPF_6$ DME	0.0-1.5	50 100	~1000 ~890	9.3 --	20 120	~89 ~87	~96 ~100	[316]
Yolk–shell Sn_4P_3@C nanospheres	Top-down phosphidation	1.9	90	AM:CB:PVdF 70:20:10	1 M $NaClO_4$ PC +5% v FEC	0.01-2.0	100 1500	~1804 ~1150	56 52	50 400	65 65	98 ~100	[317]
Yolk–shell Sn_4P_3@C nanocubes	Wet chemistry and hydrothermal route	--	--	AM:AB:PVdF 70:20:10	1 M $NaClO_4$ PC +5% v FEC	0.01-2.0	100 1000	1210 ~1100	~36 ~25	50 500	~91 ~65	~100 ~100	[318]

Table 4. Summary of nanostructured conversion/alloying heterostructures anodes for SIBs.

Materials	Synthesis	Mass Loading total electrode /mg cm^{-2}	Active material % w in material	Electrode composition /%	Electrolyte	Potential range/ V	Current density /mA g^{-1}	1st sodiation capacity/ mAh g^{-1}	1st cycle irreversibility/%	Number of cycles	Capacity retention after (x) cycles/ %	Coulombic Efficiency after (x) cycles / %	Ref.
Double-Walled Sb@TiO$_{2-x}$ Nanotubes	Hydrolysis and calcination	1.0 - 1.5	78 % Sb	AM: AB: CMC 70:20:10	1 M NaClO$_4$ PC +10 %w FEC	0.01- 2.5	2640 660	~700 ~850	~35 ~31	1000 300	~66 ~90	~100 --	[321]
Sb–NiSb–Ni heterostructures	Controlled pulsedelectrodeposition	--	--	AM: 100	1 M NaClO4 PC:FEC	0.01- 1.5	66	1200	~58	300	~61 (of 2nd cycle	~94	[324]

					98:2 v						ca pa cit y)		
SnS/SnO$_2$@RGO heterostructures	Hydrothermal method and sulfidation	1.0	69	AM: SP:CMC-PAA 80:10:10	1 M NaClO$_4$ EC: DEC (1:1v) +5% w FEC	0.01-2.0	30 24 30	976 ~780	~25 ~45	70 50 0	~98 ~76	-- ~100	[32 3]
MoS2/SnS2@rGO nanocomposites	Hydrothermal method	1.3	93	AM: CB: CMC 80:10:10	1 M NaPF6 EC: DEC :DMC (1:1:1v)	0.01-3.0	150 1500	840 --	~19 --	100 150	96 99	~100 ~100	[32 5]
MoS2/Ni3S2@MoS2 coaxial nanofibers	PVP-assisted hydrothermal reaction	~8-10	--	AM: 100	1 M NaPF6 EC: DEC :FEC (1:1:0.03v	0.01-3.0	100 200 2000	707 -- --	~16 -- --	-- 100 400	-- 83 73	-- ~100 ~100	[32 6]

)

2D MoS2/ polyaniline heterostructures	Wet chemistry synthesis	~1.0-1.2	75	AM: CB: CMC 80:10:10	1 M NaPF6 EC: DMC (1:1v)	0.01-3.0	20 300	888 --	~16 --	-- 100	-- ~89	-- ~100	[254]
ZnS-Sb_2S_3@C core-double shell polyhedron	High-temperature calcination and sulfurization reaction	--	65	AM: AB: LA-132 70:20:10	1 M NaClO4 PC+5%wFEC	0.01-1.8	100	1675	~39	120	~61	~100	[327]
P@Ni-P core@shell nanostructure	electroless deposition and chemical dealloying technique	2.0-2.5	93	AM: SP:CMC 70:15:15	1 M NaClO4 PC+5%wFEC	0.05-2.0	260 5000	1810 composite 550 composite	~12 --	200 2000	~70 ~74	~100 ~100	[328]
TiO2@SnS2@N-C	hydrothermal and atomic	~1	--			0.01-	200	1285	~35	--	--	--	[32]

heterostructure arrays	layer deposition					3.0	1000	--	--	600	~78	~100	9]
TiO_2-Coated Flower-like MoS_2 Nanosheets	atomic layer deposition	~3.0	100	AM:100	1 M NaClO4 EC:DMC (1:1 w) +5% v FEC	0.01-2.5	200 500	1393 --	~31 --	150 200	~76 ~69	~100 ~100	[33 0]
$Ni_2P/NiS_{0.66}$ Heterostructures	Hydrothermal and phosphidation/sulfidation	~1.0-2.0	~96.7	AM:SP:PVDF 80:10:10	1 M NaClO4 EC:DMC (1:1v) + 10% w FEC	0.01-3.0	100 200	519 520	~38 ~25	-- 150	-- ~45	-- ~100	[33 1]

Huang Zhang received his BS degree in 2010 in Polymer Materials from Jiangnan University and MS degree in 2013 in Materials Science from East China University of Science and Technology, China. Then, he had one-year of research experience as predoctoral fellow in University of Leuven, Belgium. Currently, he is pursuing his PhD in Physical Chemistry at Helmholtz Institute Ulm, Karlsruhe Institute of Technology in Germany under the supervision of Prof. Stefano Passerini. His research interests focus on the development of advanced materials for electrochemical energy storage.

Ivana Hasa is currently a Chemist Postdoc Fellow at Lawrence Berkeley National Laboratory (U.S.) within the Energy Storage and Distributed Resources Division in the group of Dr. Robert Kostecki. Her research activities are focused on the fundamental understanding of the solid/electrolyte interphase of alloying anodes for lithium-ion battery application. Prior to this, she carried out studies on sodium-ion battery materials development and characterization at Helmholtz Institute Ulm (Germany) and during her PhD studies at "Sapienza" University of Rome (Italy).

Stefano Passerini is Professor at the Karlsruhe Institute of Technology, Helmholtz Institute Ulm (Germany) since January 1, 2014. Formerly Professor at the University of Muenster (Germany), he co-founded the MEET battery research centre at the University of Muenster (Germany). His research activities are focused on electrochemical energy storage in batteries and supercapacitors.

Alloying and conversion anode materials enable the achievement of much higher specific capacity values for the next generation anode materials for sodium-ion batteries. Recent developments on nanostructured design of these concepts are reviewed to highlight the advantages and remaining challenges with respect to their governing chemistries and implementation of nanotechnology.

Keyword: Sodium-Ion Batteries

H. Zhang, I. Hasa*, S. Passerini*

Beyond Insertion for Na-ion Batteries: Nanostructured Alloying and Conversion Anode Materials